



HAL
open science

Macroscopic frictional contact scenarios and local contact dynamics: At the origins of “macroscopic stick-slip”, mode coupling instabilities and stable continuous sliding

Davide Tonazzi

► **To cite this version:**

Davide Tonazzi. Macroscopic frictional contact scenarios and local contact dynamics: At the origins of “macroscopic stick-slip”, mode coupling instabilities and stable continuous sliding. Materials and structures in mechanics [physics.class-ph]. INSA de Lyon; Università degli studi La Sapienza (Rome), 2014. English. NNT: 2014ISAL0110 . tel-01149051

HAL Id: tel-01149051

<https://theses.hal.science/tel-01149051>

Submitted on 6 May 2015

HAL is a multi-disciplinary open access archive for the deposit and dissemination of scientific research documents, whether they are published or not. The documents may come from teaching and research institutions in France or abroad, or from public or private research centers.

L'archive ouverte pluridisciplinaire **HAL**, est destinée au dépôt et à la diffusion de documents scientifiques de niveau recherche, publiés ou non, émanant des établissements d'enseignement et de recherche français ou étrangers, des laboratoires publics ou privés.



SAPIENZA
UNIVERSITÀ DI ROMA

INSA | INSTITUT NATIONAL
DES SCIENCES
APPLIQUÉES
LYON

N° order 2014ISAL0110

Year 2014

Ph.D. Thesis

Macroscopic frictional contact scenarios and local contact dynamics: at the origins of “macroscopic stick-slip”, mode coupling instabilities and stable continuous sliding

Jointly awarded at the
“La Sapienza” University of Rome
Dottorato di ricerca in Meccanica Teorica e Applicata XXVII ciclo

and at the
Institut National des Sciences Appliquées of Lyon
Ecole doctorale: Mécanique, Energétique, Génie Civil, Acoustique (MEGA)
Spécialité: Mécanique

by
Davide Tonazzi

On December 4th, 2014

PhD Committee:

Examiner/reviewer:	F. LEBON	Professor CNRS	(LMA, Aix-Marseille University)
Examiner/reviewer:	P. DUFRENOY	Professor	(LML, Lille1 University)
Examiner:	L. BAILLET	Professor	(ISTerre, UJF University of Grenoble)
Examiner/tutor:	Y. BERTHIER	Research Director CNRS	(LaMCoS, INSA-LYON)
Examiner/tutor:	F. MASSI	Associate Professor	(DIMA, “Sapienza” University of Rome)
Examiner/tutor:	A. FREGOLENT	Associate Professor	(DIMA, “Sapienza” University of Rome)
Examiner/tutor:	A. CULLA	Assistant Professor	(DIMA, “Sapienza” University of Rome)

Research laboratories:

Dipartimento Ingegneria Meccanica e Aerospaziale (DIMA)
Laboratoire de Mécanique des Contacts et des Structures (LaMCoS)

INSA Direction de la Recherche - Ecoles Doctorales - Quinquennal 2011-2015

SI GLE	ECOLE DOCTORALE	NOM ET COORDONNEES DU RESPONSABLE
CHIMIE	<p>CHIMIE DE LYON http://www.edchimie-lyon.fr Sec : Renée EL MELHEM Bat Blaise Pascal 3^e etage 04 72 43 80 46 Insa : R. GOURDON secretariat@edchimie-lyon.fr</p>	<p>M. Jean Marc LANCELIN Université de Lyon – Collège Doctoral Bât ESCPE 43 bd du 11 novembre 1918 69622 VILLEURBANNE Cedex Tél : 04.72.43 13 95 directeur@edchimie-lyon.fr</p>
E.E.A.	<p>ELECTRONIQUE, ELECTROTECHNIQUE, AUTOMATIQUE http://edeea.ec-lyon.fr</p> <p>Sec : HAVGOUDOUKIAN eea@ec-lyon.fr</p>	M.C.
E2M2	<p><u>EVOLUTION, ECOSYSTEME, MICROBIOLOGIE, MODELISATION</u> http://e2m2.universite-lyon.fr</p> <p>Sec : Safia AIT CHALAL Bat Atrium- UCB Lyon 1 04.72.44.83.62 Insa : S. REVERCHON Safia.ait-chalal@univ-lyon1.fr</p>	<p>Mme Gudrun BORNETTE CNRS UMR 5023 LEHNA Université Claude Bernard Lyon 1 Bât Forel 43 bd du 11 novembre 1918 69622 VILLEURBANNE Cédex Tél : 06.07.53.89.13 e2m2@univ-lyon1.fr</p>
E DISS	<p>INTERDISCIPLINAIRE SCIENCES-SANTE http://www.ediss-lyon.fr Sec : Safia AIT CHALAL Bat Atrium – UCB Lyon 1 04 72 44 83 62 Insa : Safia.ait-chalal@univ-lyon1.fr</p>	<p><u>Mme Emmanuelle CANET-SOULAS</u> INSERM U1060, CarMeN lab, Univ. Lyon 1 Bâtiment IMBL 11 avenue Jean Capelle INSA de Lyon 696621 Villeurbanne Tél : 04.72.68.49.09 Fax :04 72 68 49 16 Emmanuelle.canet@univ-lyon1.fr</p>
INFOMA THS	<p><u>INFORMATIQUE ET MATHEMATIQUES</u> http://infomaths.univ-lyon1.fr</p> <p>Sec :Renée EL MELHEM</p>	<p>Mme Sylvie CALABRETTO LIRIS – INSA de Lyon Bat Blaise Pascal 7 avenue Jean Capelle 69622 VILLEURBANNE Cedex</p>

	Bat Blaise Pascal 3 ^e étage infomaths@univ-lyon1.fr	Tél : 04.72. 43. 80. 46 Fax 04 72 43 16 87 Sylvie.calabretto@insa-lyon.fr
Matériaux	MATERIAUX DE LYON http://ed34.universite-lyon.fr Sec : M. LABOUNE PM : 71.70 –Fax : 87.12 Bat. Saint Exupéry Ed.materiaux@insa-lyon.fr	M. Jean-Yves BUFFIERE INSA de Lyon MATEIS Bâtiment Saint Exupéry 7 avenue Jean Capelle 69621 VILLEURBANNE Cedex Tél : 04.72.43 71.70 Fax 04 72 43 85 28 Ed.materiaux@insa-lyon.fr
MEGA	MECANIQUE, ENERGETIQUE, GENIE CIVIL, ACOUSTIQUE http://edmega.universite-lyon.fr/ Sec : M. LABOUNE PM : 71.70 –Fax : 87.12 Bat. Saint Exupéry mega@insa-lyon.fr	M. Philippe BOISSE INSA de Lyon Laboratoire LAMCOS Bâtiment Jacquard 25 bis avenue Jean Capelle 69621 VILLEURBANNE Cedex Tél : 04.72 .43.71.70 Fax : 04 72 43 72 37 Philippe.boisse@insa-lyon.fr
ScSo	ScSo* http://recherche.univ-lyon2.fr/scso/ Sec : Viviane POLSINELLI Brigitte DUBOIS Insa : J.Y. TOUSSAINT viviane.polsinelli@univ-lyon2.fr	Mme Isabelle VON BUELTZINGLOEWEN Université Lyon 2 86 rue Pasteur 69365 LYON Cedex 07 Tél : 04.78.77.23.86 Fax : 04.37.28.04.48 isavonb@gmail.com

ACCORD DE COOPERATION POUR LA MISE EN ŒUVRE D'UNE COTUTELLE DE THESE

L'Université de Rome "La Sapienza" ayant son siège à Rome (Italie), Piazzale Aldo Moro 5, représentée par son Recteur Professeur Luigi FRATI agissant en-qualité et en vertu des pouvoirs qui lui sont conférés d'une part

ET

L'INSA de LYON, représenté par le Professeur Daniel BARBIER, Directeur Adjoint de la Recherche, agissant en-qualités et en vertu des pouvoirs qui lui sont conférés, d'autre part

Pour la partie italienne :

- Vue la Loi n. 210 du 3 juillet 1998 art. 4 – doctorat de recherche ;
- Vu le D.M. 224/99 relatif aux normes en matière de doctorat de recherche ;
- Vu le D.M. 509/99 relatif aux normes en matière d'autonomie didactique des Universités ;
- Vu le Règlement de l'Université en matière de doctorat de recherche ;
- Vue la délibération du Sénat Académique du 2 octobre 2003 ;

ET

Vu pour la part française :

- L'arrêté du 6 janvier 2005 relatif à la procédure de cotutelle internationale de thèse (France);
- L'arrêté du 7 août 2006 relatif aux études doctorales (France);
- La convention cadre franco-italienne entre la Conférence des Présidents d'Université (CPU) et la Conferenza dei Rettori delle Università Italiane (CRUI) sur la reconnaissance des diplômes et validation des titres universitaires signée en date 18 janvier 1996;
- La convention cadre franco-italienne entre la Conférence des Présidents d'Université (CPU) e la Conferenza dei Rettori delle Università Italiane (CRUI) sur la co-tutelle de thèse signée le 13 février 1998;

désireux (désireuses) de contribuer à l'instauration et/ou au développement de la coopération scientifique entre équipes de recherche italiennes et étrangères en favorisant la mobilité des doctorants

sont convenu(e)s des dispositions suivantes

Titre I – Modalités administratives

Art. 1 – L'Université de Rome "La Sapienza" et L'INSA de Lyon désignées ci-après "les établissements", décident dans le respect des lois et des règlements en vigueur dans chacun des pays et/ou établissements, d'organiser conjointement une cotutelle de thèse au bénéfice de l'étudiant désigné ci-après :

Prénom et nom : Davide TONAZZI

spécialité : ingénieur Mécanique – Doctorat en Meccanica Teorica ed Applicata

sujet de thèse : **Analyse du couplage entre dynamique macroscopique des systèmes frottants et dynamique locale au contact.**

Le but de cette thèse est d'analyser l'évolution de la génération et de la propagation d'ondes dans les contacts frottants (freins, implants articulaires, liaisons quasi-statiques, glissement de terrains, tremblements de terre...) pour en contrôler le fonctionnement (frottement, usure) et maîtriser le comportement macroscopique (stick-slip, glissement continu, vibrations induites) à partir de la compréhension des phénomènes locaux.

L'étude des vibrations provoquées par le frottement est un problème scientifique ancien qui malgré des attentes industrielles importantes a très peu progressé du fait de son fort caractère interdisciplinaire (science des matériaux, tribologie, dynamique et contrôle des vibrations, mécanique de la rupture...). Par conséquent cette thèse fera dialoguer ces disciplines autour d'un problème modèle analysé à partir des derniers développements de la tribologie (science du mouvement) numérique.

Une synthèse des méthodologies et des analyses développées jusqu'ici dans les domaines de la tribologie, de la dynamique des structures et de la mécanique de la rupture (en sciences de l'ingénieur et sciences de la terre) a été réalisé dans le cadre d'une précédente thèse en cotutelle (M. Di Bartolomeo, 2008-2011) à l'aide des outils numériques actuels. La génération et la propagation d'ondes au contact ont été simulées et reliées à la fois à l'excitation locale au contact, qui est responsable de plusieurs phénomènes d'usure, et à l'excitation vibratoire de la structure, qui est responsable des instabilités dynamiques engendrées au contact (crissement, sprag-slip, stick-slip,...). Le travail proposé dans le cadre de cette thèse concerne la reproduction et investigation expérimentale des résultats numériques obtenus pendant la thèse de M. Di Bartolomeo par une analyse du phénomène sur un banc d'essais et l'investigation de l'influence de différents paramètres. Le point innovant par rapport aux travaux présents dans la littérature (Fineberg) est la volonté d'arriver à mesurer non seulement les valeurs globales (conséquence des phénomènes locaux) mais aussi à suivre la dynamique de la rupture et la propagation des ondes engendrées au niveau de l'interface des corps en contact glissant.

L'aspect innovant du projet de thèse est assuré par la validation et le passage à l'analyse du glissement et de l'interaction entre la dynamique locale (échelle du contact) et la dynamique globale (échelle des corps en contact) du système.

Les résultats attendus durant ce projet sont la compréhension des phénomènes et des facteurs responsables de la génération et de la propagation des ondes à la surface des contacts frottants. Cela permettra entre autre l'étude des mesures physiques à mettre en place pour prédire les événements sismiques; la prévention des instabilités dynamiques (ou la diminution du bruit, des vibrations) dans les applications existantes; le développement de méthodes de contrôle du coefficient de frottement global à partir d'« envoi d'ondes » dans les surfaces en contact, qui modifieraient le frottement local et donc le comportement macroscopique du système (stick-slip, glissement continu, vibrations induites, etc.).

Les principes et les modalités administratives et pédagogiques de cette cotutelle sont définis par le présent accord.

Art. 2 - La durée prévue pour la préparation de la thèse en cotutelle est de 3 ans, à partir de l'année scolaire 2011/2012.

En cas de nécessité, cette durée peut être prolongée en conformité avec la réglementation en vigueur dans les deux établissements.

Art. 3 - La préparation de la thèse s'effectue par périodes alternées, à peu près équivalentes, dans chacun des deux établissements partenaires. La durée de ces périodes sera déterminée de commun accord par les deux directeurs de thèse.

Art. 4 – L'étudiant Davide TONAZZI

est tenu à s'inscrire régulièrement dans les deux établissements. L'étudiant paiera les droits d'inscriptions à l'Université La Sapienza de Rome et en sera dispensé près l'INSA de Lyon.

Art. 5 – Pour les périodes d'études effectuées en France et pour la soutenance, le doctorant bénéficie de l'ensemble des dispositions de l'arrêté du 7 août 2006 susvisé, et de la charte des thèses de l'INSA de Lyon.

Art.6 – Lors de son inscription, le doctorant devra fournir les justificatifs relatifs à ses ressources, à sa couverture sociale ainsi qu'à son assurance relative aux accidents du travail, dans chacun des pays.

Titre II – Modalités pédagogiques

Art. 1 – Le travail de thèse de l'étudiante sera réalisé sous la supervision commune de deux directeurs de thèse :

- Annalisa FREGOLENT (Professeur du Département de Meccanica e Aeronautica), directeur de thèse à l'Université "La Sapienza" ;
- Yves BERTHIER (Professeur au Laboratoire de Mécanique des Contacts et des Structures), directeur de thèse à l' INSA de Lyon ;

qui s'engagent à exercer pleinement la fonction de tuteurs de la candidate ainsi qu'à formuler chacun un avis écrit sur la thèse de Doctorat.

L'avis favorable des deux Directeurs de Thèse est une condition nécessaire à l'admission à l'examen final.

Art. 2- La thèse donnera lieu à une soutenance unique, reconnue par les deux établissements concernés. La soutenance aura lieu à l'université de Rome "La Sapienza". Le jury de soutenance est composé sur la base d'une proportion équilibrée de membres de chaque établissement désignés conjointement par les établissements contractants et comprend, en outre, des personnalités extérieures à ces établissements.

Il comprendra au moins quatre membres et au maximum huit membres, dont, sauf dérogation, les deux directeurs de thèse.

Art. 3- La thèse sera rédigée et discutée en Anglais. Elle comportera un résumé substantiel rédigé en français.

Art. 4 – En cas de rapport favorable du Jury, chacun des deux établissements s'engage à conférer le titre de docteur de recherche pour la même thèse.

L'Université de Rome "La Sapienza" s'engage à conférer le grade de docteur de recherche en Meccanica Teorica e Applicata.

L'INSA de Lyon s'engage à conférer le grade de docteur de recherche en Mécanique.

Art. 5- Lorsque le doctorant doit valider des formations complémentaires (scientifiques ou visant à son insertion professionnelle), les établissements (l'Ecole Doctorale MEGA pour l'INSA) préciseront les modalités de reconnaissance mutuelle de ces formations, en accord avec les directeurs de thèse et le doctorant.

Titre III – Conclusions

Art. 1 – L'étudiant est tenu de respecter les règlements et les usages de l'établissement d'accueil.

Art. 2 – Par l'intermédiaire de leurs directeurs de thèses respectifs, les établissements signataires s'engagent à se communiquer toutes les informations et la documentation utiles à l'organisation de la cotutelle de thèse faisant l'objet du présent accord.

Art. 3 – Les modalités de présentation, de dépôt et de reproduction de la thèse seront établies dans chaque pays dans le respect de la réglementation en vigueur.

La protection du sujet de thèse, ainsi que la publication, l'exploitation et la protection des résultats issus des travaux de recherche du doctorant dans les deux établissements signataires seront assujetties à la réglementation en vigueur et assurées conformément aux procédures spécifiques à chacun des pays impliqués dans la cotutelle.

Sur demande, les dispositions concernant la protection des droits de propriété intellectuelle pourront faire l'objet de protocoles ou de documents spécifiques.

Art. 4 – Le présent accord entre en vigueur à partir de la date de signature du représentant légal de chaque établissement signataire et le reste jusqu'à la fin de l'année universitaire au cours de laquelle la thèse ou les travaux seront soutenus. Dans le cas où l'étudiant ne serait pas inscrit dans l'un et/ou l'autre des établissements signataires, ou bien renoncerait par écrit à poursuivre, ou bien n'est pas autorisé à poursuivre la préparation de sa thèse en vertu de la décision de l'un au moins des deux directeurs de thèse, les deux établissements signataires mettront fin conjointement et sans délai, aux dispositions du présent accord.

Art. 5 – Le présent accord est rédigé en quatre exemplaires originaux, dont deux en italien et deux en française, faisant également foi.

Roma, li 19 DIC. 2011



Pour le Recteur de l'Université
La Sapienza de Rome

Il Coordinatore del Dottorato di Ricerca
Carlo Massimo CASCIOLA

Co-direttori di tesi
Annalisa FREGOLENT

Antonio CULLA

Le Doctorant
Davide TONAZZI

Villeurbanne, li 09 JAN. 2012

Pour le directeur de l'INSA de Lyon
Professeur Daniel BARBIER
Directeur Adjoint de la Recherche



Le Responsable de l'Ecole Doctorale
Philippe BOISSE

Le Directeur du laboratoire
David DUREISSEIX

Co-directeur (s) de thèse
Yves BERTHIER

Francesco MASSI

CONVENZIONE PER UNA CO-TUTELA DI TESI DI DOTTORATO DI RICERCA

L'Università degli Studi di Roma "La Sapienza" con sede in Roma (Italia), Piazzale Aldo Moro, 5 rappresentata dal Rettore Prof. Luigi FRATI, che opera in virtù dei poteri che gli sono conferiti, da una parte

e

L'INSA di Lione rappresentata dal Professore Daniel BARBIER, Addetto alla Direzione della Ricerca, che opera in virtù dei poteri che gli sono conferiti, dall'altra parte

Per la parte italiana:

- VISTA la Legge 210 del 3 luglio 1998 art. 4 – dottorato di ricerca;
- VISTO il D.M. 224/99 recante norme in materia di dottorato di ricerca
- VISTO il D.M. 509/99 recante norme concernenti l'autonomia didattica degli Atenei;
- VISTO il Regolamento di Ateneo in materia di dottorato di ricerca;
- VISTA la delibera del Senato Accademico del 2 ottobre 2003;

e

Visti, per la parte francese,

- La delibera del 6 gennaio 2005 relativo alla procedura internazionale per la cotutela di tesi (Francia);
- La delibera del 7 agosto 2006 relativo al dottorato (Francia);
- La convenzione franco-italiana tra la Conférence des Présidents d'Université (CPU) e la Conferenza dei Rettori delle Università Italiane (CRUI) sul riconoscimento dei diplomi e della validità dei titoli universitari siglata in data 18 gennaio 1996;
- La convenzione franco-italiana tra la Conférence des Présidents d'Université (CPU) e la Conferenza dei Rettori delle Università Italiane (CRUI) sulla cotutela di tesi siglata li 13 febbraio 1998;

nell'intento di contribuire ad instaurare e/o sviluppare la cooperazione scientifica tra équipes di ricerca italiana e straniera attraverso la mobilità dei dottorandi

convengono e stipulano quanto segue

Parte prima – Modalità amministrative

Art. 1 – L'Università degli Studi di Roma "La Sapienza" e L'INSA di Lione denominati qui di seguito "Istituzioni" concordano, nel rispetto delle leggi e dei regolamenti in vigore in ciascun Paese e/o Istituzione, di organizzare congiuntamente una co-tutela di tesi di dottorato a beneficio del dottorando sottoindicato:

nome e cognome: Davide TONAZZI

iscritto al corso di Dottorato di Ricerca in Meccanica Teorica e Applicata presso l'Università La Sapienza di Roma e in "Mecanique" presso l'"ecole doctoral MEGA".

Soggetto di tesi: **Analisi dell'interazione tra dinamica globale e dinamica locale dei sistemi in contatto strisciante.**

Lo scopo di questa tesi è quello di analizzare la generazione e propagazione delle onde nei contatti striscianti (freni, protesi articolari, giunti quasi-statici, geofisica, terremoti ...) per

controllare il funzionamento (attrito, usura) e il comportamento macroscopico (stick-slip, scorrimento continuo, vibrazioni indotte) a partire dalla comprensione dei fenomeni locali.

Lo studio delle vibrazioni provocate da attrito è un problema scientifico non recente e che, nonostante le importanti applicazioni industriali, è tuttora parzialmente incompreso a causa della sua natura fortemente interdisciplinare (scienza dei materiali, tribologia, dinamica e controllo delle vibrazioni, meccanica della frattura ..). Questa tesi cercherà di sintetizzare gli strumenti di differenti discipline intorno ad un problema modello analizzato utilizzando gli ultimi sviluppi della tribologia numerica.

Una sintesi delle metodologie e delle analisi sviluppate fino ad oggi nel campo della tribologia, della dinamica delle strutture e della meccanica della frattura (in ingegneria e scienze della terra) è stata eseguita in una precedente tesi di dottorato in co-tutela (M. Di Bartolomeo, 2008-2011) utilizzando gli attuali strumenti numerici.

E' stata svolta un'analisi numerica per simulare la generazione e la propagazione di onde dovute al contatto. Tale fenomeno è legato sia alla dinamica locale al contatto, che è responsabile di diversi fenomeni di usura, sia all'eccitazione vibrazionale della struttura, che è responsabile dell'instabilità dinamica causata dal contatto (squeal, sprag-slip, stick-slip).

Il lavoro proposto in questa tesi riguarda la riproduzione e l'analisi sperimentale dei risultati numerici ottenuti durante la tesi del Dr. Di Bartolomeo, tramite la riproduzione del fenomeno su un set-up sperimentale, per indagare l'influenza dei vari parametri.

Il punto innovativo in relazione ai lavori presenti in letteratura (Fineberg) è l'obiettivo di arrivare a misurare non solo i valori globali (conseguenza dei fenomeni locali), ma anche di monitorare la dinamica della rottura e la propagazione delle onde generate all'interfaccia in contatto strisciante.

L'obiettivo del progetto di tesi è rappresentato dalla riproduzione e dall'analisi dello scorrimento e la comprensione dell'interazione tra la dinamica locale e la dinamica globale del sistema. I risultati attesi da questo progetto sono la comprensione dei fenomeni e dei fattori responsabili della generazione e propagazione delle onde sulla superficie di contatto.

Questo si focalizza sulle misure fisiche messe in atto per prevedere fenomeni di instabilità dinamica (o ridurre il rumore, vibrazioni, terremoti) nelle applicazioni esistenti e nello sviluppo di metodi di controllo del coefficiente di attrito tramite opportuni campi acustici artificiali inviati sulle superfici di contatto, per "guidare" la dinamica locale al contatto e quindi modificare il comportamento macroscopico del sistema (stick-slip, scorrimento continuo, vibrazioni indotte dall'attrito, ecc.).

I principi e le modalità amministrative e didattiche di tale co-tutela sono definiti dalla presente convenzione.

Art.2 - La durata per la preparazione della tesi è di 3 anni, a partire dall'anno accademico 2011/2012.

In caso di necessità tale durata potrà essere prorogata in conformità con la regolamentazione vigente nelle due Istituzioni.

Art.3 - La preparazione della tesi si effettuerà in periodi alterni, pressoché equivalenti, in ciascuna delle due Istituzioni. La durata di tali periodi sarà fissata in comune accordo dai due Direttori di tesi.

Art.4 - Il dott. Davide TONAZZI sarà iscritto in entrambe le Istituzioni. Corrisponderà i regolari diritti di iscrizione all'Università "La Sapienza" di Roma e ne sarà esonerato presso INSA di Lione.

Art.5 - Per tutto il periodo di preparazione della tesi il dott. Davide TONAZZI beneficerà di quanto disposto dalla delibera del 7 Agosto 2006 e della carta dei tesisti de l'INSA de Lyon.

Art.6 - Per la durata della sua iscrizione, il dott. Davide TONAZZI dovrà fornire giustificazione relativamente alle sue risorse, alla sua coperta sanitaria così come alla sua assicurazione sugli incidenti di lavoro, in ognuno dei paesi.

Parte seconda – Modalità didattiche

Art.1 – Il dott. preparerà la tesi sotto la direzione comune dei professori:

- Annalisa FREGOLENT (Docente presso il dipartimento di Meccanica e Aeronautica), direttore di tesi a l'Università di Roma "La Sapienza"
- Yves BERTHIER (Docente presso il Laboratorio di Meccanica dei Contatti e delle strutture), direttore di tesi all'INSA di Lione

che si impegnano ad esercitare pienamente la funzione di tutori del dottorando e si impegnano a valutarne, ciascuno con propria relazione scritta, la tesi di Dottorato.

Il giudizio positivo di entrambi i Direttori di Tesi è condizione necessaria per l'ammissione all'esame finale.

Art. 2 - La discussione della tesi, unica e riconosciuta dalle due istituzioni, avrà luogo presso l'Università di Roma "La Sapienza". La Commissione giudicatrice, nominata dai Rettori delle due Università, sarà composta da un numero pari di studiosi appartenenti alle due Istituzioni e designati congiuntamente da esse, oltre a membri esterni alle due Istituzioni. Essa dovrà essere composta da un minimo di quattro membri ed un massimo di otto, appartenenti ai settori scientifico-disciplinari del Dottorato, tra cui, a meno di derogazioni, i due direttori di tesi.

Art. 3 – La tesi sarà redatta e discussa in inglese; un riassunto sostanziale sarà redatto in lingua francese.

Art. 4 – Ognuna delle due Istituzioni si impegna a conferire il titolo di dottore di ricerca per la stessa tesi, in seguito ad una relazione favorevole della Commissione giudicatrice.

L'Università degli Studi di Roma "La Sapienza" conferirà il titolo di dottore di ricerca in Meccanica Teorica e Applicata.

L'INSA di Lione conferirà il titolo di dottore di ricerca in Meccanica.

Art. 5- In caso il dottorando dovesse convalidare le formazioni complementari (scientifiche o mirate alla sua inserzione professionale), le Istituzioni (l'Ecole Doctorale MEGA pour l'INSA) specificheranno le modalità di riconoscimento reciproco di queste formazioni, in accordo con i direttori di tesi ed il dottorando.

Parte terza – Conclusione

Art. 1 – Il dottorando dovrà rispettare i regolamenti e le consuetudini dell'Istituzione ospitante.

Art. 2 – Le Istituzioni contraenti, attraverso l'intermediazione dei rispettivi direttori di tesi, si impegnano a comunicarsi rispettivamente tutte le informazioni e la documentazione utile per l'organizzazione della co-tutela di tesi oggetto della presente convenzione.

Art. 3 – Le modalità di presentazione, di deposito e riproduzione della tesi saranno effettuati in ogni paese secondo i regolamenti in vigore.

La protezione dell'oggetto della tesi, così come la pubblicazione, lo sfruttamento e la protezione dei risultati ottenuti con lo studio di ricerca del dottorando nelle Istituzioni contraenti saranno assoggettati alla normativa in vigore e assicurati conformemente alle procedure specifiche di ciascun Paese coinvolto nella co-tutela.

Qualora richiesto, le disposizioni relative alla protezione dei diritti di proprietà intellettuale potranno costituire oggetto di protocolli o documenti specifici.

Art. 4 – La presente convenzione entra in vigore dalla data di firma del rappresentante legale di ciascuna Istituzione contraente e sarà valida fino alla fine dell'anno accademico nel corso del quale la tesi o lo studio saranno discussi.

Nel caso in cui il dottorando non fosse iscritto in una e/o l'altra delle Istituzioni contraenti, oppure rinunciasse per iscritto a proseguire, oppure, in virtù della decisione di almeno uno dei due direttori di tesi, non fosse autorizzato a proseguire la preparazione della tesi in co-tutela, le Istituzioni contraenti porranno fine, congiuntamente e senza ritardo, alle disposizioni del presente accordo.

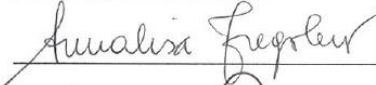
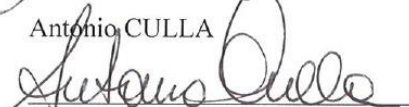
Art. 5 – La presente convenzione è redatta in quattro esemplari originali, di cui due in lingua italiana e due in lingua francese, aventi valore legale.

Roma, li 19 DIC. 2011
Per il Rettore dell'Università
di Roma "La Sapienza"

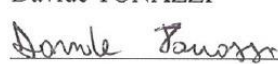



Il Responsabile del Dottorato di Ricerca
Carlo Massimo CASCIOLA

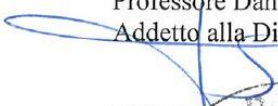
Co-direttori di tesi
Annalisa FREGOLENT


Antonio CULLA


Il Dottorando
Davide TONAZZI

Villeurbanne, li 09 JAN. 2012
Per il Direttore dell'INSA de Lyon
Professore Daniel BARBIER
Addetto alla Direzione della Ricerca


Il Responsabile del Dottorato di Ricerca
Philippe BOISSE

Il Direttore del Laboratorio
David DUREISSEIX

Co-direttori di tesi
Yves BERTHIER


Francesco MASSI




To my family

Acknowledgements

This thesis arises in the framework of a “cotutelle” thesis between La Sapienza of Rome and the INSA of Lyon. Firstly, I would like to thank the institutions that have supported this research and made it possible: the doctoral school of Theoretical and Applied Mechanics of the University of Rome "La Sapienza" and the doctoral school MEGA (Mécanique, Energetique, Génie Civil, Acoustique) of the INSA of Lyon. Then I would like to continue by thanking my Italian and French supervisors and co-supervisors of thesis: the Professors Annalisa Fregolent, Antonio Culla, Francesco Massi, Yves Berthier for their professional guidance during the development of this research work. Of course, a special thanks to Francesco Massi for his encouragement and for the constant support during these years. I would like also to express my gratitude to the Professor Laurent Baillet for his collaboration and contribution to the research work. Sincere thanks goes also to the reviewers, Professor Frédéric Lebon and Professor Philippe Dufrenoy for their comments and suggestions that allowed for improving this work. I would like to finish extending my greeting to all friends, colleagues, professors, people that I have had the opportunity and the pleasure to meet during these years, at the LaMCoS as well as at the DIMA or somewhere else. Among them, Fangfang, Matthieu, Alexandra, Guillaume, Mathieu, Hung, Rudy, Livia, Ghassene, Serge, Komla, Jerome, Joe, Sayed, Samuel, Edouard, Aurélien, Guilhem, Pierre, Arnaud, Marion, Gianluca, David, Paolo, Silvia, Ahmed, Rafael, Silvio. I big special thanks to my “French-Italian” friends Jacopo, Manuel, Giovanna and Francesca and to my Italian friends Samantha, Giovanni, Christian and Giuseppe.

Concluding, a last but certainly not least thanks to my family Manlio, Pia, Pamela to whom this thesis is dedicated.

Macroscopic frictional contact scenarios and local contact dynamics: at the origins of “macroscopic stick-slip”, mode coupling instabilities and stable continuous sliding

Résumé étendu

Le comportement local d'un contact et son interaction avec la dynamique globale du système qui le contient, sont à l'origine d'innombrables problèmes de contact concernant plusieurs disciplines telles que la tribologie, la géophysique, la mécanique vibratoire ou la mécanique de la rupture. Une première importante contribution à la compréhension du frottement sec a été réalisée par Léonard de Vinci (1495); il a été le premier ingénieur à introduire le terme de coefficient de frottement. Quelques siècles plus tard, Amontons [1] et Coulomb [2] ont amélioré le concept de friction entre les corps solides par rapport aux différents matériaux, la composition de la surface, la lubrification, l'humidité et les effets de la température. Dans l'histoire, les phénomènes de frottement ont été fondamentalement examinés plutôt en comparaison aux aspects mécaniques du contact.

Dans les dernières décennies, le développement de méthodes de simulations expérimentales et numériques pour l'étude des phénomènes de frottement, ont produit une croissance soudaine du nombre d'activités de recherche en tenant compte non seulement des aspects du contact, mais aussi de la réponse du système auquel les surfaces de contact appartiennent. Godet [3] et Berthier [4] ont introduit le concept de «troisième corps» dans l'étude des phénomènes de frottement menant à la notation du "Triplet Tribologique". Cette approche met en évidence la façon dont le contact entre deux surfaces frottantes est influencé par le troisième corps, qui peut être un liquide, un gaz ou un film solide interposé entre les interfaces de contact et par le mécanisme (dynamique du système); par conséquent l'analyse des problèmes de contact implique l'interaction de divers phénomènes à différentes échelles.

En outre, la compréhension des mécanismes physiques, impliquant le couplage entre le contact (échelle locale) et la dynamique des systèmes (échelle de la structure) pendant le mouvement relatif, est d'une grande importance pour de nombreuses recherches et applications industrielles. Ces mécanismes, liés à des échelles soit du contact soit de la structure, peuvent compromettre le bon fonctionnement des systèmes ayant des interfaces en contact. Beaucoup de publications récentes portent sur des questions spécifiques des systèmes complexes, comme le crissement des freins [5-9], l'instabilité des disques d'embrayage [10], le fretting [11], les failles sismiques [12], la perception tactile [13], ou le cris-

sement de la prothèse de hanche [14, 15]. Leurs objectifs étant de contrôler ou de prévoir les effets des vibrations dues au frottement pour chaque cas particulier. De nombreux articles dans différents domaines ont été consacrés à l'étude des instabilités des systèmes excités par les forces de contact liées au frottement. Par exemple, à la suite des approches centrées sur l'échelle de contact (les ondes d'interface et des fronts de rupture [16-18], les précurseurs [19, 20], de l'usure et du troisième corps [21]) ou axées sur la réponse globale du système (les modes instables [22], les vibrations induites par le frottement [23], le « stick-slip macroscopique » [24-26]). Cependant, une approche générale permettant de reproduire et d'étudier les différents types de comportements de frottement en fonction des paramètres du système, n'a pas encore été élaborée.

Dans ce contexte, cette thèse est dédiée à l'étude des différents mécanismes à l'origine de différents scénarios de contact dus au frottement lorsque deux corps élastiques sont en contact frottant, en fonction des paramètres clés du système (conditions aux limites, frottement, matériaux en contact, amortissement, etc). Ce travail veut fournir des indications sur la façon dont le couplage entre le comportement local (contact) et la dynamique globale (système) est à l'origine des différents scénarios de contact qui se posent dans les systèmes de frottement. Alors que les simulations numériques ont été développées pour l'étude des phénomènes physiques locaux (l'état du contact, la rupture et les propagations d'onde, etc), impossibles à mesurer expérimentalement de façon appropriée, et le couplage avec la réponse dynamique du système, les résultats expérimentaux ont permis de valider les résultats numériques. Les simulations expérimentales et numériques ont permis de dessiner des cartes des scénarii de contact, en fonction des paramètres considérés.

Le travail présenté dans ce manuscrit vise à étudier les phénomènes physiques et à développer les outils numériques et expérimentaux nécessaires à l'étude. Pour cette raison, après une première vue d'ensemble des outils numériques et expérimentaux utilisés, une analyse numérique et une version expérimentale préliminaire sont décrites pour obtenir les principaux aperçus des phénomènes. Puis, une fois le dispositif expérimental et le modèle numérique mis à jour pour permettre une analyse plus fine, une comparaison quantitative entre les expériences et les simulations numériques est présentée. Le travail est organisé en quatre parties principales.

La première partie de la thèse présente un aperçu des principaux problèmes de dynamique de contact dus au frottement (chapitre 1), les outils numériques (chapitre 2) et expérimentaux (chapitre 3) utilisés pour réaliser les investigations de deux milieux élastiques simples en mouvement relatif. Après une introduction générale sur les vibrations induites par frottement, l'attention est concentrée sur les instabilités qui peuvent survenir entre deux corps en contact frottant.

Même s'il est ambitieux de fournir une classification complète des vibrations liées au frottement, une significative (pour le présent travail) classification peut être formulée, en fonction de la réponse dynamique globale du système, comme suit :

- l'instabilité du « macroscopique stick-slip » [27-29] induite par le contact frottant dans les systèmes élastiques. D'un point de vue macroscopique, le scénario macroscopique du stick-slip est caractérisé par la chute soudaine de la force de frottement (état de glissement), séparée par des périodes d'accumulation d'énergie élastique (état d'adhérence). De fortes vibrations du système sont induites par des excitations impulsives en raison des chutes de la force tangentielle (glissement macroscopique), due aux fronts de rupture à l'interface de contact,
- l'instabilité dynamique du système. La réponse de la structure est caractérisée par des vibrations instables harmoniques du système, à une de ses fréquences propres, excitées par les forces de frottement,
- vibrations stables du système en raison de la réponse dynamique du système à l'excitation aléatoire provenant de la rugosité à l'interface. Même si le système est dynamiquement stable, des oscillations de faible amplitude avec un spectre de fréquence large, caractérisent la réponse du système au cours de glissement macroscopique. Ces types d'instabilités, générées par des forces de frottement, ont principalement été l'objet de publications traitant de problèmes spécifiques dans différents domaines tels que le crissement des freins, le crissement des prothèses de hanche, les vibrations roue-rail, les tremblements de terre, etc.

Dans ce contexte, des analyses expérimentales et numériques ont été ici mis en place pour comprendre comment le comportement de l'interface locale affecte la réponse macroscopique du système et vice-versa, au cours des scénarios d'instabilité. Le chapitre 2 présente les outils numériques utilisés pour réaliser l'étude des scénarii de frottement pour des systèmes de contact en glissement. La première partie du chapitre traite de la description de la géométrie du modèle et des conditions aux limites utilisées pour l'analyse transitoire non-linéaire (Figure I).

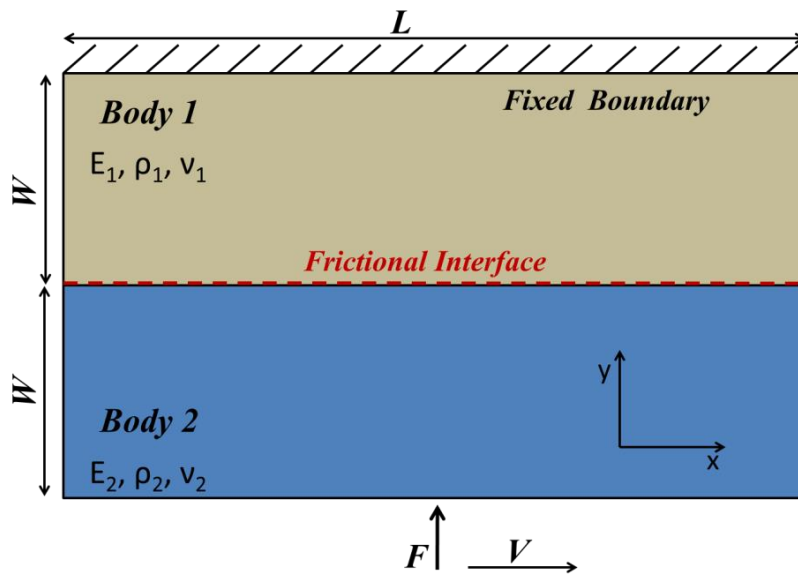


Figure I: Géométrie de base et conditions aux limites utilisées pour le modèle numérique. F est la force de compression appliquée à la limite inférieure du corps 2, et V est la vitesse horizontale imposée à la même limite du corps 2 ; à chaque nœud de l'interface est imposée la loi de contact.

Le modèle considéré a permis d'étudier l'interaction entre la dynamique globale et le comportement local du contact entre corps déformables en mouvement relatif. Le code aux éléments finis PLASTD utilisé est spécifique à la solution des problèmes de contact transitoire dynamiques. Une description de la modélisation du contact pour simuler le comportement du contact local et les lois de frottement adoptées est présentée. La deuxième partie du chapitre décrit l'analyse en fréquence linéaire et la formulation liée au problème aux valeurs propres complexes pour les systèmes de frottement ; un intérêt particulier est adressé à la stabilité dynamique du système.

Le chapitre 3 présente les outils expérimentaux utilisés pour étudier les scénarii de frottement qui se produisent pendant le mouvement relatif entre deux corps déformables. Une description du dispositif expérimental (PEDEBA), l'approche, les matériaux et la méthode utilisée pour effectuer une analyse préliminaire du contact sont d'abord présentés. Ensuite, la deuxième partie du chapitre traite d'une description détaillée du nouveau banc d'essai (TRIBOWAVE) récemment développé au laboratoire LaMCoS (Figure II). Les éléments fondamentaux et l'instrumentation, nécessaires pour étudier le comportement du frottement et la dynamique du système pour chaque essai sont décrits en détail. La rigidité et la dynamique tangentielle du dispositif expérimental sont utilisées afin de mieux caractériser la réponse dynamique de l'ensemble (banc d'essai et matériaux en contact). La caractérisation dynamique du banc d'essai a permis de

mettre à jour le modèle numérique et d'effectuer une comparaison quantitative entre les résultats expérimentaux et numériques (chapitre 6).

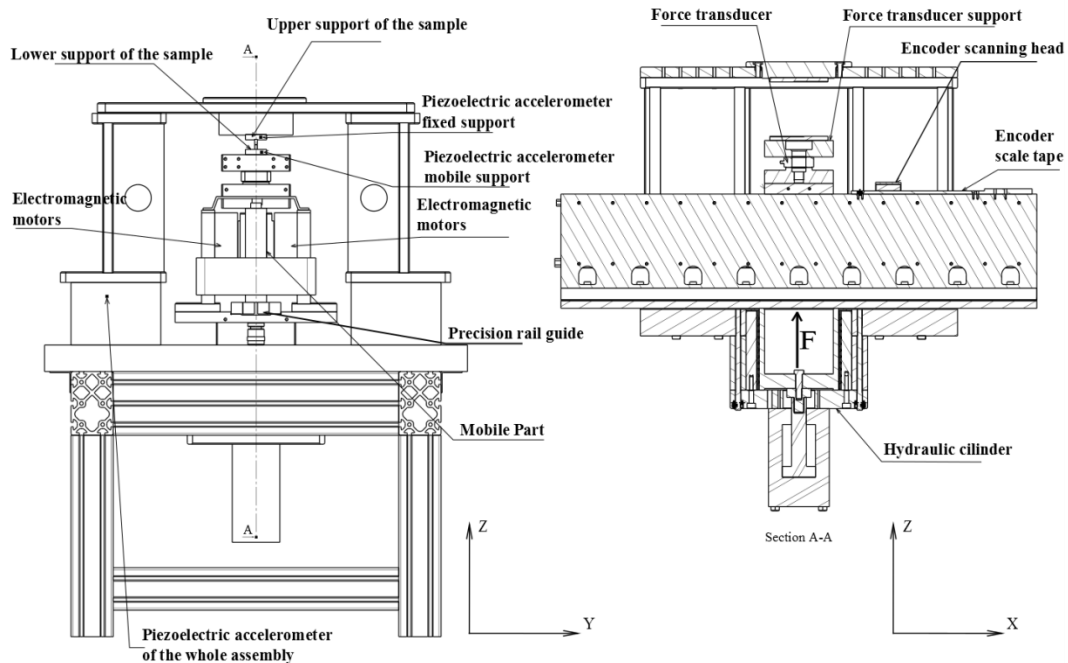


Figure II: *Vue latérale et frontale du nouveau banc d'essai (TRIBOWAVE).*

La deuxième partie (chapitre 4) présente une première analyse numérique sur l'effet de l'amortissement des matériaux sur la réponse du frottement de deux corps élastiques en mouvement relatif séparés par une interface de frottement. L'approche adoptée dans la mécanique du contact est couplée avec l'analyse dynamique du système mécanique. Les simulations transitoires non linéaires, effectuées et l'analyse aux valeurs propres complexes, ont conduit à reproduire et à étudier les différents scénarii qui se produisent lorsque les forces de frottement excitent le système. L'analyse numérique a mis en évidence que le même système mécanique peut passer d'instabilité de type « macroscopique stick-slip » au glissement continu, avec ou sans instabilité dynamique, en fonction des paramètres d'amortissement. Le mécanisme de sélection entre ces scénarii est une combinaison de la dynamique locale de contact et son couplage avec la réponse dynamique macroscopique du système mécanique, décrit dans le chapitre 4.

Les simulations transitoires non linéaires et l'analyse aux valeurs propres complexes soulignent que les paramètres d'amortissement α et β ($C = \alpha M + \beta K$) affectent la réponse du système d'une manière différente.

Le coefficient d'amortissement α , relatif à la matrice de masse :

- i) joue un rôle important sur l'amortissement de la réponse du système (vibrations du système excité) lorsque le comportement du système est dominé par des phénomènes de type « macroscopique stick-slip » ;
- ii) affecte la stabilité des modes à basse fréquence et l'amplitude du cycle limite lors du glissement continu avec l'instabilité dynamique.

Le coefficient d'amortissement β , relatif à la matrice de rigidité :

- i) affecte en amortissant les dynamiques locales (de propagation des ondes et de la rupture) au contact, le comportement de frottement macroscopique du système qui se déplace du stick-slip au glissement continu,
- ii) affecte l'amortissement et l'instabilité dynamique des modes aux fréquences plus élevées.

Une carte numérique des scénarios de frottement a été établie (Figure III). Les différents scénarios ont été analysés en attirant l'attention à la fois sur l'interface du contact (l'état de l'interface, la propagation d'ondes et les ruptures) et à la réponse dynamique du système (vibrations mécaniques dues au couplage modale, « macroscopique stick-slip »).

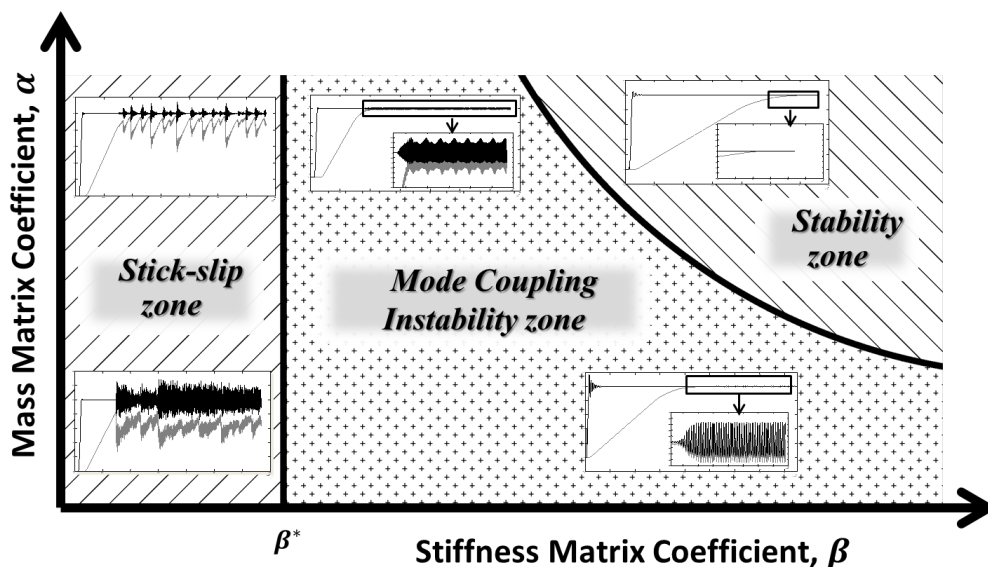


Figure III: Carte des scénarii d'instabilité en fonction des paramètres d'amortissement.

Dans la troisième partie (chapitre 5) une analyse expérimentale préliminaire a été effectuée dans le but de faire une première comparaison qualitative entre les résultats expérimentaux et numériques de la réponse globale du système. Le chapitre 5 présente des observations expérimentales des comportements macroscopiques dus aux frottements, reproduits avec l'ancien banc d'essai (PEDEBA).

La réponse macroscopique de deux milieux élastiques en mouvement relatif a été étudiée expérimentalement, en soulignant comment le comportement de contact frottant est affecté par les conditions aux limites imposées. « Macroscopique stick-slip », instabilité dynamique et transition vers un glissement stable continu ont été observés.

La première partie de ce chapitre montre les résultats obtenus par l'analyse expérimentale du comportement de deux blocs de polycarbonate en contact frottant. En fonction des conditions aux limites (charge et vitesse tangentielles imposées), le même système frottant présente un comportement différent, en passant de phénomènes de type « macroscopique stick-slip », à de l'instabilité modale jusqu'à du glissement stable continu. Différentes réponses structurelles (l'amplitude des vibrations, les fréquences et les accélérations excitées) du système ont été observées en fonction de la réponse due au frottement.

La seconde partie du chapitre présente une comparaison (qualitative) préliminaire entre l'analyse numérique et expérimentale en fonction des mêmes paramètres. Dans la modélisation par éléments finis, une loi de contact qui prend en compte le coefficient de frottement en fonction du temps d'adhérence (sticking), est représentée, dans le but de simuler le comportement de frottement de polycarbonate. Le code explicite aux éléments finis, PLASTD, a été utilisé pour effectuer l'analyse transitoire numérique.

L'analyse fréquentielle et temporelle des essais expérimentaux présente un bon accord qualitatif avec les résultats numériques obtenus par les simulations transitoires de contact. La transition de « macroscopique stick-slip » à glissement continu avec ou sans vibrations instables du système, a été mise en évidence expérimentalement et numériquement en fonction des conditions aux limites (force normale de contact et vitesse imposées). Des cartes des scénarii d'instabilité (Figure IV) ont été établies en fonction des conditions aux limites tant expérimentalement que numériquement. En ce qui concerne le chapitre précédent, où le paramètre étudié était le matériau d'amortissement, l'analyse numérique est ici développée en fonction des paramètres qui peuvent varier expérimentalement (force normale de contact et vitesse).

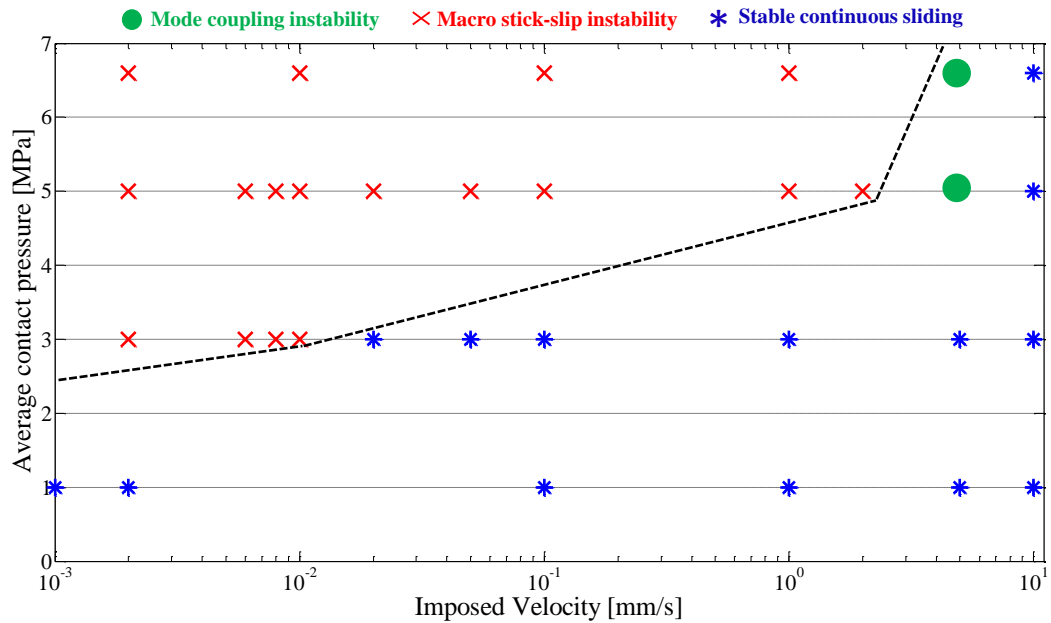


Figure IV : Carte expérimentale des scénarii de contact en fonction de la vitesse imposée et de la pression de contact moyenne.

Dans la dernière partie de la thèse (chapitre 6) une analyse expérimentale plus fine a été réalisée pour étudier le couplage entre la dynamique du système et la dynamique de contact et fournir une comparaison quantitative avec les simulations numériques. Le banc d'essai le plus récent (TRIBOWAVE), décrit dans le chapitre 2, a alors été développé. Ce banc d'essai a permis de reproduire et d'analyser les différents comportements de frottement macroscopiques et leur apparition en fonction d'une gamme plus large et plus contrôlée de conditions aux limites. La rigidité et la dynamique tangentielle du nouveau banc d'essai ont été mesurées et ainsi incluses dans le modèle numérique. En fait, car le passage entre les différents scénarii de frottement macroscopique est fonction du couplage entre la dynamique de contact et la dynamique du système, le banc d'essai expérimental doit fournir l'accès à la fois à l'échelle locale (contact) et au comportement globale du système.

Le développement du banc d'essai TRIBOWAVE et la mise à jour du modèle numérique, comprenant la rigidité et la dynamique du banc d'essai, ont permis de développer une comparaison quantitative entre les résultats expérimentaux et numériques (Figure V).

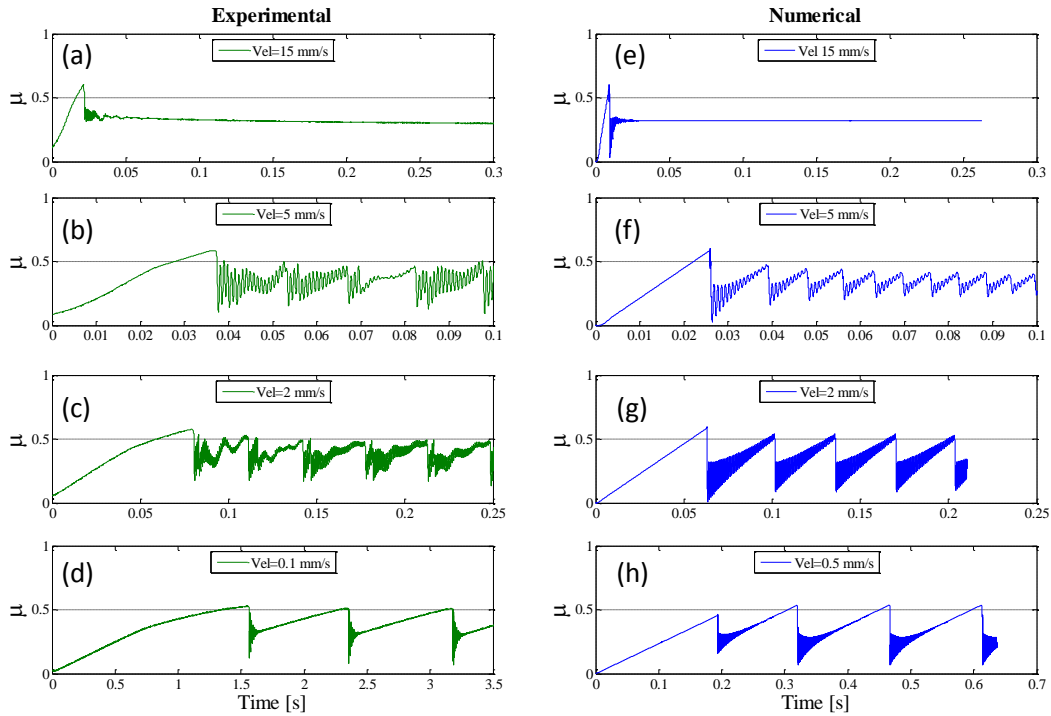


Figure V: Coefficient de frottement macroscopique expérimentale (à gauche) et numérique (à droite), en fonction de la vitesse imposée ; pression de contact moyenne de 5 MPa.

Les résultats numériques peuvent ensuite être utilisés pour associer chaque réponse au frottement macroscopique du système au comportement local du contact (propagation d'onde, fronts de rupture au contact, adhérence-glissement-séparation et évolution de l'interface), qu'il n'est toujours pas possible d'étudier expérimentalement. En outre, l'accessibilité au contact par instrumentations optiques et acoustiques permet des analyses futures de la rupture et de la propagation des ondes au contact pour valider les résultats des simulations numériques à la zone de contact.

Mots-Clés: frottement sec, instabilités dues au frottement, stick-slip, couplage modale, dynamique de contact, analyse expérimentale, simulation numérique du contact.

Macroscopic frictional contact scenarios and local contact dynamics: at the origins of “macroscopic stick-slip”, mode coupling instabilities and stable continuous sliding

Abstract

Local contact behavior and its interaction with the global dynamics of the system are at the origin of innumerable contact issues concerning several different disciplines like tribology, geophysics, vibration mechanics or fracture mechanics.

When two elastic media are in relative motion with a frictional interface, friction induced vibrations arise into the system. By a macroscopic point of view, the “macroscopic stick-slip” scenario occurring during relative motion is characterized by sudden friction force drops (sliding state) along the time, separated by periods of elastic energy accumulation (stick state). Instead, the mode dynamic instability occurs when a vibration mode of the mechanical system becomes unstable, due to frictional contact forces. This kind of instabilities, generated by frictional forces, have been mainly object of papers dealing with specific issues in different domains such as brake squeal, hip endoprosthesis squeaking, wheel-rail vibrations, earthquakes, etc.

In this context, experimental and numerical analyses have been focused here on understanding how the local interface behavior affects the macroscopic frictional response of the system, and, conversely, during instability scenarios.

The macroscopic frictional scenarios (macroscopic stick-slip instability, mode coupling instability, stable continuous sliding) arising between two simple elastic media in relative motion have been investigated numerically and experimentally. A newer experimental setup (TRIBOWAVE) has been developed and it allowed to reproduce and to investigate the different scenarios under well-controlled boundary conditions.

The same frictional scenarios have been reproduced by transient numerical simulations. A dedicated friction law as a function of adherence (sticking) time has been recovered by means of experimental tests. The obtained friction law has been implemented in the numerical model, leading to a quantitative validation of the simulated scenarios by the experiments.

Nonlinear transient simulations, complex eigenvalue analyses and experimental tests allowed for drawing instability maps as a function of system key parameters.

The numerical model, validated by the comparison with the experimental global measurements (forces, accelerations/velocity), allowed for investigating the coupling between the local contact behavior (contact status distribution, wave and rupture propagation, precursors) and the system dynamic response

during macroscopic stick-slip instability, mode coupling instability and stable continuous sliding.

The understanding of the coupling between contact and system dynamics will bring to further improvements on the control of contact instabilities and related wear issues.

Key-words: dry friction, friction instabilities, stick-slip, mode coupling, contact dynamics, experimental analysis, numerical contact simulation.

Summary

<i>Introduction</i>	<i>1</i>
<i>1 Frictional contact dynamics</i>	<i>4</i>
1.1 Generalities on friction induced vibrations	4
1.2 Macroscopic stick-slip instability	6
1.3 Dynamic instability	11
Negative slope of friction coefficient-sliding velocity	12
Sprag-slip theory	12
Modal coupling: mode lock-in theory	13
1.4 Stable friction induced vibrations	16
1.5 Concluding remarks	17
<i>2 Numerical tools for contact analysis</i>	<i>18</i>
2.1 Introduction	18
2.2 Transient non-linear contact analysis	18
2.2.1 Geometry and material properties	18
2.2.2 Finite element formulation	19
2.2.3 Contact algorithm and friction laws	21
Amontons-Coulomb law	22
Adherence time friction law	22
2.3 Complex eigenvalue analysis	25
<i>3 Experimental tools: test bench, materials and instrumentation</i>	<i>27</i>
3.1 Introduction	27
3.2 Test bench for preliminary experimental analysis: PEDEBA	27
3.3 Description of dedicated setup: TRIBOWAVE	29
3.3.1 Components, materials and instrumentation	29
3.3.2 Stiffness and dynamic characterization	32
Tangential stiffness	33
Tangential dynamics	35
<i>4 Frictional scenarios in dry contact: numerical analysis</i>	<i>40</i>
4.1 Introduction	40
4.2 Description of the model	40
4.3 Macroscopic stick-slip instability ($\beta = 5e-10 s$)	42
4.3.1 Effect of mass damping parameter α	45
4.4 Continuous sliding with mode coupling instability	46
4.4.1 High frequency instability ($\beta = 1e-8 s$)	47
4.4.2 Low frequency instability ($\beta = 1e-7 s$)	49
4.4.3 Effect of mass damping parameter α on limit cycle oscillations	51
4.5 Stable continuous sliding ($\beta = 1e-6 s$)	52
4.6 Parametrical complex eigenvalue analysis (CEA)	54

4.7	Coupling between local contact behaviour and system dynamic response	56
4.7.1	Macroscopic stick-slip instability	57
4.7.2	Mode coupling instability	58
4.7.3	Stable continuous sliding	61
4.8	Discussion of results: contact scenario map	62
5	<i>Preliminary experimental analysis and qualitative numerical comparison</i>	65
5.1	Introduction	65
5.2	Materials and method	66
5.3	Frictional observations: role of boundary conditions	67
5.3.1	Macroscopic stick-slip instability	67
5.3.2	Mode coupling instability	68
5.3.3	Stable continuous sliding	70
5.3.4	Discussion on experimental frictional scenario map	71
5.4	Qualitative comparison between experimental and numerical results	73
5.4.1	Numerical model	73
5.4.2	Definition of the friction law	74
5.4.3	Effect of the imposed boundary conditions	77
5.5	Discussion of results	82
6	<i>Analysis of macroscopic frictional scenarios on a dedicated setup</i>	84
6.1	Introduction	84
6.2	Experimental observations	85
6.2.1	Materials and method	85
6.2.2	Frictional scenario maps	87
6.2.3	Frictional instabilities: discussion on the system dynamic response	90
	Macroscopic stick-slip	90
	Mode coupling instability	95
6.2.4	Effect of roughness on the friction coefficient	99
6.3	Numerical analysis	103
6.3.1	Description of the numerical model	103
6.3.2	Validation of the numerical model: the macroscopic frictional and dynamic response	105
6.4	Concluding remarks	110
7	<i>General conclusions</i>	111
7.1	Original contributions	111
7.2	Future works	112
8	<i>References</i>	114

Summary

Introduction

The frictional contact dynamics is an old and relevant issue in different disciplines as tribology, earth science, vibrational mechanics or fracture mechanics. A first important contribution to the understanding of dry friction was achieved by Leonardo da Vinci (1495); he was the first engineer who introduced the term of friction coefficient. A few centuries later, Amontons [1] and Coulomb [2] improved the concept of friction between solid bodies in relation to contact material pairs, surface composition, lubrication, humidity and temperature. In history, frictional phenomena were earlier and more fundamentally examined in comparison to pure contact mechanical aspects.

In the last decades the development of experimental and numerical simulation methods for investigating frictional processes have produced a sudden growth in the number of research activities considering not only the contact aspects but also the response of the system to which the contact surfaces belong. Godet [3] and Berthier [4] introduced the “third body concept” into the study of frictional phenomena leading to the notation of the “Triplet Tribologique”. This approach highlights how the contact between two frictional surfaces is influenced by the third body, which can be a solid, liquid or gas film interposed between the contact interfaces during sliding, by the response of the solids in contact and by the mechanism (dynamics of the system); thus the analysis of contact issues involves the interaction of various phenomena at different scales.

Furthermore, understanding the physical mechanisms involving the coupling between local (contact scale) and system dynamics (structure scale) during frictional relative motion is of great importance to many research and industrial applications. These mechanisms, related to both the contact and structure scales, can compromise the correct functioning of systems having interfaces in contact. Many recent papers dealt with specific issues of complex systems, like brake squeal [5-9], instability of clutch discs [10], joint fretting [11], earthquake faults [12], tactile perception [13], or hip endoprosthesis squeaking [14, 15] in order to control or predict the effects of friction induced vibrations in each particular case. Many papers in different domains have been dedicated to study the instabilities of systems excited by frictional contact forces, following approaches focused at the contact scale (interface waves and rupture fronts [16-18], precursors [19, 20], wear and third body [21]) or focused on the global response of the system (unstable modes [22], friction induced vibrations [23], macroscopic stick-slip [24-26]). However, a general approach, allowing to reproduce and investigate different kind of frictional behaviours as a function of the system parameters, has not been still formulated.

In this context this thesis is addressed to the investigation of the different mechanisms at the origin of different frictional contact scenarios when two simple elastic media are in relative motion, as a function of key system parameters (boundary conditions, friction coefficient, materials in contact, material damping, etc.). This work wants to provide insights on how the coupling between local (contact) behaviour and global (system) dynamics is at the origin of the different contact scenarios arising in frictional systems. While the numerical simulations have been developed for the investigation of the local physical phenomena (contact status, rupture and wave propagations, etc.), impossible to be measured appropriately, and the coupling with the system dynamic response, the experimental results allowed for validating the numerical findings. Both experimental and numerical simulations allowed for drawing frictional scenario maps as a function of the accounted parameters.

The work presented in this manuscript was aimed to both investigate the physical phenomena and develop the numerical and experimental tools necessary for the investigation. Because of this, after a first overview of the used numerical and experimental tools, a numerical analysis and a preliminary experimental one are described to get the main insights of the phenomena. Then, once the experimental set-up and numerical model have been updated to allow for a finer analysis, a quantitative comparison between experiments and simulations is presented. The work is organized in four main parts.

The first part (chapter 1) presents an overview of frictional contact dynamics issues, focusing the attention to the instabilities that can arise between two bodies in relative motion. Then (chapters 2 and 3), the numerical and experimental tools used to perform the numerical and experimental investigations of two simple elastic media in relative motion are described; the numerical model, the experimental set-up, the materials and the methods used to perform the analyses are presented in detail.

The second part (chapter 4) presents a first numerical analysis dealing with the effect of the material damping on the frictional response of two elastic bodies in relative motion separated by a frictional interface. The approach adopted in contact mechanics is coupled with the structural dynamics analysis of the mechanical system. Both non-linear transient simulations, performed considering large transformations, and complex eigenvalues analyses led to reproduce and investigate the different scenarios occurring when the frictional forces excite the system. The numerical analysis highlighted as the same mechanical system can switch from macroscopic stick-slip instability to continuous sliding with or without mode coupling instability, as a function of the material damping parameters. A numerical map of the frictional scenarios has been drawn. The different scenarios have been analysed focusing the attention both at the contact interface (status of the interface, propagation of

contact ruptures and waves) and at the system dynamic response (mechanical vibrations due to the mode coupling, macroscopic stick-slip).

In the third part (chapter 5) a preliminary experimental analysis has been performed in order to carry out a first qualitative comparison between experimental and numerical results on the global response of the system. The transition from macroscopic stick-slip up to continuous sliding with or without unstable vibrations of the system has been highlighted both experimentally and numerically as a function of the boundary conditions (normal contact force and driving velocity). The frequency and time analysis of the experimental measurements exhibits a good agreement with the numerical results obtained by transient contact simulations.

The last part of the thesis (chapter 6) deals with the experimental campaign on the newer dedicated setup (TRIBOWAVE), and the respective experimental and numerical results. A stiffness and dynamic characterization of the newer setup has been performed by means of preliminary experimental tests (section 3.3.2). Then, the main dynamic characteristics of the setup have been implemented into the numerical model in order to consider not only the contact samples but the more complex dynamic of the system. Experimental tests on the newer setup and numerical simulations with the updated numerical model allowed for a quantitative comparison between experimental and numerical results, validating the numerical findings.

Finally, a conclusive section is dedicated to the discussion of the original contributions and the outlines from the presented work.

1 Frictional contact dynamics

1.1 Generalities on friction induced vibrations

Frictional vibrations are induced in the system when two contact surfaces are in relative motion to each other. Frictional contact between two elastic media can give rise to diverse forms (frequency spectrum and amplitude) of system oscillations, which often lead to have a strong interaction between the local contact dynamics and the structure response.

The frictional contacts and the frictional response of two materials in contact is an old [1, 2], tricky and multidisciplinary issue, which involves different disciplines such as vibration mechanics, contact mechanics, fracture mechanics, geophysics and tribology.

In [22] Akay presents an overview of friction induced vibrations and related acoustic phenomena, concerning different frictional systems at different scales, from the atomic to the structure scale. Moreover friction induced vibrations are object of research in different domains because of the large amount of involved phenomena.

Friction leads to energy dissipation and, in different applications, the friction can be either minimized for saving energy (e.g. joints with bearing) or maximized for dissipating energy or avoid sliding, such as for example between the tires and the road or during braking. While a large amount of energy is dissipated directly at the contact, a part of the energy is returned to the system into the form of induced vibrations; the system responds through its own dynamics storing and dissipating energy by vibrations and material damping [24, 30].

Furthermore, understanding the physical mechanisms that drive the onset and the evolution of sliding between two media is of great importance to many research and industrial applications such as disk brake squeal [6, 8, 9, 31-33], hip endoprosthesis vibrations [15, 34], wheel-rail vibrations [35] and noise emission [5, 36, 37], machining tool vibrations [38], earthquakes [20, 39], tactile perception [13, 40], etc. A review about friction induced vibrations concerning several engineering applications is presented in [23].

As a function of the specific issue or discipline, in the literature the behaviour of bodies in frictional contact are often investigating by either a macroscopic (nonlinear dynamics) or local (tribology) point of view, as a function of the applications or the focused phenomena.

For instance some recent papers deal with frictional models characterized by few degrees of freedom and rigid/deformable contact behaviour [41, 42]. This kind of modelling is useful to better investigate the global non-linear dynamic response of the system without accounting for local phenomena (e.g. contact dynamics, wear [4], plasticity, third body [4, 43], local impact [44]) by means of specific “macroscopic” contact laws or constitutive interface models [45, 46].

Different numerical approaches are presented in literature, from system with few degrees of freedom up to continuous systems with rigid/deformable contact interface; the main aim of these studies is the understanding of the global response of the system during the frictional motion [42]. In [47] a linear and non-linear analysis of a multi-degrees of freedom system shows the existence of limit cycles, quasi-periodic and even chaotic behaviour during steady relative motion. Minimal and analytical models [48-50] have been proposed for understanding the role of the system key parameters, such as damping or friction coefficient, on the time and frequency response.

Recently other works showed as the frictional behaviour is not exclusively a property of the materials in contact [51] and the system dynamics, but it is a more complex phenomenon that involves processes at different scales (from atomic to system scales) [52, 53]. Adams [54-56], considering a continuum approach, investigated the sliding of two elastic half spaces with imposed constant friction coefficient at the interface. He found that local ruptures can propagate along the contact interface. The system is characterized by stick-slip motion due to the rupture propagations at the interface and allowing the bodies to slide with an apparent coefficient of friction which is lower than the coefficient of friction imposed at the interface. He highlighted the difference between the apparent/remote friction coefficient (ration between remote shear and normal stress) and the imposed local contact friction, due to the dynamics at the interface.

A more general approach is needed to account for the coupling between the local phenomena (e.g. contact dynamics) and the system response.

Baillet et al. [57, 58] showed some first works dealing with the coupling between local and contact dynamics considering a finite geometry. They considered a transient non-linear finite element model with constant boundary conditions, showing as the behaviour at the contact zone (stick, slip, separation, stress concentration, local velocity, etc) depends by “dynamic effects” due to

friction induced vibrations. More in general the presence of these instabilities changes drastically the relation between the remote stress applied at the boundaries of the bodies and the stresses distribution at the interface. In addition the local stress can reach extremely larger (or lower) values than the expected ones. Friction dynamics can modify the local kinematics at the surface and consequently the distribution of the contact pressure, the shear stress, the local deformations and the tribological state of the contact zone [57-59]. Consequently the local dynamic processes can cover a key role on the formation of the STTs (Superficial Tribological Transformations) [4, 60] as well as in the formation and role of the third body [43, 61].

Even if it would be ambitious to provide a complete classification of friction induced vibrations, a significant (for the present work) classification can be formulated, as a function of the global dynamic response of the system, as follows:

- Macroscopic stick-slip instability [27-29] induced by frictional contacts in elastic systems. Strong vibrations of the system are induced by impulsive excitations due to the sudden drops of the tangential force (macroscopic slip), due to ruptures at the contact interface.
- Dynamic instability of the system. The structural response is characterized by harmonic unstable vibrations of the system, at one of its natural frequencies, excited by the frictional forces.
- Stable vibrations of the system due to the response of the system dynamics to the random excitation coming from the roughness at the interface. Even if the system is dynamically stable, oscillations of low amplitude with a wide frequency spectrum characterize the system response during the macroscopic sliding motion.

In the next sections a more detailed description of the recent literature on the over-mentioned classes of friction induced vibrations is presented.

1.2 Macroscopic stick-slip instability

When two elastic media are in sliding motion, contact instability phenomena can lead, with respect to the system parameters (friction coefficient, material damping, sliding velocity, contact pressure, material properties, etc.), to strong system oscillations, discontinuous motion (stick-slip) and fastidious noise.

While lumped systems with sliders have been widely used in nonlinear dynamics to investigate the nonlinear dynamic response of rigid masses under

frictional contact and the occurring of stick-slip [26, 29, 62] the recent literature shows an increase of works dealing with distributed or continuous models. Some works deal with distributed frictional models (dampers-springs-blocks) in order to simply the system dynamics and understanding the parameters that play a key role into the system response.

A minimalistic 1D spring-block model has been proposed by Maegawa et al. [19] to reproduce their experiments about precursors to frictional sliding in the stick-slip regime. A model with a simple Coulomb friction law, showed that the length of precursors is modified when the external normal load is made asymmetric. Amundsen et al. [62] improved the 1D model from Maegawa, developing an analytical prediction for the length of precursors as a function of the applied tangential load.

In [63] a 2D spring-block model for the transition from static to kinetic friction at an elastic slider/rigid substrate interface, obeying a minimalistic friction law, is presented. By using realistic boundary conditions, a number of previously unexplained experimental results on precursory micro-slip fronts are successfully reproduced. From the analysis of the interfacial stresses, they tried to derive a prediction for the evolution of the precursor length as a function of the applied loads, as well as an approximate relationship between microscopic and macroscopic friction coefficients.

In last years the local dynamics (rupture and wave propagation) in frictional contacts has been the subject of experimental and numerical works [20, 26, 64, 65]. Recent experimental works focused the attention on the effect of the local dynamics [18] at the contact interface. In [26], Voisin et al. showed experimental observations of the frictional behaviour of a single crystal salt slider over a large number of deformation cycles. A continuous change is observed from stick-slip to stable sliding as slip accumulates under constant conditions of sliding velocity, normal load and temperature. They also showed that the roughness of the contact interface evolves from randomly rough to some striated morphology.

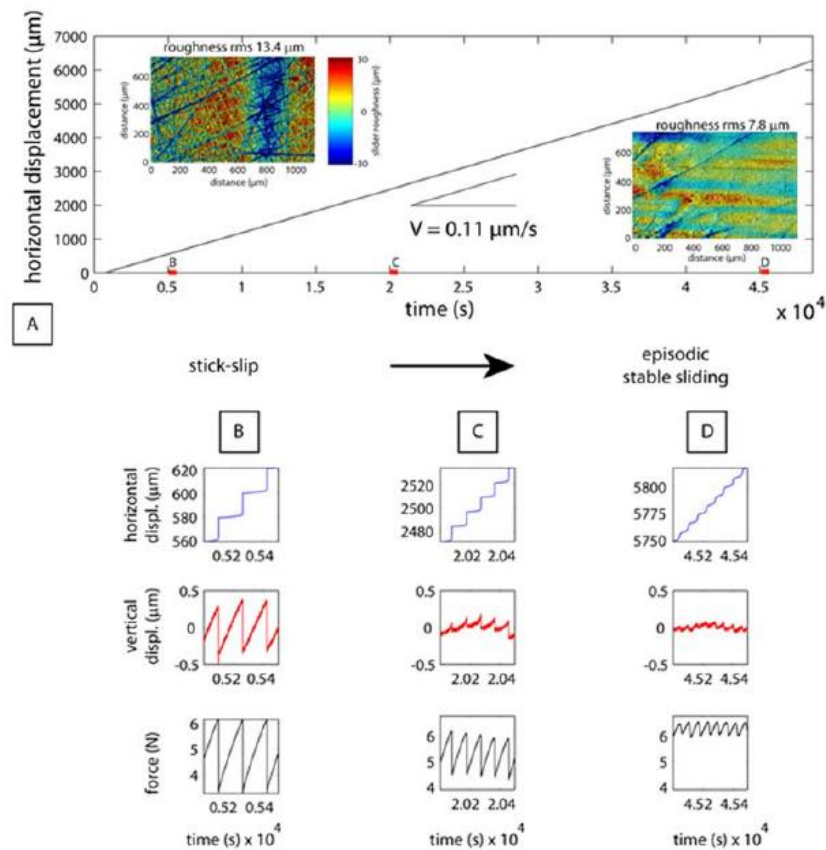


Figure 1-1: (a) Frictional behaviour of salt/glass friction experiment for loading velocity of $0.11 \mu\text{m/s}$ and normal load of 0.26 Mpa . For more specific information see [26].

Zigone et al. [66] showed a systematic correlation between the onset of slip acceleration and the emission of TLS (tremor like signals) in a laboratory friction experiment. TLS are generated when the shear stress reaches the peak static resistance and the interface is close to failure or rupture. The result provides a comprehensive image of how natural seismic tremors might be generated and/or triggered by passing seismic waves or even slow slip events. Typical phenomena of macroscopic stick-slip have been highlighted by the by salt/glass friction experiments (Figure 1-2).

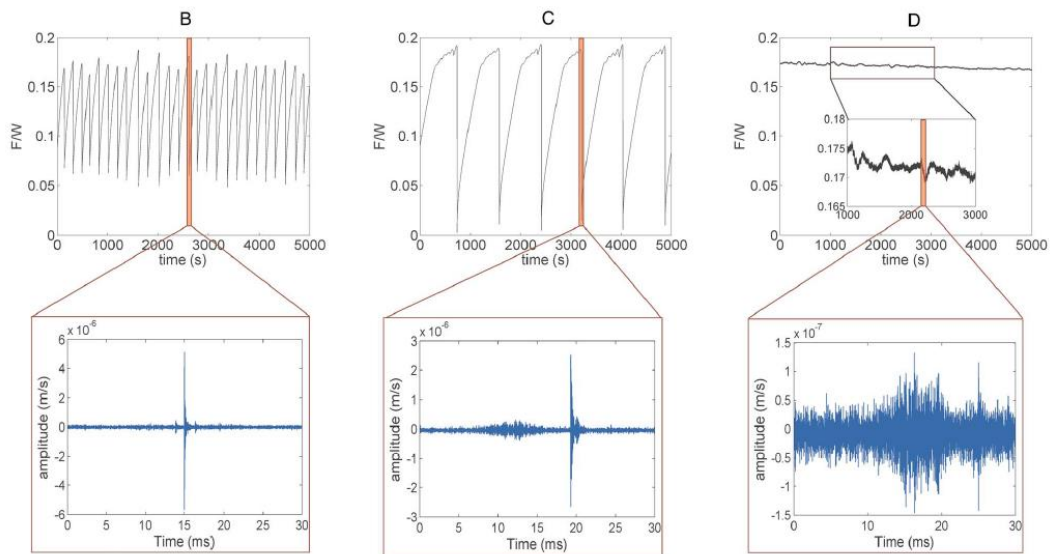


Figure 1-2: Frictional behaviour of salt/glass friction experiment as a function of increasing cumulative sliding. (B) Typical phenomena of stick-slip with sudden tangential force and related acoustic emission. (C) Smooth oscillations of growing amplitude precede the macro-slip event. (D) Stable continuous sliding characterized by small variations of frictional force around a mean value. For more information about the experiment see [66].

In [67] stick-slip has been also observed in articular cartilage under certain loading and sliding conditions. Using the Surface Forces Apparatus, they showed that stick-slip can induce permanent morphological changes (a change in the roughness indicative of wear/damage) in cartilage surfaces, even under mild loading and sliding conditions. The different load and speed regimes can be represented by friction maps, separating regimes of smooth and stick-slip sliding.

Rubinstein et al. in [64] studied the onset of dynamic friction between two blocks of PMMA (polymethyl-methacrylate) separated by a rough interface. They measured the real contact area during the propagation of the ruptures before the overall sliding by means of an experimental apparatus. They observed that the dynamic rupture is governed by crack-like detachment fronts and after each detachment front the net contact area is reduced. Two kinds of these fronts propagate at subsonic and intersonic velocities; a third type of front, which propagates an order of magnitude more slowly, is the dominant mechanism for the rupture of the interface. No overall motion (sliding) of the blocks occurs until either of the slower fronts traverses the entire interface.

In [20], Rubinstein et al. measured the spatial and temporal behaviour of the true contact area along a rough spatially extended interface between two blocks in frictional contact. A sequence of cracklike precursors preceded the global sliding of the contact interface, which are initiated at shear levels that are well

below the threshold for static friction. These precursors arrest traversing the entire interface.

In [68] Kammer et al. investigated the evolution of heterogeneous stress states along frictional interfaces. They used a finite element simulation in order to model the occurrence of precursory slip sequences on a deformable-deformable, as well as a deformable-rigid, interface between two solids. In addition to the linear slip-weakening friction law, the frictional strength is regularized using a simplified form of the Prakash–Clifton law [16]. The delay parameter of the frictional strength has been chosen sufficiently small compared to the typical duration of a slip event [16, 69]. They showed that at the tip of each arrested rupture (precursor) is created and then it is erased to the passage of the following rupture. The bulk viscoelasticity is at the origin of this history effect.

Recently Andrews et al. [70] investigated the frictional dynamics between two identical elastic-viscoplastic solids. Depending on bulk material properties, interface properties and loading conditions, frictional slip along the interface can propagate in a crack-like mode, a pulse-like mode or a train of pulses mode.

Considering the interaction between local contact behaviour and system dynamics (vibration modes), Di Bartolomeo et al. presented in [17] the results obtained from a 2D non-linear finite element analysis of the evolution of sliding between two dissimilar isotropic elastic bodies separated by a frictional interface. Results from the numerical parameter space study showed how the system parameters affect the local dynamics. Consequently, the local dynamics affects the macroscopic frictional behaviour of the system and excites the system dynamic response. The approach used typically in geophysics to follow the wave generation and propagation at the contact interface is coupled with the structural analysis of the bodies in contact. Figure 1-3 shows the complex processes at the contact interface during the onset of the sliding. Different types of contact ruptures and at different speeds cross the interface, reaching the boundaries and then reflecting inside the bodies that respond with their own dynamics.

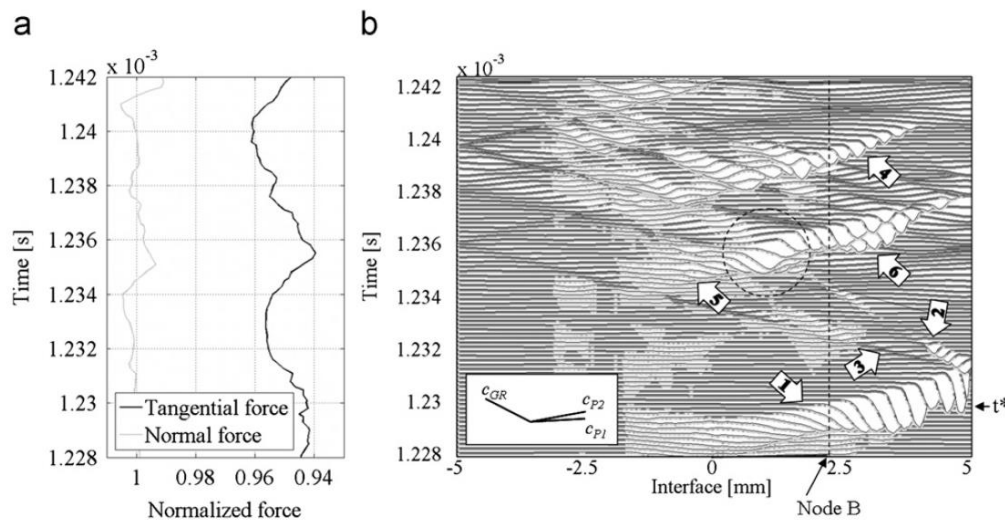


Figure 1-3: (a) Zoom of normalized contact force as a function of time and (b) seismic horizontal velocity profile for the same interval at the onset of the sliding (from [17]).

The main numerical results obtained in [17] can be qualitatively compared with the experimental results presented in [20, 29, 64]. Obviously comparison between experimental and numerical results needs a critical analysis with respect to the difference between numerical and experimental models.

1.3 Dynamic instability

In the previous section, the more recent works on macroscopic stick-slip instability, related to the interface rupture and propagation/generation of contact waves, have been presented. On the other hand, this section wants to give an overview of the main works dealing with the dynamic modal instabilities in frictional contacts and focusing the attention to the macro-scale (system scale) aspect of the issue. In fact, in most of the cited works, the global system response is investigated, while the local contact dynamics is not usually focused.

In this context, a relevant number of works has been dedicated to investigate different possible mechanisms at the origin of dynamic instabilities occurring in sliding contact: sprag-slip, mode lock-in, negative slope of friction coefficient, etc. In general, they can be considered as particular cases of friction induced vibrations, in which the system dynamics results to be unstable and is excited by the contact forces. These works are aimed to understand the causes and key factors in order to give a solution for some practical issues such as disc brake squeal, clutch instabilities, hip endoprosthesis squeaking, etc..

In the following, the main features of the mentioned theories are resumed; a more complete and detailed description can be found in [7].

Negative slope of friction coefficient-sliding velocity

A simple mechanical system where the friction coefficient is a decreasing function of sliding velocity has been investigated by Mills [71].

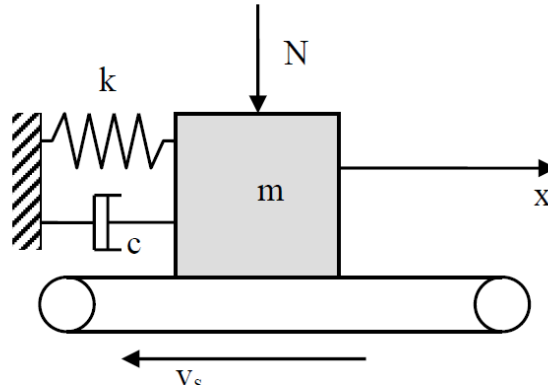


Figure 1-4: Spring-mass-damping system with a moving surface.

Considering a friction coefficient law as a linear function of sliding velocity, the governing equations of the system in Figure 1-4 can be written as follows:

$$m\ddot{x} + c\dot{x} + kx = \mu_1 N - \mu_2(v_c - \dot{x})N$$

$$\mu(v_r) = \mu_1 - \mu_2 v_r$$

Where m is the mass, k is the spring, c the viscous damping and x is the tangential displacement of the mass around the equilibrium position.

The term of the friction force that is proportional to the velocity of the mass introduces an additional term to the damping coefficient and brings to an “apparent” damping value that can result to be negative, bringing to self-excited vibrations of the unstable system.

Sprag-slip theory

In 1961 Spurr realized that unstable oscillations of the system can be produced even when the friction coefficient is independent of the sliding velocity [72].

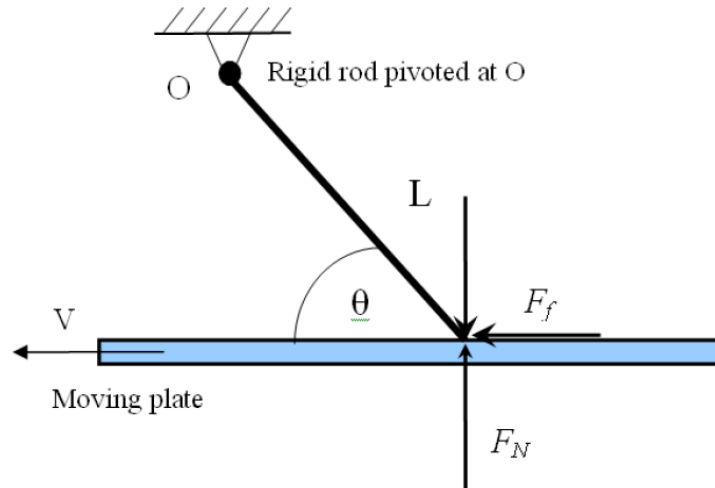


Figure 1-5: Schematic diagram of sprag-slip theory [73].

In describing this mechanism, Spurr presented a semi-rigid structure that is inclined at an angle θ to a rubbing surface and pushed horizontal to the surface, as shown in Figure 1-5. Assuming $F_f = \mu F_N$ and considering the equilibrium of the system, the following equation is derived:

$$F_f = \frac{\mu L}{1 - \mu \tan(\theta)}, F_N = \frac{L}{1 - \mu \tan(\theta)}$$

where μ is the coefficient of friction and L is the load. It can be seen that the friction force (F_f) will approach infinity as μ approaches $\cot(\theta)$. When $\mu = \cot(\theta)$ the system “sprags” or locks and the surface motion become impossible. In this simple way Spurr explained the loading cycle that could bring to the limit-cycle of self-excited vibrations.

Modal coupling: mode lock-in theory

In 1972 North investigated self-excited vibrations considering an eight-degrees-of-freedom model, where the contact forces are considered as follower forces and the friction coefficient as a constant value.

The equations of motion of the system can be written as:

$$M\ddot{x} + K_{AS}x = 0$$

with M the mass matrix and K_{AS} the stiffness matrix.

The introduction of the frictional contact forces lead to have an asymmetric stiffness matrix. When the equilibrium of the system is stable the eigenvalues consist of complex conjugate purely imaginary pairs (or with negative real part if damping is introduced in the model). Varying the parameters of the system, it

is possible that two eigenfrequencies (imaginary part) tend to approach each other until they reach the same frequency at the lock-in point (Figure 1-6). Then the real part of the two coupled eigenvalues split, and one of the modes of the pair can result to have positive real part, i.e. negative damping. On the other hand in the lock-out point the two eigenfrequencies of the system return at distinct values assuming again real part equal to zero in the case of nil damping (Figure 1-6).

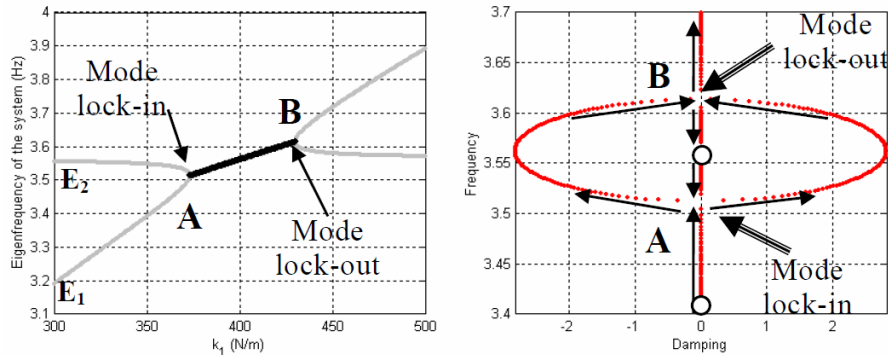


Figure 1-6: Complex eigenvalue analysis of 2 dof model of North [74].

Generally, in real frictional systems, the mechanisms explained above can occur simultaneously, so that an exact separation of these effects is often difficult.

By the way, among these approaches, the modal coupling theory (mode lock-in) is one of the most accepted for specific issues like brake squeal and the complex eigenvalues analysis is a popular numerical tool for dynamic instability prediction. In the last years a huge amount of numerical and experimental works related to brake squeal have been presented. In fact the study of self-excited oscillations, by the mode coupling theory, has its origin in the brake squeal issues. In order to investigate the origin of the mode coupling and its key factors investigations on both real brake systems [75] and simplified laboratory systems [76] have been developed through experimental, numerical and semi-analytical [50, 77] approaches.

Hoffmann in [48] presented a qualitative and quantitative study of the mode-coupling instability in the presence of structural damping, which will be assumed as linear viscous. It is shown that under specific conditions the mode-coupling instability may be regarded as a viscous instability in the sense that an increase in structural damping may render a stable system unstable. Thus the role of damping can be clarified in a two-degree-of-freedom model.

Other researchers studied the effect of damping both in simple minimal models [49] and in more complex systems [9, 78, 79]. Sinou et al. in [49] investigated a non-linear-two-degree-of-freedom system, replacing contact

nonlinearities with contact nonlinear stiffness. The results indicate the existence of, in some cases, an optimal structural damping ratio between the stable and unstable modes which decreases the unstable region. The distribution of damping on the system components and the propensity of the brake to develop squeal is investigated by Massi et al. [80] (Figure 1-7). The obtained numerical results are validated by the experimental ones, presented in [81]. The behaviour of the system eigenvalues highlights that, while a homogenous distribution of damping stabilizes the system, a non-uniform repartition of damping can increase the squeal propensity.

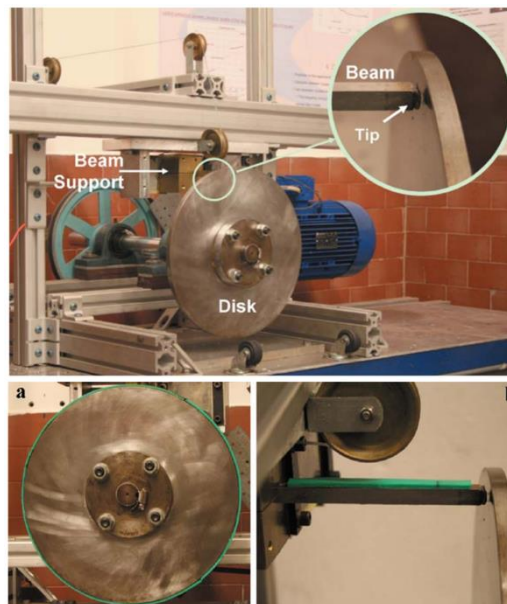


Figure 1-7: Experimental setup used to investigate the effect of damping by Massi et al. [81].

Magnier [50] presented a model defined by a disc and a pad connected via distributed springs (contact stiffness). A static equilibrium has been solved before performing the complex eigenvalue analysis. The results demonstrate that the introduction of heterogeneities can modify the dynamic behaviour of the system. Moreover, the influence of the size of the heterogeneities has been studied and the results show the influence of this parameter in the squeal occurrence.

Friction induced vibrations has also been highlighted in biomechanical systems, applying the same approach used for brake squeal noise (mode coupling theory). Researchers [34] analysed self-excited vibrations and fastidious noise (squeaking) from hip endoprosthesis systems. A combined experimental and numerical study reveals that certain configurations can become unstable causing high frequency oscillations with considerable amplitude

(Figure 1-8). Complex eigenvalue analysis has been performed to individuate critical parameters and influence factors to help endoprosthesis design.

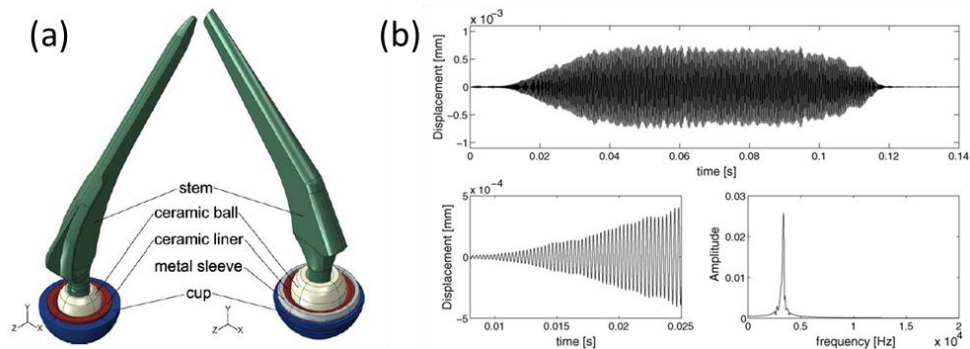


Figure 1-8: (a) Hip endoprosthesis system. (b) Experimental results obtained in vitro on the ceramic ball [34].

1.4 Stable friction induced vibrations

Friction induced vibrations can also arise during sliding when a system frictional instability (detailed in the previous sections) doesn't occur. The main mechanism at the origin of this kind of vibrations is the interaction of asperities at the interface. The roughness and materials at the frictional interface characterize the local excitation and thus the interaction with the system response (system vibrations). In this case a response at the natural frequencies of the frictional system characterises the friction induced vibrations. This kind of behaviour produce an acoustic emission referred in literature as roughness noise [22]. An example of roughness noise involving corrugated surfaces sliding over each other under normal load, is presented, producing impulsive contact forces generating an excitation in each direction; the response spectrum is characterized by a combination of the natural frequencies of the system and the frequency corrugations.

Several numerical and experimental works [13, 82-84] deal with friction induce vibrations related to surface roughness, focusing the attention to the global response of the system and the acoustic emission. By the acoustic point of view, Othman et al. [83] carried out an experimental investigation of the roughness noise generated from the sliding of a stylus over a frictional surface, analysing the sound pressure level for different material surface roughness. The frequency and sound level has been studied for concentrated contacts (stylus over a surface). On the other hand Stoimenov et al. [84] clarified the effect of surface roughness on the frequency of non-squealing frictional sound by means of experiments on a distributed dry contact (flat-flat sliding contact). The

structural response (Power spectral density of the sound) highlights as the frequency peaks increases its amplitude with the increasing of the sliding velocity and average contact pressure. Of course, the frictional response due to the surface roughness in such stable frictional system is characterized by relative low amplitude vibrations along the time and a broad frequency spectrum. For a more detail review concerning stable friction induced vibrations, which overcomes the aim of this work, the reader can refer to the over-mentioned papers.

1.5 Concluding remarks

The literature dealing with frictional contact dynamics is really huge and differentiated as a function of the different applications, different investigated phenomena or different disciplinary approaches; this chapter wants to give a generic, but not exhaustive, bibliographical panorama of the recent literature. Detailed literature on specific applications or issues can be found in the different review papers cited in the text.

When dealing with friction induced vibrations, many papers are focused on specific issues of more or less complex systems, in order to control or predict the effects of friction induced vibrations in each particular case. Moreover, as a function of the specific issue and discipline, different time and space scale are accounted for.

However, a general approach, accounting for the different scales (contact and system scale) is needed to generalize the approach and show how a same mechanical system can present the different scenarios of friction induced vibrations mentioned above (stick-slip instability, mode coupling instability or stable continuous sliding), as a function of the system parameters.

2 Numerical tools for contact analysis

2.1 Introduction

This section presents the numerical tools used to carry out the numerical contact analyses concerning the investigation of frictional dynamic scenarios in sliding contact systems. The first part of the chapter deals with the description of the model geometry and the boundary conditions used for the non-linear transient analysis. The considered model allowed for investigating the interaction between global dynamics and local contact behaviour between deformable bodies in relative motion. The used finite element code PLASTD is specific to resolve transient contact dynamic issues. A description of the contact modelling to simulate the local contact behaviour and the adopted friction laws are presented. The second part of the chapter describes the linear frequency analysis and the related formulation for the complex eigenvalue problem for frictional systems; particular interest is addressed to the stability of the system dynamics.

2.2 Transient non-linear contact analysis

2.2.1 Geometry and material properties

The numerical model (2D plane strain deformation) consists of two isotropic elastic finite media separated by a frictional interface. The contact surface is flat and no thermal and physicochemical effects are accounted for. The considered constitutive law associated to the materials is the classical Hooke's law and the only nonlinearity accounted for is the frictional contact. Figure 2-1 shows the basic geometry of the numerical model and the boundary conditions used to carry out the transient non-linear contact simulations. The two bodies are pressed together with a compressive global force F , applied on the lower boundary of body 2. After this first phase of normal (y -direction) pre-loading, a constant horizontal velocity V is applied along the x -direction at the same boundary, while the upper boundary of body 1 is maintained fixed. For the numerical analysis reported in the chapter 4, the dimensions (length L and width W) of the model has been chosen in order to have affordable computational time. On the other hand, to carry out a comparison between experimental and numerical results the dimensions of the model and the material properties have

been updated considering the materials in contact and the dimensions used in the experimental analysis (Chapter 5-6). In the following chapters, the used dimensions and materials are specified.

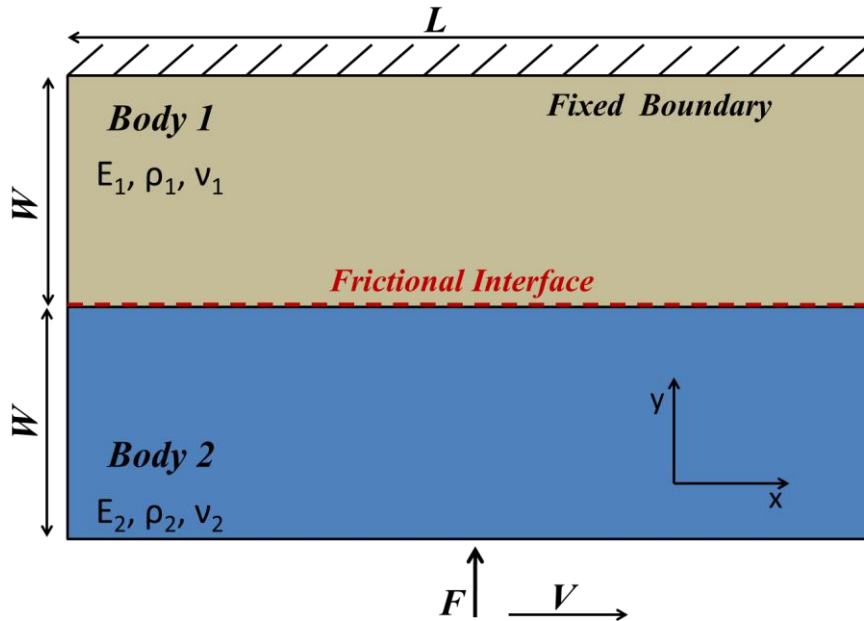


Figure 2-1: Basic geometry and boundary conditions used for the numerical model. F is the compressive global force applied at the lower boundary of body 2 and V is the horizontal velocity imposed at the same boundary of body 2. At each node of the frictional interface is imposed the friction contact law.

2.2.2 Finite element formulation

The explicit finite element code PLASTD [85, 86] is used to perform transient contact nonlinear simulations in order to analyse the interaction between the local contact dynamics and the structural response due to the frictional excitation. This software is designed for large strains, large displacements, large rotations and non-linear contact behaviour using a forward Lagrange multiplier method for the contact between deformable bodies. The bodies are described by a four node quadrilateral elements with 2×2 Gauss quadrature rule and the contact algorithm uses slave nodes and target surfaces. The elementary target segments are described by two nodes and approximated by bicubic splines. A forward Lagrange multiplier method is formulated by the equations of motion at time $t_i = i\Delta t$ with the displacement conditions imposed on the slave node at time t_{i+1} :

$$\begin{cases} \mathbf{M}\ddot{\mathbf{u}}_i + \mathbf{C}\dot{\mathbf{u}}_i + \mathbf{K}\mathbf{u}_i + \mathbf{G}_{i+1}^T \boldsymbol{\lambda}_i = \mathbf{F}_i \\ \mathbf{G}_{i+1} \{ \mathbf{X}_i + \mathbf{u}_{i+1} - \mathbf{u}_i \} \leq \mathbf{0} \end{cases} \quad (1)$$

where \mathbf{M} and \mathbf{K} are, respectively, symmetric and positively defined matrices of mass and stiffness of the system; \mathbf{C} is the Rayleigh proportional damping matrix where α is the mass damping coefficient and β is the stiffness damping coefficient:

$$[\mathbf{C}] = \alpha[\mathbf{M}] + \beta[\mathbf{K}] \quad (2)$$

\mathbf{X}_i is the coordinate vector at time t_i . $\mathbf{u}, \dot{\mathbf{u}}, \ddot{\mathbf{u}}$ are respectively the vectors of nodal displacements, nodal velocities and accelerations. \mathbf{F}_i is the vector of external forces.

$\boldsymbol{\lambda}_i = [\lambda_n \ \lambda_t]^T$ contains respectively the normal and tangential contact forces acting on the nodes at the contact surface, calculated by means of the contact algorithm.

$\mathbf{G}_i^T = [\mathbf{G}_n^T \ \mathbf{G}_t^T]$ is the global matrix of the displacement conditions ensuring non-penetration condition and the friction law at the boundaries in contact. The equations of motion are discretized in time, by using an explicit Newmark scheme.

The vectors $\ddot{\mathbf{u}}_i$ and $\dot{\mathbf{u}}_i$ are expressed at each time step using a time scheme of type β_2 , where $\beta_2 \in [0.5; 1]$:

$$\begin{cases} \dot{\mathbf{u}}_i = \frac{2}{\Delta t^2} (\mathbf{u}_{i+1} - \mathbf{u}_i - \Delta t \dot{\mathbf{u}}_i) \\ \ddot{\mathbf{u}}_i = \frac{1}{1+2\beta_2} \left[\ddot{\mathbf{u}}_{i+1} + \Delta t (1 - \beta_2) \ddot{\mathbf{u}}_{i-1} + \frac{2\beta_2}{\Delta t} (\mathbf{u}_{i+1} - \mathbf{u}_i) \right] \end{cases} \quad (3)$$

The displacements \mathbf{u}_{i+1}^* of the nodes situated on the contact surface are initially computed with λ_i equal to 0. In order to avoid the introduction of numerical damping, β_2 is fixed to 0.5 (central difference method) and the nodal displacements at time t_{i+1}^* are obtained as:

$$\mathbf{u}_{i+1}^* = \Delta t^2 \mathbf{M}^{-1} (\mathbf{F}_i - \mathbf{K}\mathbf{u}_i) + 2\mathbf{u}_i - \mathbf{u}_{i-1} \quad (4)$$

A constraint matrix \mathbf{G}_{i+1} is formulated for the slave nodes if they have penetrated through a target segment. Calculations of contact forces λ_i and nodal displacements at time t^{i+1} are then performed:

$$\begin{cases} \lambda_i = (\Delta t^2 \mathbf{G}_{i+1} \mathbf{M}^{-1} \mathbf{G}_{i+1}^T)^{-1} \mathbf{G}_{i+1} (\mathbf{u}_{i+1}^*) \\ \mathbf{u}_{i+1} = \mathbf{u}_{i+1}^* - (\Delta t^2 \mathbf{M}^{-1} \mathbf{G}_{i+1}^T \lambda_i) \end{cases} \quad (5)$$

The equations are solved using the Gauss-Seidel method [86].

The explicit Newmark scheme coupled with forward Lagrange multiplier method (see section 2.2.3) allows to satisfy more precisely the contact conditions. Furthermore the explicit method allows for better solve problems involving impact and sliding with friction [86] and fast phenomena such wave and rupture propagations at the contact.

A 2D plane strain deformation model has been used to perform numerical contact analyses in order to have reasonable computational time, which is today the main limit into solving the 3D transient non-linear contact simulations.

2.2.3 Contact algorithm and friction laws

The forward multiplier Lagrange method allows to satisfy the non-penetration condition avoiding to choose a supplementary coefficient (contrary to the penalty method) that can affect the local solution; on the other hand the computational effort into resolving the contact forces is major due to the introduction of the unknown supplementary terms and to the algorithm convergence.

The resolution of equation system (1) allows to calculate the displacement vector u and also the vector of the Lagrange multipliers, that represents the contact forces acting on the slave nodes:

$$\mathbf{F}_{t+\Delta t}^C = \mathbf{G}_{i+1}^T \lambda_i$$

During each iteration the following two contact conditions for each slave node k are also checked:

$$I) \quad \lambda_n^k \leq 0 \quad \begin{cases} \lambda_n^k < 0 \text{ (contact)} \\ \lambda_n^k = 0 \text{ (separation)} \end{cases} \quad (6)$$

$$II) \quad \|\lambda_t^k\| \leq \mu \|\lambda_n^k\| \quad \begin{cases} \text{if } \|\lambda_t^k\| < \mu \|\lambda_n^k\| \rightarrow \dot{\mathbf{u}}_t = \mathbf{0} \text{ (stick)} \\ \text{if } \|\lambda_t^k\| = \mu \|\lambda_n^k\| \rightarrow \lambda_t^k \cdot \mathbf{v}_t \leq 0 \text{ (slip)} \end{cases} \quad (7)$$

Where \mathbf{n} and \mathbf{t} are the normal and tangential unit vectors defining the contact, λ_n and λ_t are the normal and tangential contact forces at each node k and μ is the

friction coefficient. The first condition means that the contact force is a compression force (without adhesion components), while the second condition is associated with the use of the defined friction law.

In this work two different friction contact laws have been utilized to carry out the numerical simulations: the Amontons-Coulomb law and a newer friction law, where the friction coefficient is a function of local adherence (sticking) time.

Amontons-Coulomb law

When a slave node comes in contact with the respective target segment, the Amontons-Coulomb law (Figure 2-2) is represented by the equation 7 where μ is the constant friction coefficient and v_t is the tangential relative velocity. Figure 2-2 shows a graphic representation of the Amontons-Coulomb law: first the magnitude of the tangential force cannot exceed the coefficient of friction times the normal force; second the tangential velocity is zero when the tangential force is less than the Coulomb limit. Thus the contact node stays in stick state when $\lambda_t < \mu|\lambda_n|$; otherwise the contact node assumes the sliding state ($v_t \neq 0$) and $\lambda_t = \mu|\lambda_n|$. The element size of the numerical model, which has been used to perform simulations with Amontons-Coulomb law reported in chapter 4, has been chosen considering the mesh convergence analysis performed in [17].

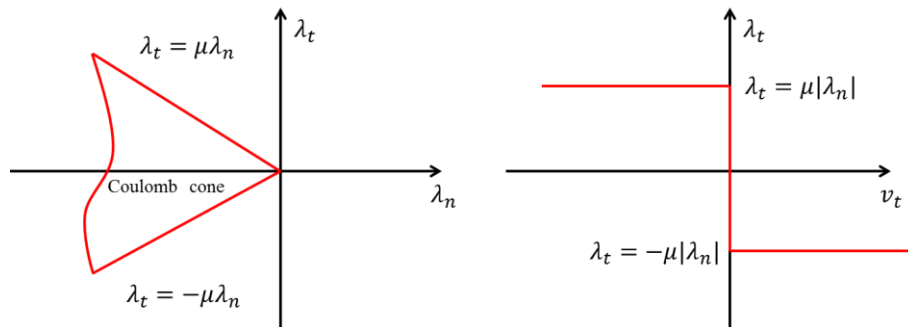


Figure 2-2: Representation of classical Amontons-Coulomb friction law

Adherence time friction law

Considering the friction law as a function of the adherence time, the friction coefficient is not assumed to have a constant value (Amontons-Coulomb friction law). In fact, the experimental frictional analysis, performed on the used materials (polycarbonate and PMMA), highlighted how the friction coefficient shows relevant variations as a function of the adherence time between the two surfaces in contact.

Based on the frictional observations, a more realistic friction model has been implemented in the code. In particular, the value of the macroscopic friction coefficient between the two contact bodies has been observed to be a function of the sticking (adherence) time between the two contact surfaces. It has been

possible to recover an analytical expression of the friction coefficient fitting the experimental data. The new friction model has the following form:

- Before that the contact node switches in sliding state for the first time, the static friction coefficient is assumed to be a constant value:

$$\mu = \mu_0$$

- after that the contact node switches in the sliding condition the friction coefficient follows the analytical expression:

$$\mu(t_{adh}) = A + B \cdot (1 - e^{-C \cdot t_{adh}}) \quad (8)$$

where the t_{adh} represents the adherence time at the contact node;

$A+B$ is the maximum value of the friction coefficient, defined for t_{adh} going to infinite;

A is the dynamic friction coefficient, defined precisely for $t_{adh} = 0$;

C is the parameter influencing the increase or decrease of the friction coefficient in the first part of the friction law shown in Figure 2-3.

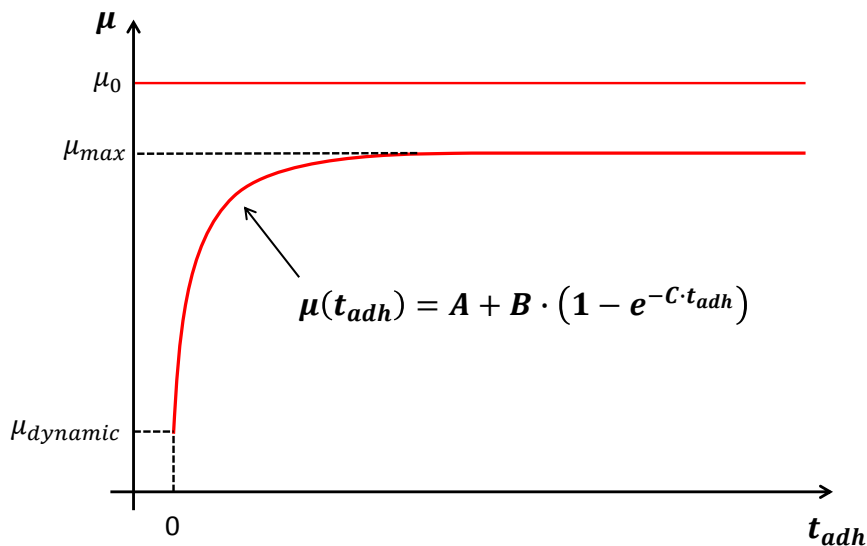


Figure 2-3: Representation of friction contact law: friction coefficient as a function of adherence (sticking) time at the contact node.

This kind of friction law is characterized by a constant value of the static friction coefficient for a long adherence time, corresponding to the limit of the curve in Figure 2-3. On the other hand, for short adherence times, the friction coefficient is governed by an exponential law. In this first zone (short adherence time) the increasing of the friction coefficient is related to the C parameter of the analytical curve (Eq. 8).

Experimental friction data also highlighted how the global friction coefficient is influenced by the initial condition of the contact interface before the first

macro sliding; in the numerical model, the influence of the initial conditions is accounted for by assuming a constant static friction coefficient μ_0 , which is kept only before the first transition of the contact node from stick to slip status. After that, the friction law showed in Figure 2-3 is imposed at each contact node.

Reliable parameters (A, B, C, and μ_0) of the friction law have been obtained experimentally as a function of contact material pairs. The increase of the friction coefficient at the interface with the adherence time can be attributed to the physicochemical surface reactivity of the used materials; the presented frictional law wants to account for the observed behavior, without modelling directly the more complex physicochemical phenomena at the interface.

This new frictional model has been developed in order to perform a quantitative comparison between experimental and numerical results, reported in the following chapters.

On the other hand a mesh convergence analysis has been performed with the new friction law, considering the model geometry reported in section 5.4.2. Figure 2-4 shows the effect of the mesh size on the macroscopic friction coefficient. Non-linear transient simulations have been performed in the case of macroscopic stick-slip instability for three different mesh size (see Figure 2-4). The results from the transient analysis doesn't change as a function of the mesh size, showing the same drop amplitude and oscillations of the friction coefficient. Considering the results of the convergence analysis, the numerical simulations presented in the chapter 5 and 6 have been carried out with mesh size equal to 0.1 mm.

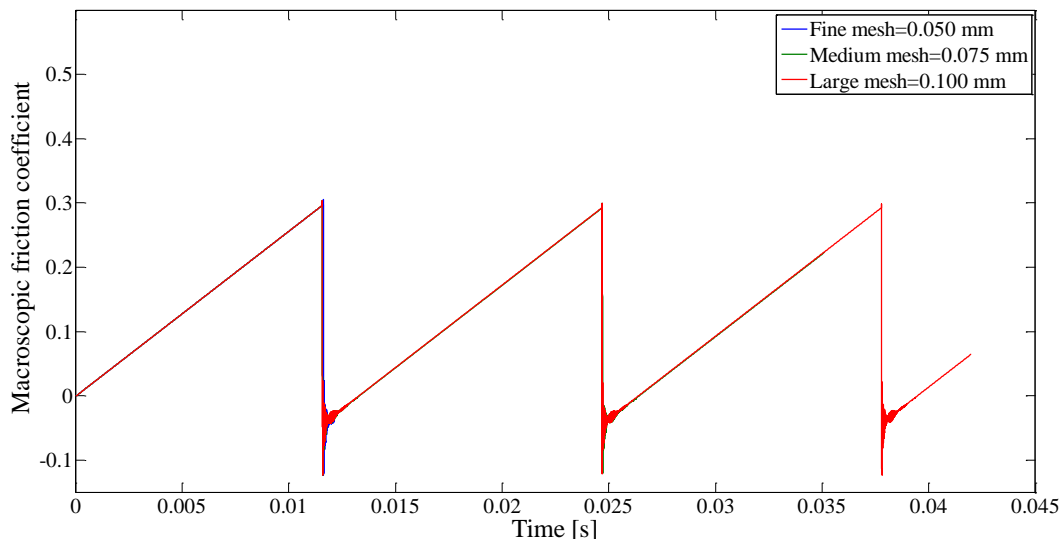


Figure 2-4: Representation of macroscopic friction coefficient for three different mesh size. Parameters of friction contact law: $A=0.1$, $B=0.4$, $C=150$ and $\mu_0=0$. Imposed boundary conditions: driving velocity of 2 mm/s, average contact pressure of 3 MPa, integration time step $dt=1e-9$ s.

2.3 Complex eigenvalue analysis

The complex eigenvalue analysis is the most commonly used technique to investigate the mode coupling dynamic instability involving elastic systems with frictional interfaces.

The commercial finite element software ANSYS is used to perform linear contact analysis and to calculate its complex eigenvalues and eigenvectors as a function of the driving parameters. The model geometry and the boundary conditions shown in Figure 1 have been utilized to carry out the pre-stressed linear frequency analysis. The contact elements CONTA173 and TARGET170 have been introduced to account for the frictional forces at the contact interface.

Before solving the complex eigenvalues analysis, a static analysis has been performed with the following loading condition:

- A vertical load distribution (along y direction), with a total force equal to F , is applied to the lower edge of body 2, bringing the bodies in contact with an average contact pressure equal to 1 MPa;
- Afterwards, an horizontal (along x direction) displacement has been applied at the same edge to bring all the contact nodes of the system in sliding condition.

By solving the preliminary static analysis, the frictional contact forces have been thus introduced in the system at the contact nodes.

The system is then linearized by replacing the contact forces with equivalent contact stiffness terms in the system stiffness matrix. The pre-stressed modal analysis is then performed to account for the system deformation and the contact state in the stationary sliding condition.

The general equation for the considered system, discretized by finite elements, is:

$$(\delta^2 M + \delta C + K_{NS})\phi = 0 \quad (9)$$

This equation represents a non-standard eigenvalues problem, where M is the mass matrix, C is the damping matrix, K_{NS} is the non-symmetric stiffness matrix of the system, δ is the eigenvalue and ϕ is the associated eigenvector. When the frictional contact is accounted for, the K_{NS} contains the supplementary terms due to contact forces at the contact nodes. The lack of symmetry leads to complex eigenvectors and complex eigenvalues. A general eigenvalue can be written as $\delta = \sigma + j\omega$, where the imaginary part is proportional to the angular frequency of the corresponding system mode and real

part is proportional to the modal damping factor of the mode. A positive real part of the eigenvalue means that the mode is unstable (negative apparent modal damping factor). This kind of linear analysis allows for calculate all the possible unstable modes of a system with frictional interface; it allows as well to perform parametrical stability analysis as a function of the system key parameters.

3 Experimental tools: test bench, materials and instrumentation

3.1 Introduction

This chapter introduces the experimental tools used to investigate the frictional scenarios occurring during relative motion between deformable bodies. A description of the experimental setup (PEDEBA), the approach, the materials and the method used to carry out a preliminary contact analysis is first presented.

Then, the second part of the chapter deals with a detailed description of the newer experimental setup (TRIBOWAVE). The fundamental components and the instrumentation needed to investigate the frictional and dynamic behaviour during each performed tests are described.

The tangential stiffness and structural dynamics of the experimental setup is retrieved in order to better characterize the contact dynamic response of the whole experimental test-bench. The dynamic characterization of the set-up allowed for updating the numerical model and carrying out a quantitative comparison between experimental and numerical results (chapter 6).

3.2 Test bench for preliminary experimental analysis: PEDEBA

A first experimental analysis of two bodies in relative motion has been performed on a test bench already present at the LaMCoS laboratory.

This set-up, named PEDEBA, has been used in order to reproduce the relative motion between the two contacting bodies and to investigate the contact macroscopic frictional behaviour between the two elastic media in relative motion under well controlled boundary conditions. The experimental analysis has been realized with the aim of investigating the role of the boundary conditions in the behaviour of the frictional system. A simplified scheme of the PEDEBA setup is reported in Figure 2-1. The setup is rigidly linked at a seismic mass (5000 kg). The lower specimen is bonded along x to the fixed frame and the normal load (along y direction) is applied through a hydraulic piston, controlled in force. The upper specimen is fixed to the mobile part of the set-up that provides the translation displacement (along x direction) through hydraulic cylinders, controlled in position with a linear encoder. A tri-axial piezoelectric

force transducer records the tangential and normal force both in the preload phase and during the relative motion. A piezoelectric accelerometer is positioned on the support of the lower specimen to measure the tangential acceleration during tests (see Figure 3-1). In the first phase of each test, the lower and upper specimens are put in contact applying a compressive normal force F ; afterward a constant velocity is imposed on the upper specimen to bring the elastic blocks in frictional relative motion. The global signals, tangential force, normal force, tangential acceleration and imposed displacement have been recorded with a sample frequency of 50 kHz by an OROS acquisition system. The translational velocity is imposed to the slider block by a linear hydraulic displacement system with high resolution in order to avoid artificial stick-slip phenomena induced by the set-up control system. The set-up allowed for imposing at the system the opportune (constant) boundary conditions in order to obtain reproducible results and to perform a comparison with numerical results.

An experimental parametrical analysis, as function of the relative velocity and the normal load, has been performed. This set-up allowed for observing different macroscopic frictional behaviours when two simple elastic media are in relative motion under frictional contact.

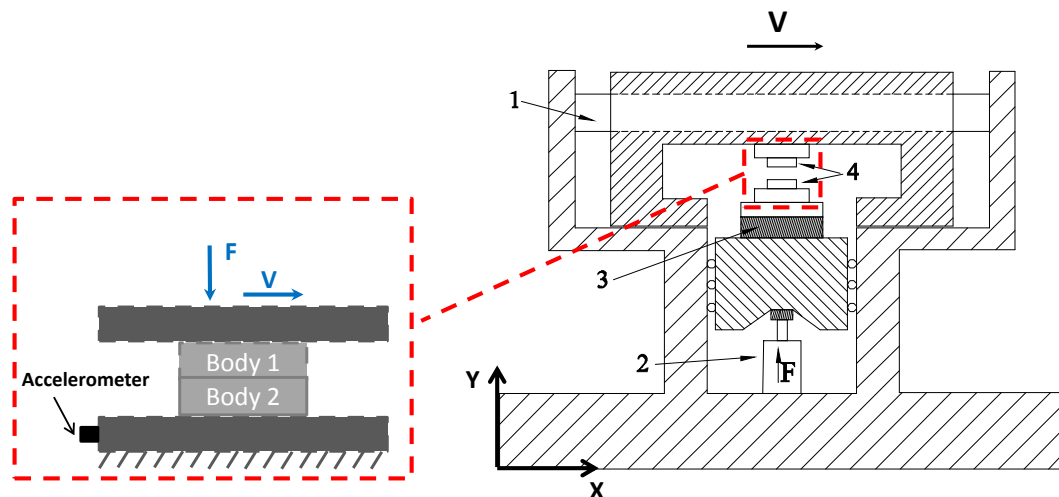


Figure 3-1: A general scheme of the experimental set-up PEDEBA: 1- Hydraulic cylinder, 2- Hydraulic piston, 3- Force transducer, 4- Specimens.

3.3 Description of dedicated setup: TRIBOWAVE

3.3.1 Components, materials and instrumentation

This section presents the experimental tribometer, named TRIBOWAVE, designed and developed at the LaMCoS laboratory. This setup is dedicated to reproduce and investigate the system response and the contact behaviour of two bodies in frictional sliding in a wide range of controlled boundary conditions.

The study of contact instabilities involves difficulties related to the fast and high frequencies contact phenomena and their interaction with the system dynamics. The test bench has been designed to guarantee the measurement reproducibility and to perform measurements limiting the noise and additional vibrations relative to sliding contact between other parts of the setup. The developed setup is able to apply an arbitrary chosen relative displacement or velocity between the two elastic body (constant, sinusoidal, etc.); the real displacement, the macroscopic frictional forces (tangential and normal) in time and the system structural response during the relative motion can be measured accurately. More in general the experimental setup allows for examine the contact dynamics and the system response for different geometries, contact surfaces and materials in contact. The set-up has been developed in order to obtain quantitative comparison between the experimental tests and the numerical simulations, allowing for reproducing the instability scenarios and to investigate the interaction between the macroscopic dynamic response of the system and the local dynamic behaviour at the contact interface.

Figure 3-2 represents a lateral and frontal view of the newer experimental setup. The experimental machine has been designed in order to impose boundary conditions in a large range of the controlled parameters (normal load, imposed driving velocity, etc.), avoiding artificial contact scenarios due to a bad controlling of the system. The main functional components of the experimental setup are:

- **The hydraulic cylinder and high pressure pump (ENERPAC)** allowing for bringing the two bodies in contact with a well-defined contact pressure; a maximum normal force (along z direction) of about 15000 N can be applied. The permitted maximum displacement in the z direction is of 100 mm. Different specimen geometries and different materials can be analysed and a wide range, both in terms of normal force and vertical displacement, can be imposed to perform the experiments.
- **The four linear electromagnetic motors (ETEL of type LMA22-100)** have been assembled in parallel in order to obtain a maximum

tangential force (x direction) equals to 10000 N with a maximum allowed tangential displacement of 20 mm. This kind of system allows for imposing very low driving velocity (down to 1 $\mu\text{m/s}$). Direct coupling of the payload to the motor's moving part eliminates the need for mechanical transmission elements such as lead-screws, timing belts, rack and pinion, and worm gear drives. Unlike in classical system, there is no contact between the moving components in a direct drive system avoiding vibrations due to the presence of contact parts.

- **The linear encoder (HEIDENHAIN of type LIP-200)** consists of a scale tape and a scanning head that operates without mechanical contact. The scale of an exposed linear encoder is fastened directly to a mounting surface. The linear encoder is designed for using on machines and installations that require especially high accuracy of the measured displacement. The resolution of the considered linear encoder is of 1nm. This resolution allows for applying a well-controlled relative displacement between the mobile and fixed part of the setup.
- **The position controller (ETEL)** allows for driving in current the electromagnetic linear motors. By feeding back the position signal (linear encoder) into the controller with an high speed communication through the ETEL real time bus, a desired displacement (velocity) can be imposed to the mobile part of the setup.
- **A precision rail guide (SKF)** is the only part of the whole system characterized by components in rolling contact. The guide is arranged in pairs and the cage containing the rolling elements is located in between; an high stiffness and a very load carrying capacity with a compact design make the guide appropriate for high precision (2 $\mu\text{m}/1000\text{ mm}$) of position measurements. By the way this component, allowing for having a relative rigid motion between the fixed part and the mobile part of the motors, is far away from the contact surface; a large mass of the mobile part (about 80 Kg) allows for filtering eventual parasitic noise coming from the rolling contact.
- **The 3D component force transducer (KISTLER of type 9067)** allows for measuring the three orthogonal components of dynamic and quasi-static forces acting between the two contact surfaces. The transducer is characterized by a high stiffness, high sensibility and fast dynamics, ensuring to measure vibrations and friction force also in specific conditions such as impulses or fast force ramps.
- **The sample supports** have been designed in order to carry out experimental test with different sample geometry (width, height, depth). In this manner experimental tests as a function of various geometry can be easily performed.

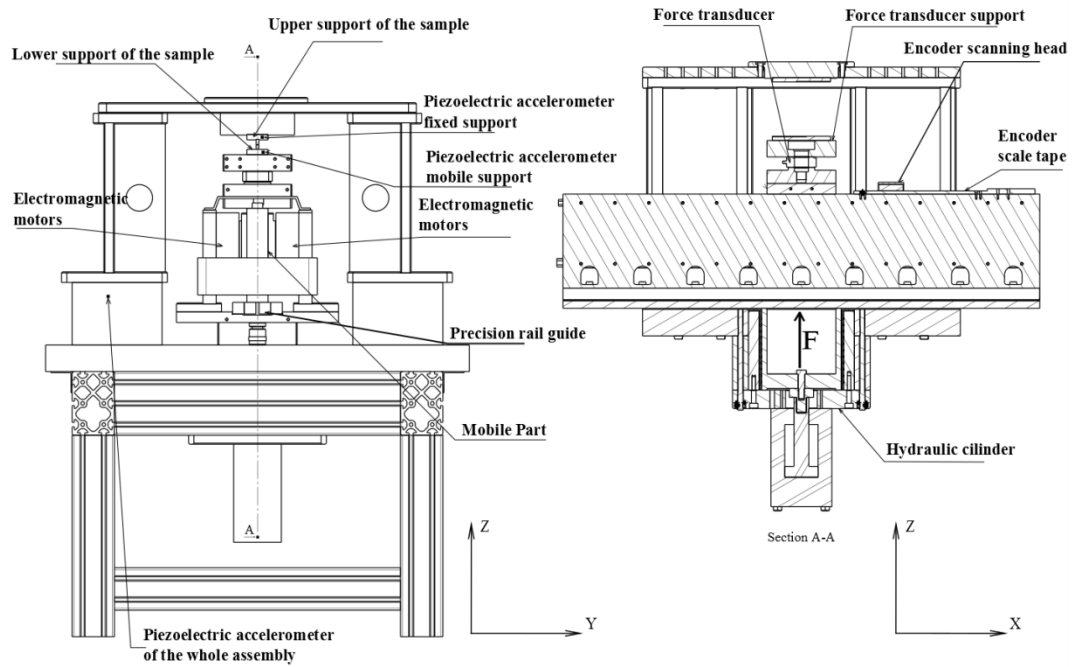


Figure 3-2: Lateral and frontal view of the experimental setup.

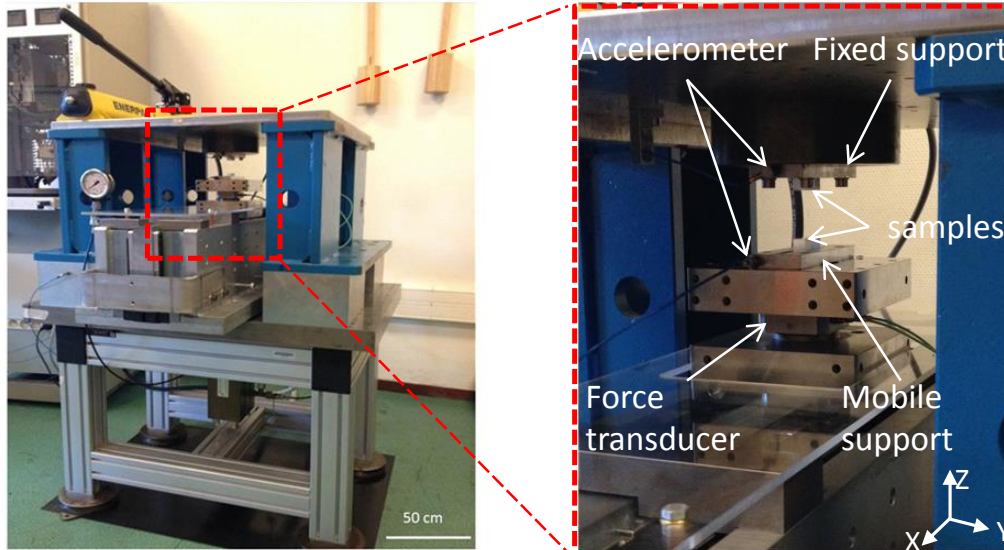


Figure 3-3: Photograph of the experimental setup and zoom related to the measurement zone.

In order to perform a dynamic and tribological analysis the newer setup has been designed with the aim of accessing to both the macroscopic dynamic

response of the system and as close as possible to the contact surface; the aim of the investigation being the understanding of the interaction between local contact behaviour and global dynamics. The following measurement instrumentation has been used to perform the experimental analysis presented in this thesis:

- A 3D force transducer allows for recording the macroscopic normal and tangential force time histories and, consequently, the global response of the frictional system;
- 1D component accelerometers (PCB of type 353B16, 353B15, 352C66) have been positioned in the direction of the relative motion (x direction) in order to analyse the structural and dynamics response (up to 10 kHz) at the main components of the setup: upper (fixed) sample support, lower (mobile) sample support and the external frame of the set-up (see Figure 3-2);
- A 3D component accelerometer (PCB of type 339A30) has been used to analyse the dynamics response of the mobile part of the setup in order to understand which modes are involved in the global response of the whole system (samples in contact and auxiliary parts of the setup);
- A laser vibrometer (POLYTECH) allowed for analyse the response at the contact samples, recording the vibration velocity (up to 1.5 MHz frequency range) at a single point in the x direction as close as possible to the contact surface. This kind of measure, very close to the contact zone and able to recorder the dynamic response on the contact samples, allowed to better distinguish between the components of the response due to either the assembly or the sample dynamics. Moreover, the measurement of the velocity of a point close to the contact allows for recording signals coming from the rupture propagation at the contact.

3.3.2 Stiffness and dynamic characterization

The interaction between the system structural dynamics and the local contact behaviour is of crucial importance to analyse the contact scenarios that can arise when deformable bodies are in relative motion. In order to better control the imposed boundary conditions, a particular attention during the design phase has been attributed to the tangential stiffness of the whole setup. The considered setup is characterized by a high rigidity in the x (tangential) direction in order to apply well controlled boundary conditions and avoiding that the setup stiffness controls the contact scenarios during the sliding motion. However, because the system components cannot be considered as rigid bodies, it is important to quantify the global stiffness and dynamics.

Tangential stiffness

In order to perform the subsequent numerical analysis, the experimental tangential stiffness has been estimated by means of preliminary experimental measurements.

Experimental tests have been performed by recording the tangential force as a function of the imposed displacement, for different values of the horizontal velocity and normal load. Figure 3-4 shows the used approach to estimate the global tangential stiffness in the case of horizontal velocity of 5 mm/s and normal contact load of 900 N. The tangential force and the contact normal force as a function of the imposed horizontal displacement are recorded. In Figure 3-4 the normal load phase is not reported. In order to calculate the global stiffness of the system the first tangential force ramp, corresponding to the preloading tangential phase, has been considered; in this phase the whole contact interface can be considered in sticking state. The slope of the tangential force in Figure 3-4, in the first linear phase, represents the global stiffness related to the tangential direction (x-direction).

Different tests with different driving velocity and normal loads have been considered to estimate a mean value of the equivalent (global) tangential stiffness. Considering the geometry of the system, the rigidity of the system in the x direction can be mainly dissociated by the contribution of two terms: one related to the tangential stiffness of the samples in contact; one related to the tangential stiffness of the force transducer and the mobile part of the setup. Looking at the configuration of the setup schematized in Figure 3-5, the tangential stiffness of the assembled system can be modelled by two equivalent spring in series, accounting for the two contributions mentioned above.

The global stiffness of the whole assembly (set-up and samples) is first calculated by the measured slope of the tangential force (Figure 3-4); then, the tangential stiffness related to the deformation of the samples in contact can be calculated numerically or analytically (assuming the hypothesis of adherence state between the two bodies); finally, knowing the global stiffness and the component due to the sample deformation, it was possible to calculate (equation highlighted in Figure 3-5) the contribution of the tangential stiffness of the set-up ($K_{\text{setup}}=1.7e7$ [N/m]), which is a characteristic of the considered tribometer.

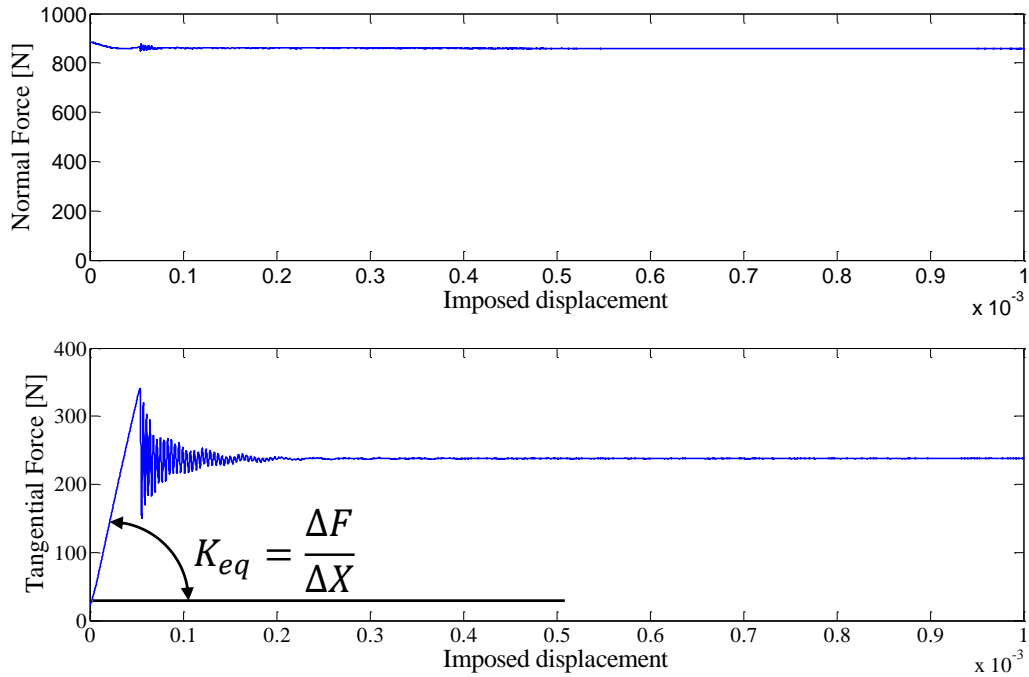


Figure 3-4: Estimation of equivalent (global) tangential stiffness K_{eq} for imposed driving velocity of 5 mm/s and contact normal load of 900 N (3 MPa).

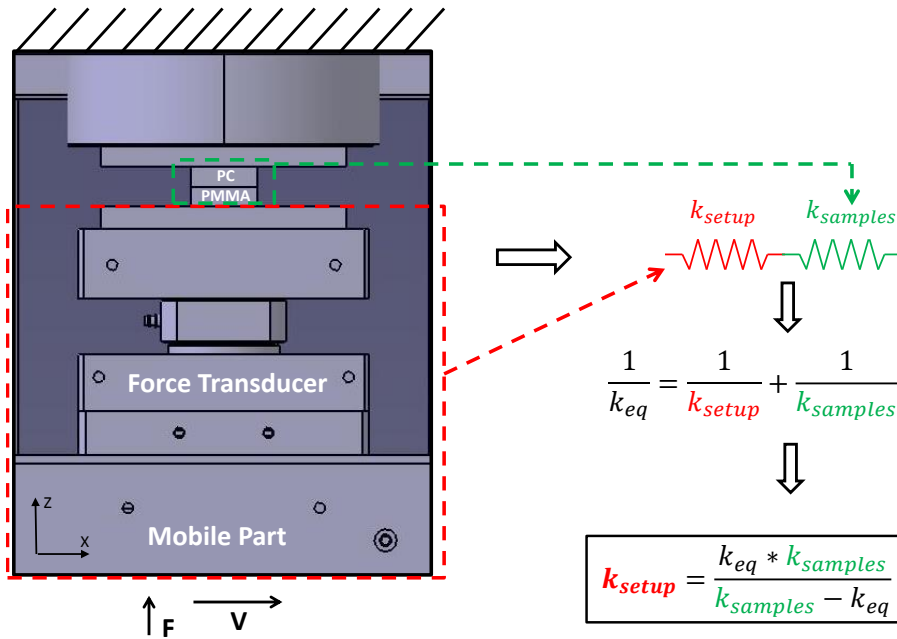


Figure 3-5: Configuration scheme used to evaluate the setup tangential stiffness k_{setup} .

Tangential dynamics

On the other hand experimental tests have been performed in order to investigate the tangential dynamics of the system. This analysis is needed to understand and account for the main frequencies involved in the experimental tangential response of the whole system, when excited by the frictional forces. In particular, the impulsive dynamic excitation due to the macro-slip event, when macroscopic stick-slip occurs (Tangential force drop in Figure 3-6(c)), allowed for highlighting the frequency components of the system response, due to the tangential system dynamics.

Figure 3-6 shows the frictional and dynamics response of the whole system for the following boundary conditions: normal contact force of 900 N (3 MPa) and horizontal driving velocity of 5 mm/s. Figure 3-6 shows the acquired signals after the preload phase, when the normal force has already reached its maximum value (Figure 3-6(b)) and stays almost constant during the test.

Once the bodies achieved the wished normal contact (Figure 3-6(b)), an imposed linear displacement (Figure 3-6(a)) is imposed to the mobile part and the response of the system is recorded by means of the accelerometers (Figure 3-6(d)(e)(f)) and the force transducer (Figure 3-6(b)(c)). Figure 3-6 (d)(e)(f) shows the accelerations related respectively to the lower (mobile) part, the upper (fixed) part and the external frame of the setup measured by means of the accelerometers positioned as shown in Figure 3-2.

The amplitude of the acceleration signals, after the initial sudden drop of the tangential force (macro-slip event), highlights as the response of the system is mainly governed by the dynamics of the lower (mobile) part.

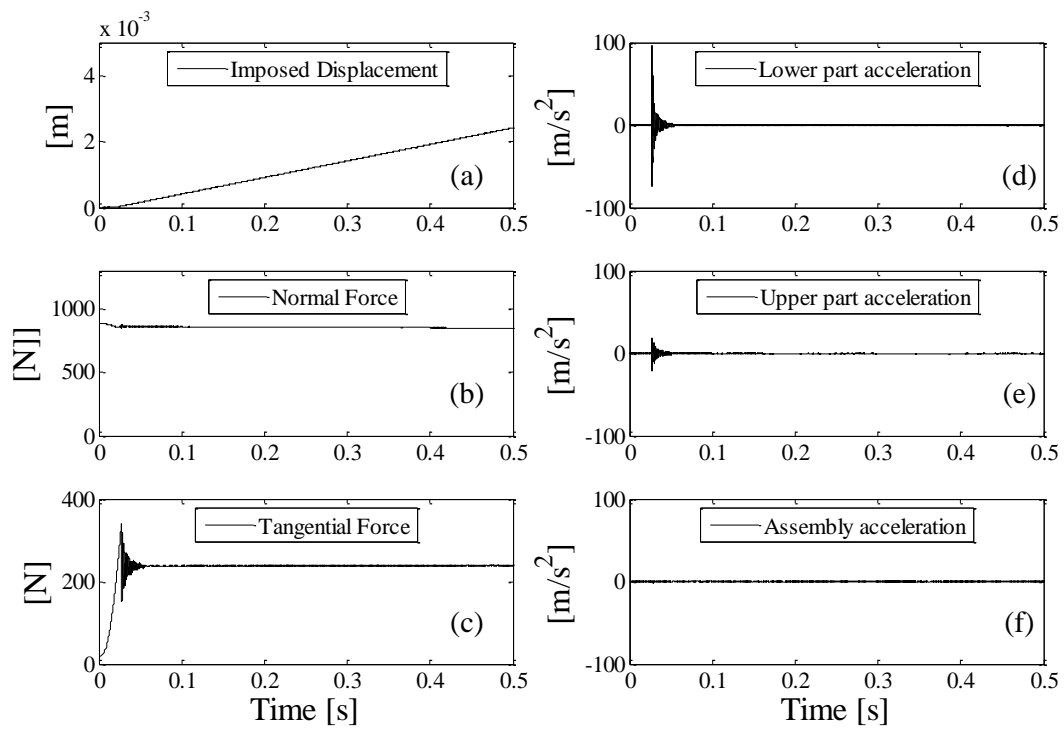


Figure 3-6: Recorded signals for an experimental test performed with an initial normal force of 900 N and imposed driving velocity of 5 mm/s, considering PMMA-PC samples. The recorded accelerations are related to the x (tangential) direction.

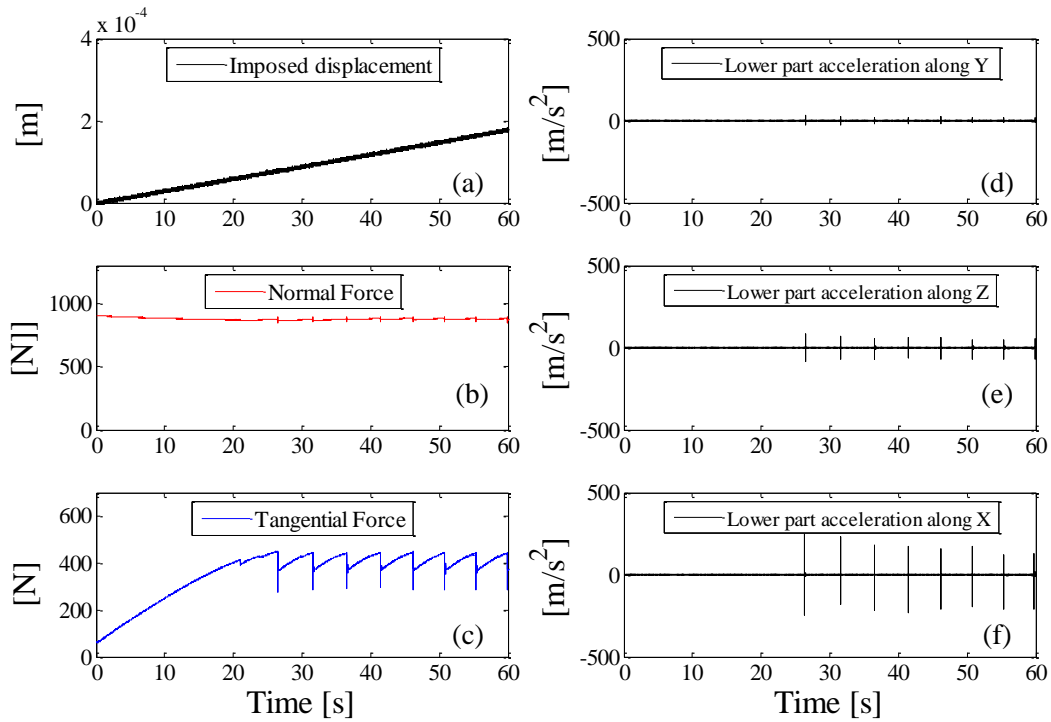


Figure 3-7: Recorded signals for an experimental test performed with an initial normal force of 900 N and imposed driving velocity of $5 \mu\text{m/s}$, considering PMMA-PC samples. The recorded accelerations are related to the lower (fixed) part of the setup.

To investigate the dynamic response of the mobile part a further experimental test has been performed with the following boundary conditions: horizontal driving velocity of $5 \mu\text{m/s}$ and normal contact force of 900 N, when macroscopic stick-slip behaviour is obtained. By means of a 3D piezoelectric accelerometer, fixed to the lower mobile part, the acceleration signals along the 3 directions have been recorded during each drop of the tangential force (macro-slip). Figure 3-7(a)(b)(c) shows respectively the imposed displacement, contact normal force and tangential force as a function of time. Figure 3-7(d)(e)(f) shows the lower part accelerations along the x, y and z direction. The results of the performed test highlighted as the dynamic response of the mobile part of the system during each tangential force drop is higher along the x direction.

The spectrum (FFT) of the lower part acceleration along x direction (Figure 3-8), after a force drop (impulsive excitation), showed that the main frequency associated to the tangential response of the system is at about 1200 Hz. This peak correspond to the natural frequency of the tangential mode of the mobile part of the whole assembly, which dominates the tangential response of the system.

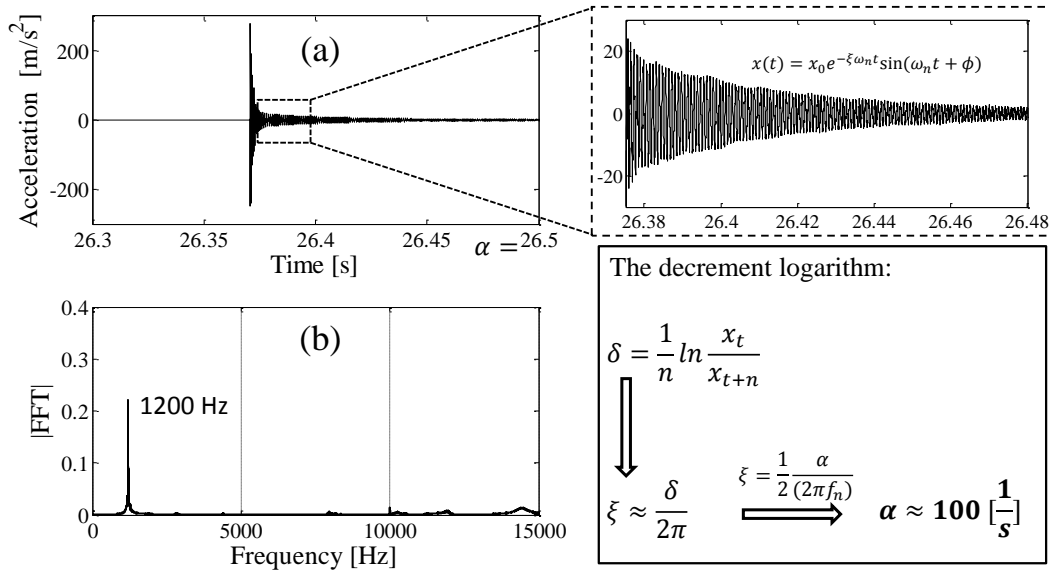


Figure 3-8: On the left: (a) Acceleration along x direction of lower part and (b) related spectrum of the signal acceleration for the following boundary conditions: imposed driving velocity of $5\mu m/s$ and normal contact force of $900 N$. On the right: Estimation of equivalent damping by means of decrement logarithm method.

The dynamic properties, such as the associated damping and the equivalent distributed mass, of the system mode have been also estimated in order to implement the tangential dynamics of the setup in the numerical model.

The damping factor associated to the tangential mode of the setup has been estimated by means of the decrement logarithmic method Figure 3-8.

On the other hand the equivalent mass has been derived considering the tangential stiffness of the setup and the mode frequency involved in the tangential response of the system (1200 Hz). Two assumptions has been used: first, the total mass of the two samples in contact is negligible with respect to the equivalent mass of the setup; second the two contact samples stay in adherence status after the macro-sliding (impulsive excitation). Considering that, the schematization used to calculate the equivalent mass (needed to implement the setup dynamics) is reported in Figure 3-9.

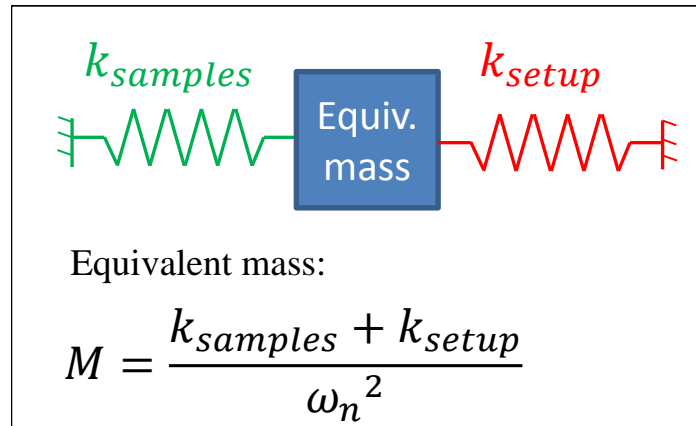


Figure 3-9: Equivalent scheme used to calculate the equivalent mass of the setup.

In such a way the tangential mode, characterizing the main contribution to the dynamic response of the system, has been introduced into the numerical model by means of its equivalent stiffness, mass and damping (see Chapter 6).

The identification of the mean tangential stiffness and the dynamics (mode frequency, mass and damping) of the setup are of main importance into simulating the dynamics response of the system (set-up and samples). A numerical model, which takes in account the dynamics of both the samples in contact and the whole experimental setup, allowed for realizing a quantitative comparison between experimental and numerical results shown in the chapter 6.

4 Frictional scenarios in dry contact: numerical analysis

4.1 Introduction

This chapter presents a numerical analysis of the frictional scenarios that can arise when two elastic media with a frictional interface are in relative motion.

The performed non-linear transient simulations highlight as the same mechanical system can switch from macroscopic stick-slip instability up to continuous sliding behaviour with or without harmonic vibrations (mode coupling instability) as a function of system key parameters.

The macroscopic stick-slip behaviour is characterized by sudden friction force drops (sliding state) along the time, separated by periods of elastic energy accumulation (stick state).

Instead, the mode coupling instability occurs when a vibration mode of the mechanical system becomes unstable due to the frictional contact forces, leading to harmonic vibrations. This kind of instability, generated by frictional forces, has been mainly object of works dealing with a specific issue named brake squeal and related to brake systems. However this chapter shows how any mechanical system can generate harmonic acoustic emission comparable to brake squeal noise during relative motion with frictional contact.

The nonlinear transient simulations and complex eigenvalues analyses allowed for investigating the different instability scenarios and drawing qualitative maps as a function of driving parameters. In this chapter the effect of the Rayleigh damping coefficients is focused and the role of the material damping on the frictional dynamics has been investigated. The results show the need on implementing a good estimation of the material damping when modelling systems with frictional contact, in order to have reliable simulations.

4.2 Description of the model

The 2D model (plane strain deformation) consists of two isotropic elastic finite media separated by a frictional interface (see Figure 2-1) governed by a classical Coulomb friction law, described in the section 2.2.3. The material and geometrical properties of the finite element model are listed in Table 1. The two bodies are put in contact with a compressive normal force $F=10\text{ N/mm}$; after the

stabilization of the first normal phase, a constant horizontal velocity $V=10 \text{ mm/s}$ is applied at the lower body (slider) to bring the system in sliding state, while the upper body is maintained fixed.

Nodal displacements, velocities and accelerations of the system nodes, as well as the values of the contact forces and contact node status (stick, slip and detachment) are calculated along the simulation time.

	Body 1	Body 2
Length L [mm]	10	10
Width W [mm]	3	3
Element number	48000	9048
Contact element size [mm]	0.025	0.0575
Young Modulus E [GPa]	2.5	3.9
Density ρ [Kg/m³]	1202	1303
Poisson ratio ν	0.38	0.33
Damping parameter α [1/s]	40	40
Compressive force F [N/mm]	10	10
Initial averaged normal stress $\sigma=F/L$ [MPa]	1	
Horizontal velocity V [mm/s]	10	
Coulomb friction coefficient μ	1	
Integration time step [s]	0.334e-8	

Table 1: Geometry dimensions, material and mesh properties used to perform the non-linear simulations.

This section presents different macroscopic frictional behaviours during the relative motion between the bodies in contact, when the damping parameters are modified.

The material damping is introduced in the model as proportional damping model and the global damping matrix has the following expression:

$$\mathbf{C} = \alpha[\mathbf{M}] + \beta[\mathbf{K}] \quad (10)$$

Where α is the mass matrix coefficient and β is the stiffness matrix coefficient.

The α coefficient affects, mainly, the low frequency vibrations, while β affects the high frequency vibrations of the system. Numerical transient simulations have been performed changing both the damping parameters. The first part of the chapter deals with the results obtained varying the stiffness damping parameter, which affects directly the local dynamics at the contact

[17], i.e. the wave generation and propagation at the frictional interface and, consequently, its coupling with the system dynamics [12, 20, 64]. Further simulations, as a function of the mass damping parameter, have been then performed and the main results have been presented in the last section of the chapter.

4.3 Macroscopic stick-slip instability ($\beta = 5e-10$ s)

Figure 4-1 shows the results obtained by the transient non-linear contact simulations when the stiffness damping coefficient β is fixed to $5e-10$ s, while the mass damping coefficient α , measured experimentally [87] on polycarbonate, is fixed to 40 s⁻¹.

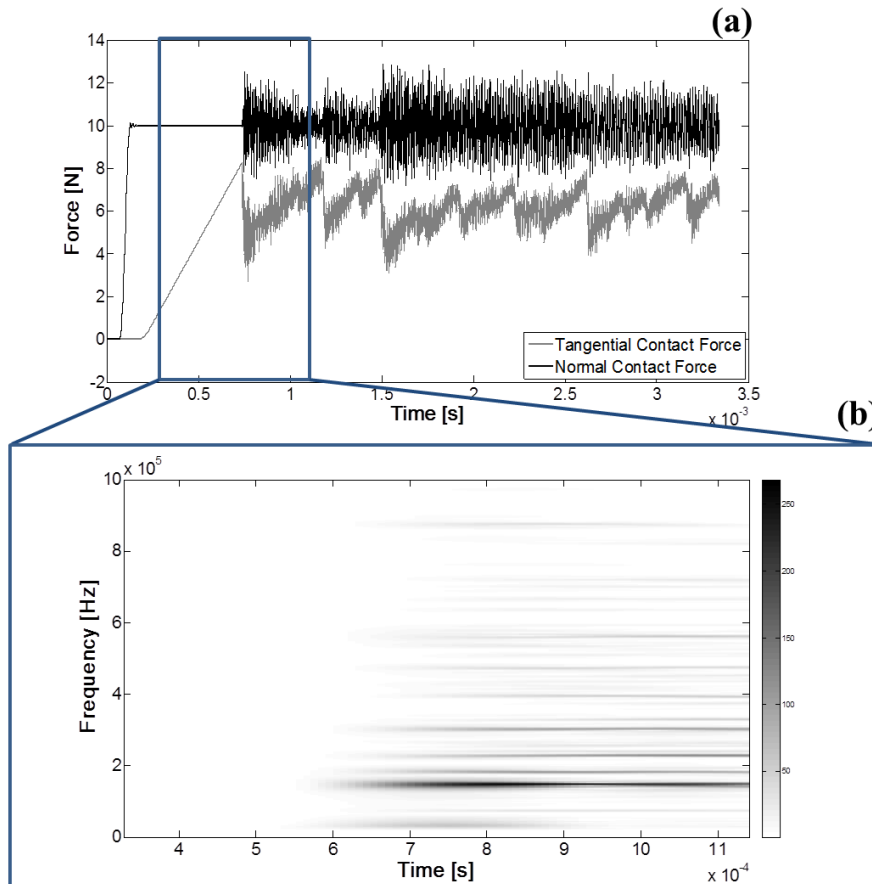


Figure 4-1: (a) Time evolution of the global (tangential and normal) contact force with $\beta = 5e - 10$ s and $\alpha = 40$ s⁻¹. (b) Time-varying spectral representation of the tangential contact force for $t \in [3e - 4 \div 1.1e - 3]$ s.

Figure 4-1(a) shows the time evolution of the sum of the tangential and normal contact forces (approximately x and y direction, because the contact interface can be considered flat). After a first normal and tangential preloading phase, the system behaviour is dominated by macro stick-slip phenomena, characterized by sudden drops of tangential force along the simulation time (Figure 4-1(a)). The tangential contact force exhibits repetitive fluctuations due to the macro-slip events at the contact interface. This effect is due to the energy that is stored by the solid deformation during the force ramps, and that is then released during the force drops, due to the ruptures propagating at the interface that switch suddenly the most of the interface in the sliding state, as shown in [17, 88].

Each force drop, with the consequent energy release, excites the structural dynamics and generate system vibrations. Figure 4-1(b) shows the natural frequencies of the system that are excited by the contact forces, while Figure 4-2 shows the velocity distribution of the system, along x direction, at time $t = 7.668e-4$ s, highlighting different velocity oscillations in the system during the stick phase subsequent to the macro slip event (excitation).

After a first stable tangential preload phase with a linear increasing of the tangential force, for $t = 7e-4$ s the macro-slip starts and the first natural frequencies of the system are excited. The first modes (natural frequencies) of the system can be detected from the time-varying spectrum of the system response in Figure 4-1(b) for $t \in [3e-4 \div 1.1e-3]$ s. The frictional excitation (macro-slip) can be considered as a quasi-impulsive excitation due to the sudden release of the stored elastic energy by means of the rupture propagations at the contact interface.

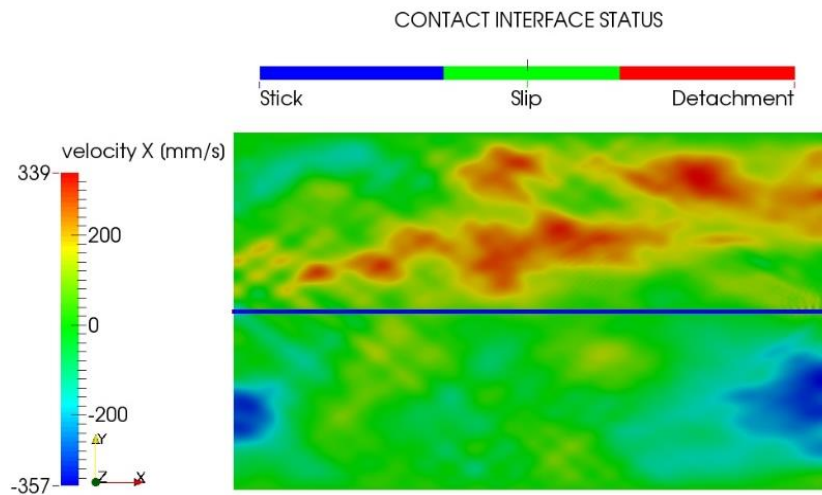


Figure 4-2: (a) Velocity along x direction and status of the contact interface at time $t = 7.668e-4$ s for $\beta = 5e - 10$ s and $\alpha = 40$ s $^{-1}$.

A detailed analysis concerning the rupture propagation during stick-slip instability and the interactions between the contact dynamics (wave and ruptures generation and propagation at the contact) and the macroscopic frictional behaviour is presented in [17, 88].

Figure 4-3 shows the time evolution of the contact forces when the value of the stiffness matrix damping coefficient is ranged between $5e-10$ s up to $1e-8$ s; the figure highlights as the macroscopic behaviour of the system changes with respect to the increase of the β damping parameter. The tangential contact force shows a reduction of the amplitude of the force drops due to the macro-slip events, while the period of the force fluctuation decreases. For larger values of the stiffness damping coefficient ($\beta = 1e-8$ s) the force fluctuations disappear and the global tangential force reaches the limit value determined by the local friction law imposed to the contact nodes. In fact, for a large damping factor, the interface waves decay faster after their nucleation and the energy is dissipated progressively by the material damping [17]. In this condition, the stick-slip force drops disappear and the system reaches a “continuous sliding” status along the whole contact surface. For this reason, the macroscopic friction coefficient coincide with the local one, imposed by the friction law.

While the force drops disappear, a high frequency vibration of the system can be recognized by the oscillations of the contact forces (Figure 4-3(f)); this behaviour, due to mode coupling instability, is analysed in detail in the following sections.

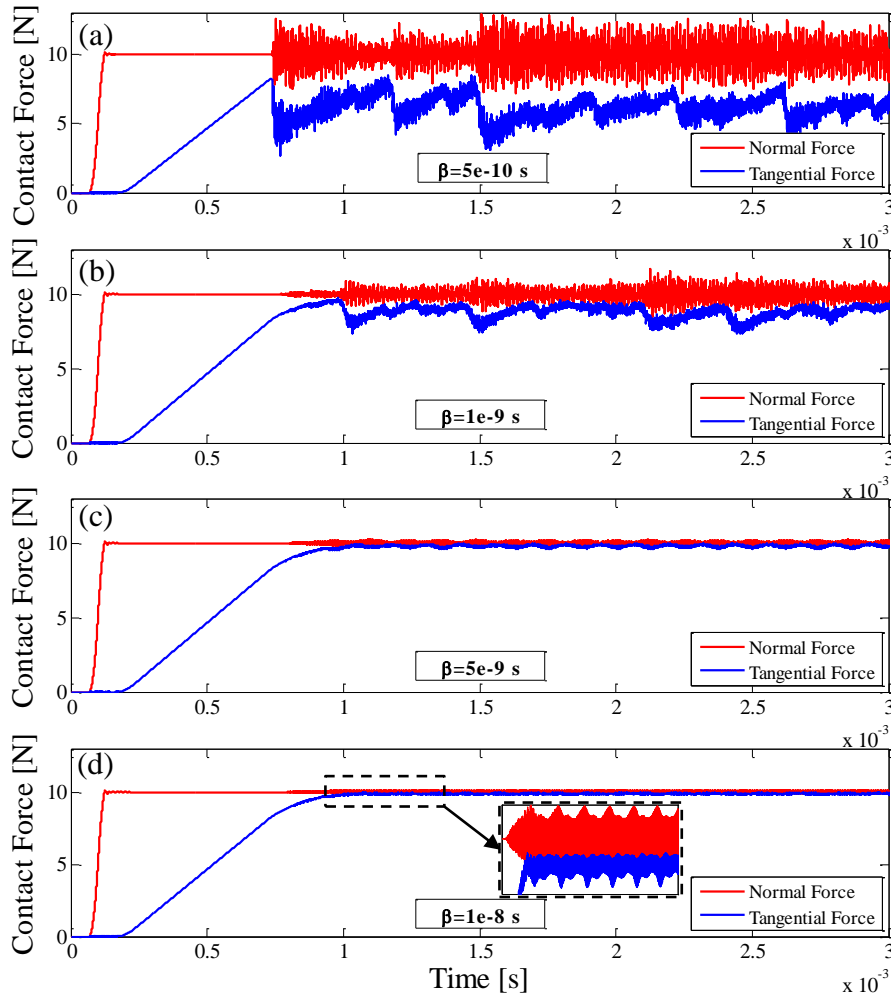


Figure 4-3 Time evolution of the global contact force for different values of stiffness damping coefficient β . Mass damping coefficient α is fixed to 40 s^{-1} .

4.3.1 Effect of mass damping parameter α

The effect of the α damping parameter, when the frictional response of the system is dominated by macro stick slip behaviour, is here investigated. While the stiffness damping coefficient β has been set to $5\text{e-}10 \text{ s}^{-1}$, the mass damping parameter has been varied. Figure 4-4 shows the global frictional response (tangential and normal contact force) while the mass damping parameter has been varied from 40 to 40000 s^{-1} . The macroscopic behaviour of the system doesn't change and the system is always characterized by macroscopic stick-slip phenomena. By the way, the numerical results highlighted how the mass damping parameter affects the response of the system after each macro slip excitation. In fact, while the β damping parameter drives the macroscopic stick-slip behaviour thanks to its effect on the rupture and wave propagations, the

increasing of the α damping parameter damps the oscillations of the system response during each ramp (stick) phase, as shown in Figure 4-4(c).

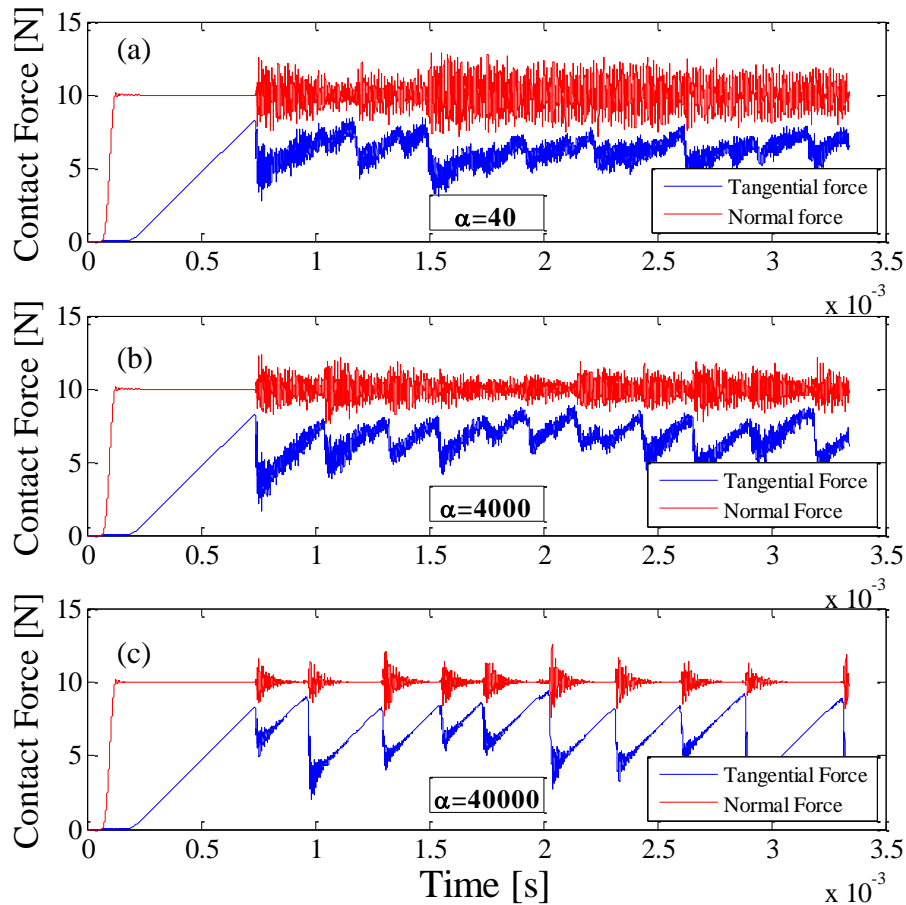


Figure 4-4: Time evolution of the global contact force for different values of mass damping coefficient α . Stiffness damping coefficient β is fixed to $5e-10$ s.

4.4 Continuous sliding with mode coupling instability

This section discusses the system behaviour when the system parameters are set to obtain continuous sliding between the bodies in relative motion. In these conditions, increasing the stiffness material damping parameter, the system switch between another unstable behaviour, characterized by mode coupling instabilities with harmonic vibrations, and stable behaviour without any relevant system vibration. When affected by mode coupling instability, the system can switch between different unstable modes at different frequencies, as a function of the imposed material damping.

4.4.1 High frequency instability ($\beta = 1e-8 s$)

Figure 4-3(d) shows the time evolution of the global contact forces for $\beta = 1e-8 s$, and the magnification of the oscillations occurring when the tangential force reaches the limit value; an increase of the vibration amplitude can be observed up to a limit cycle ($t > 1.1e-3s$) that is characteristic of self-excited vibrations [79, 80]. To analyse in detail the dynamic behaviour of the system during the relative motion, Figure 4-5 (c) shows the acceleration calculated at one node of the upper body, for the time interval from $0.7e-3 s$ to $2.6 e-3 s$. Two consecutive phases are highlighted: in the first phase, the oscillation amplitude of the acceleration increases exponentially as could be expected by a response of an unstable linear system; in the second phase, the oscillations stabilize at a limit cycle and a maximum of the amplitude, due to the contact nonlinearities [89], is reached. This behaviour is characteristic of mode coupling instabilities (squeal in brake systems, squeaking in hip endoprosthesis).

The FFT (Fast Fourier Transform) of the acceleration signal, calculated in the first phase (Figure 4-5(a)), shows a harmonic spectrum with only a fundamental harmonic at about 406 kHz. On the other hand, the FFT of the acceleration signal, calculated in the second phase (Figure 4-5(b)), shows both a main frequency peak, representing the fundamental harmonic at 406 kHz, and the respective sub-harmonics and super-harmonics of the signal, due to the contact non-linearities. The high frequency of the vibration is due to the reduced dimensions of the model (Table 1), which bring to relative high frequencies (the first mode is at 65 kHz), and are due to the fine mesh needed to have convergence with a reasonable computational effort.

A linear CEA (Complex Eigenvalues Analysis) has been developed with the same system parameters used to perform the transient simulation. The stability analysis of the system under steady sliding has been carried out. The eigenvalues calculated by the CEA analysis predict an unstable mode (positive real part of the eigenvalue) at 402 kHz.

The natural frequency of the unstable mode calculated by the CEA matches with the main harmonic of the system vibrations, calculated by the transient non-linear analysis. The real part of the unstable eigenvalue has been used in order to plot the exponential growth of the system vibrations expected by the linear analysis (bleu curves in Figure 4-5(c)); the figure shows how the plotted curve matches the growth of the vibrations calculated in the first phase of the transient simulation (Figure 4-5(c)). Thus, during the first phase (Figure 4-5(c)) the system behaviour corresponds to a modal dynamic instability of the linear system under sliding state. In the second phase, the non-linearities at the contact limit the system oscillations and stabilize the system response that reaches a limit amplitude (limit cycle) of vibration (Figure 4-5(c)). During this phase the

system response shows sub and super-harmonics of relative large amplitude and the phase plane (reported in Figure 4-5(d)) suggests the possible appearance of a chaotic behaviour [90].

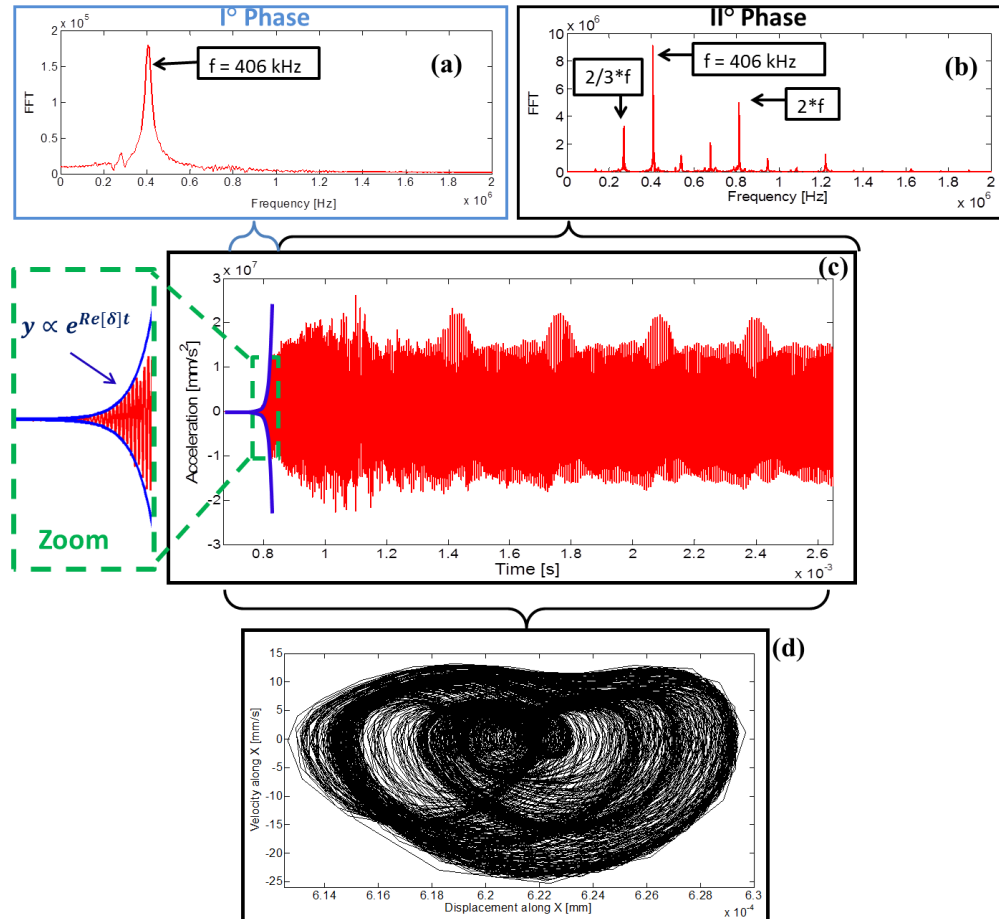


Figure 4-5: (a) FFT of the acceleration signal in the first (linear) phase. (b) FFT of the acceleration signal in the second (nonlinear) phase. (c) Node acceleration along y calculated by the non-linear transient analysis for $\beta = 1e-8$ s. The blue curve refers to the exponential vibration growth expected by the linear CEA. (d) Phase space (displacement-velocity) for a node of the fixed body.

A further comparison between the results from the linear analysis and the nonlinear one can be done by the comparison of the modal deformed shape of the unstable mode calculated by CEA and the vibrational deformation of the system calculated by the transient analysis. Figure 4-6(a) shows the velocity of the system along the Y direction at time $t = 0.8e-3$ s, computed by the transient simulation; Figure 4-6-b shows directional deformation along Y , calculated by the CEA. The calculated deformed shapes match each other, confirming that the calculated unstable mode is effectively the one excited during the transient

simulation. The slight difference between the two deformed shapes and the calculated frequency is due the fact that the stability analysis is performed with a linear approximation at the sliding steady state, while the transient analysis account for the actual contact conditions (stick, slip, detachment), as described below.

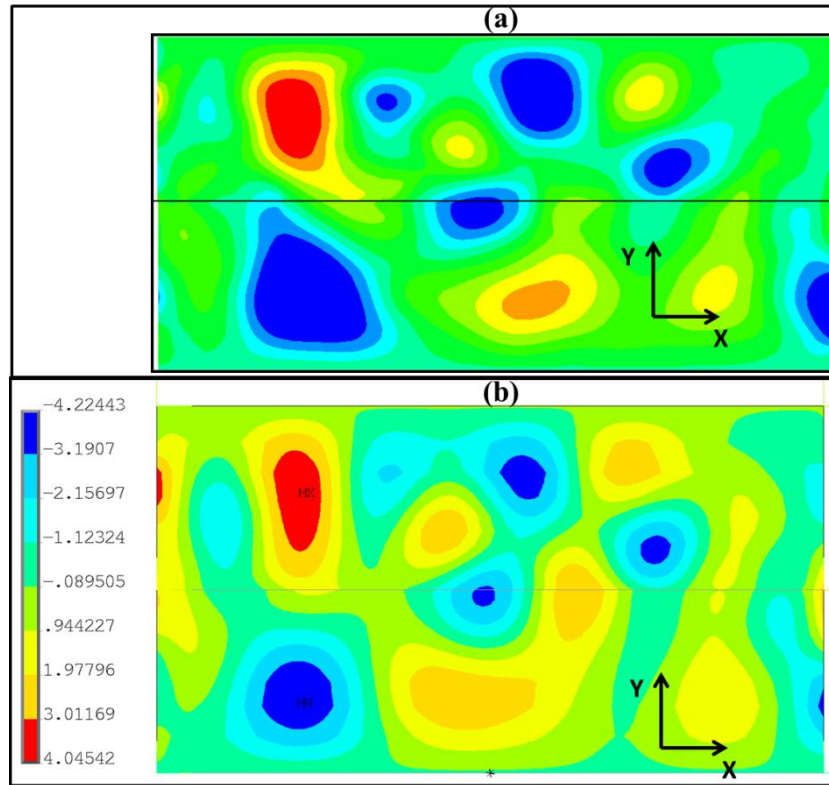


Figure 4-6: (a) Velocity of the system along Y at time ($t=0.3 \text{ e-}3 \text{ s}$) with $\beta = 1 \text{ e-}8 \text{ s}$ (PLASTD). (b) Directional deformation (real part) along Y of the mode at 402 kHz (CEA).

4.4.2 Low frequency instability ($\beta = 1 \text{ e-}7 \text{ s}$)

Figure 4-7 shows the results obtained from non-linear simulations when a higher value of the stiffness damping coefficient, $\beta=1 \text{ e-}7 \text{ s}$, is imposed. The behaviour of the system, after a first tangential preload phase, is still characterized by a “macroscopic continuous sliding” with harmonic vibrations; nevertheless the frequency of vibration is lower. The spectrum of the normal contact force shows a main harmonic at about 63 kHz (Figure 4-7 (b)); the respective super-harmonics, which are a characteristic of the non-linear contact behaviour once the limit cycle is reached, are of lower amplitude with respect to the ones presented in the previous section. Figure 4-7 (c) shows the limit cycle

of vibration on the phase space calculated for a node belonging to the upper body, where the limit cycle is distinguished clearly.

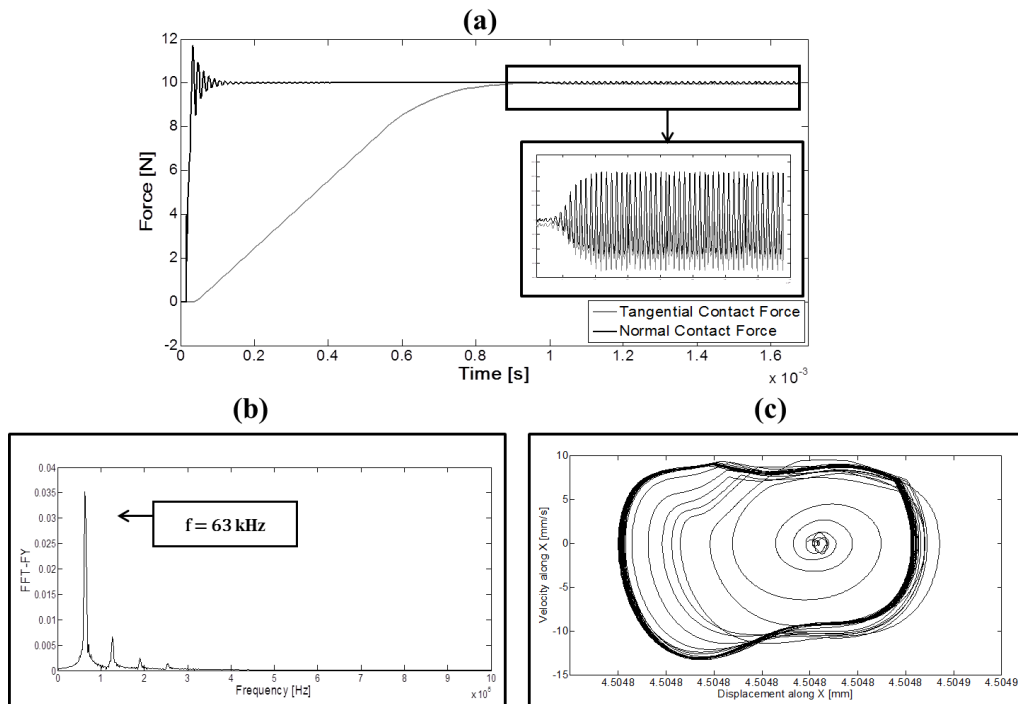


Figure 4-7: (a) Time evolution of the global contact force and a magnification of the signal with dynamic instability at 63 kHz. Stiffness matrix damping coefficient $\beta = 1e-7$ s, mass matrix damping coefficient $\alpha = 40$ s⁻¹. (b) Spectrum of the normal contact force signal. (c) Phase space (displacement-velocity) for a node of the fixed body. Integration time step $dt=0.6e-9$ s.

The CEA of the system has been performed with the same material damping used in the transient simulation. The eigenvalue extraction predicts an unstable mode at about 65 kHz. Figure 4-8(a) shows the velocity distribution of the system calculated by the transient simulation, while Figure 4-8(b) represents the directional modal deformed shape calculated by the CEA at 65 kHz. The agreement of the transient deformation and vibrational frequency, with the unstable eigenvector and eigenvalue calculated by the CEA analysis, allows for asserting that the system is still under self-excited vibrations due to a mode coupling instability [42, 77]. The increasing of the proportional (with respect to frequency) component of the material damping allowed for stabilizing the modes at higher frequencies and exciting an unstable mode at lower frequencies. Again, after a first phase characterized by an exponential growth of the system vibrations, the oscillation stabilizes up to a limit cycle (Figure 4-8(c)) due to the contact non-linearities.

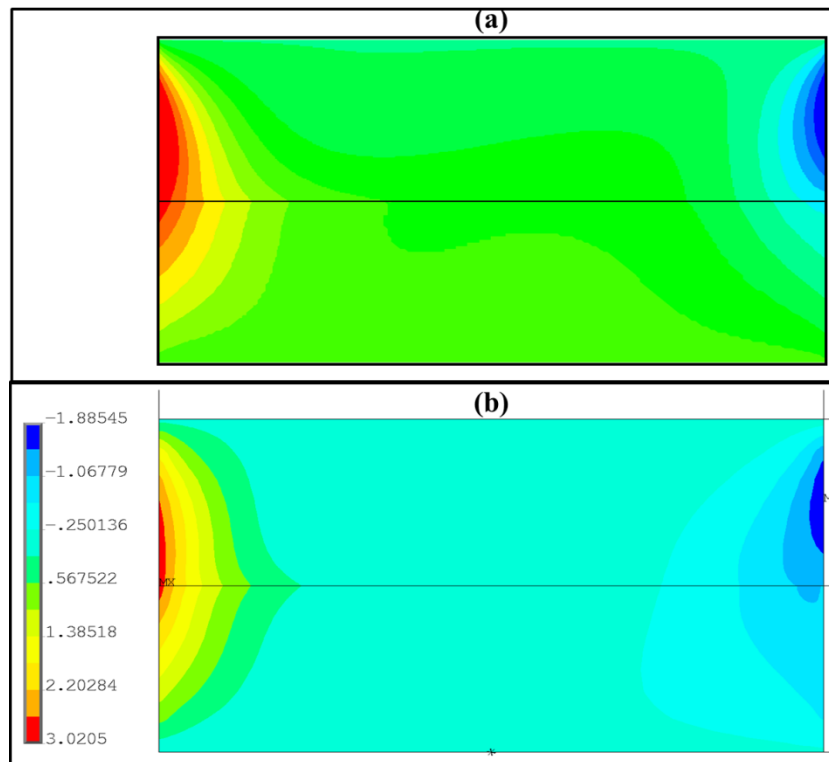


Figure 4-8: (a) Directional modal deformation (real part) along Y of the mode at 65 kHz (CEA). (b) Velocity of the system at time ($t=0.001031$ s) with $\beta = 1e-7$ s (PLASTD).

4.4.3 Effect of mass damping parameter α on limit cycle oscillations

The effect of the α damping parameter when the frictional response of the system is dominated by mode coupling behaviour is here investigated. With the stiffness damping coefficient β set to $1e-8$ s⁻¹, the mass damping parameter has been varied.

Figure 4-9 shows the acceleration along the y direction calculated at one node of the upper body, for the time interval from $0.7e-3$ s to $1.5 e-3$ s. The mass damping parameter has been varied from 40 to 93000 s⁻¹. The macroscopic behaviour of the system doesn't change and the system is always characterized by mode coupling instability. Nevertheless, the numerical results highlighted how the mass damping parameter affects the vibration amplitude and the exponential growth of the oscillations during the linear phase. In fact, when increasing the value of the mass damping parameter, the limit cycle of vibration is reached more slowly and its amplitude decreases.

Of course, a further increase of the α damping parameter, combined with a larger value of the β damping parameter, can bring to stable eigenvalues of the system and will result in a stable continuous sliding (see section 4.6).

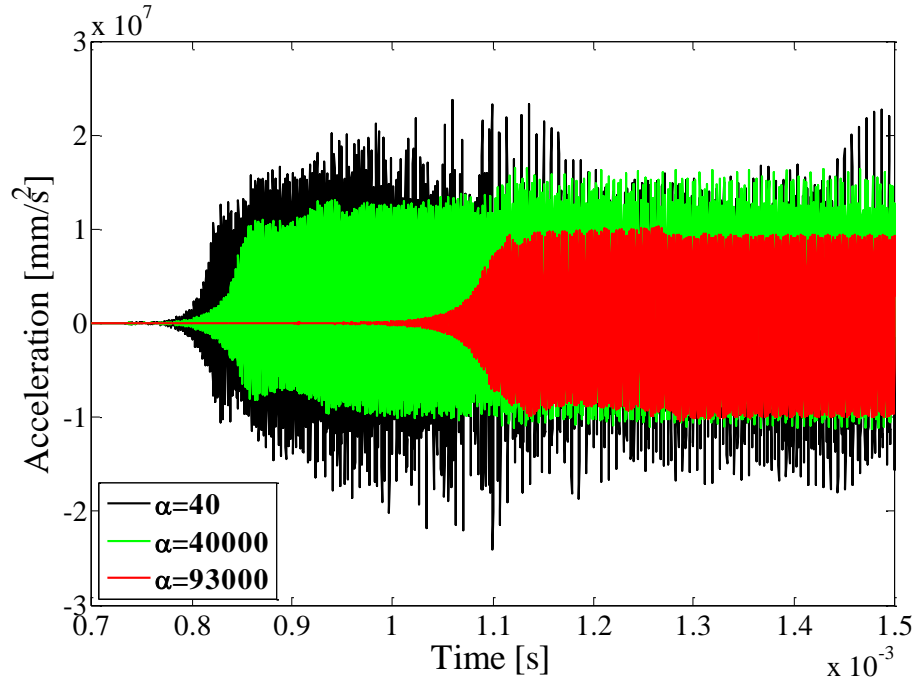


Figure 4-9: Time evolution of the acceleration along y direction for three different values of mass damping coefficient α . Stiffness damping coefficient β is fixed to $1e-8$ s.

4.5 Stable continuous sliding ($\beta = 1e-6$ s)

Increasing the damping parameter until $\beta=1e-6$ s the macroscopic behaviour, during the relative motion, is stable. In fact, as can be noted in the Figure 4-10, the global tangential force reaches the limit value defined by the friction law and not significant oscillations of the force (vibrations of the system) are recognized. In fact the system behaviour during relative motion is not characterized by instability phenomena (macroscopic stick-slip or mode coupling) and all the contact nodes stay in sliding state along the time (see Figure 4-11).

Even if in these conditions no “unstable” vibrations characterize the system response, it should be noticed that low amplitude vibrations are still present and are due to the response (stable response) of the system to the excitation at the contact. Nevertheless, when the system is stable, the excitation and response spectra are affected by the surface roughness that is not accounted for in this model. Specific analyses are devoted to this specific issue [84, 91].

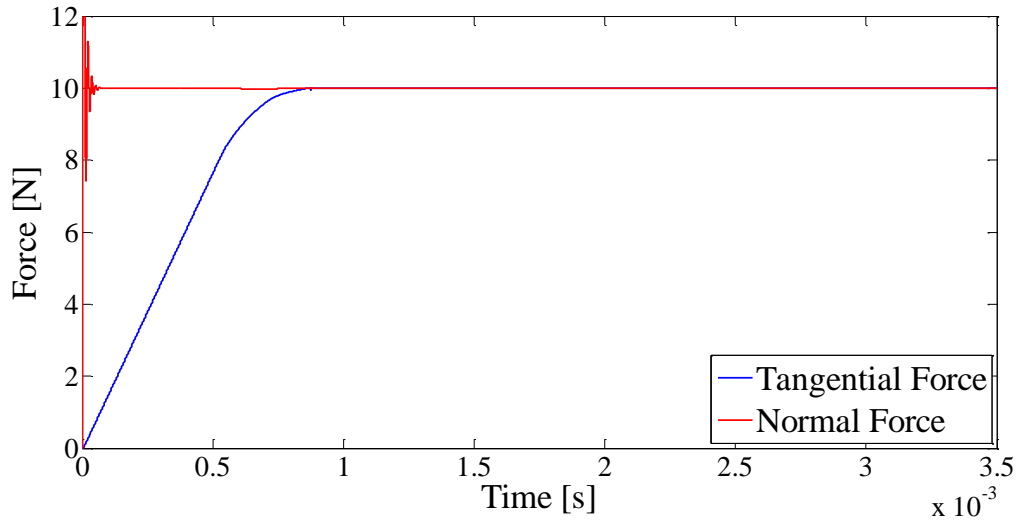


Figure 4-10: Time evolution of the global contact force. Stiffness matrix damping coefficient $\beta = 1e-6$ s, mass matrix damping coefficient $\alpha = 40$ s⁻¹ and integration time step $dt = 0.1e-9$ s.

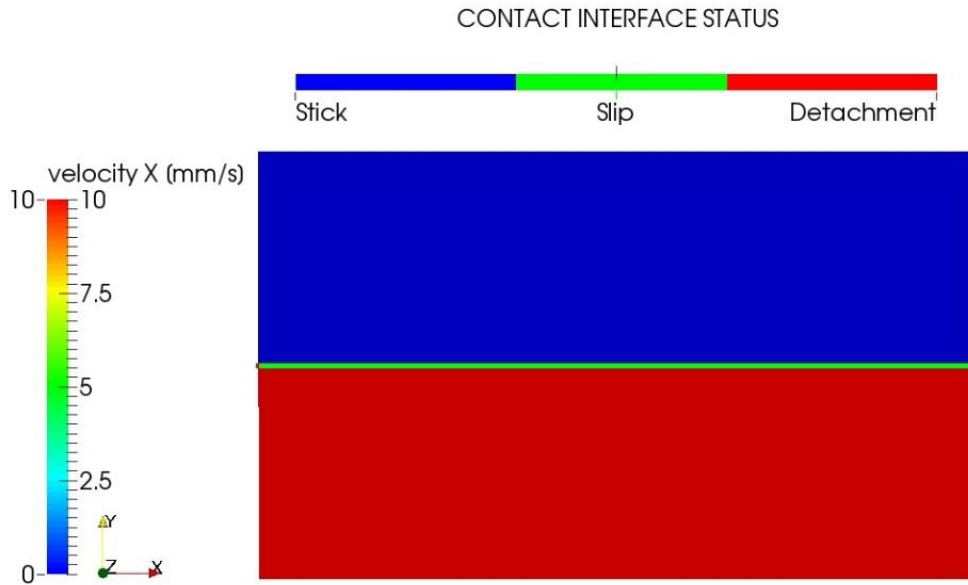


Figure 4-11: Time evolution of the global contact. Stiffness matrix damping coefficient $\beta = 1e-6$ s, mass matrix damping coefficient $\alpha = 40$ s⁻¹ and integration time step $dt = 0.1e-9$ s.

4.6 Parametrical complex eigenvalue analysis (CEA)

In this section a full parametrical pre-stressed linear CEA is presented to investigate the role of the damping in the dynamic stability of the system, calculated in steady state sliding condition. The influence of damping on the mode coupling instability of the modes at 402 kHz and 65 kHz is presented.

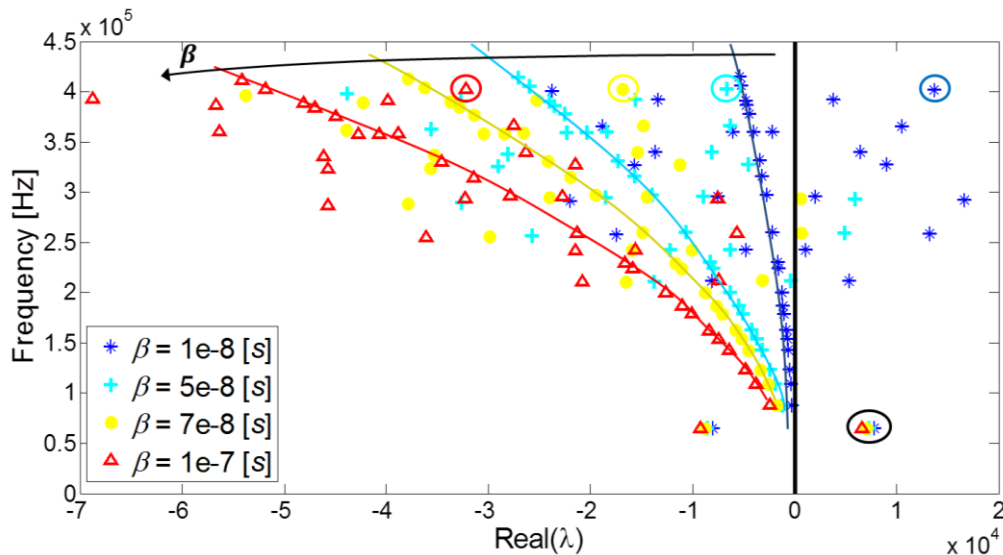


Figure 4-12: Locus plot in the frequency range 0-450 kHz for 4 different values of β . The continue lines represent the values of the real parts due exclusively to the material damping. The points, that split in opposite direction from continue line, identify the coupled eigenvalue real parts, which value is due to the global contribute of the material damping with friction conditions. The eigenvalue at 402 kHz, for the different values, has been highlighted by circles. The first (in frequency) unstable eigenvalue of the system at 65 kHz stays unstable ($\text{Re}[\lambda] > 0$) for all damping values.

Figure 4-12 shows the plot of the eigenvalues calculated in the frequency range between 0 kHz and 450 kHz, for four different values of the damping coefficient β , ranging between $1e-8$ s and $1e-7$ s. For each value of β it is possible to identify the contribution to the eigenvalue real parts due to the structural damping without friction contribution (continuous lines). When the lock-in between two modes occurs their real parts split from the structural damping value in opposite directions; one of the two modes can become unstable if its real part becomes positive. In general the Figure 4-12 shows how the increasing of β shifts all the eigenvalue real parts versus the negative half plane. Nevertheless, being the contribution of β to the modal damping

proportional with the frequency, the shift of the eigenvalues versus the negative half plane increases with the increasing of the imaginary part (frequency).

When β is equal to $1e-7$ s, all the modes, except for the 65 kHz eigenvalue (black circle in Figure 4-12), stay stable. This result explains why the transient analysis with β equal to $1e-7$ s presents a different frequency of the harmonic vibrations, corresponding to the sole mode (at lower frequency) that stays unstable.

When β is equal to $1e-8$ s several modes are calculated to be unstable by the real part of the eigenvalues, while the transient nonlinear analysis shows how only the mode at 402 kHz is at the origin of the unstable vibrations. The instability over-prediction of the CEA is a known issue [9, 78], and newer approaches accounting for the energy balance [30] during unstable vibrations are under investigation to propose more effective instability indexes [92, 93].

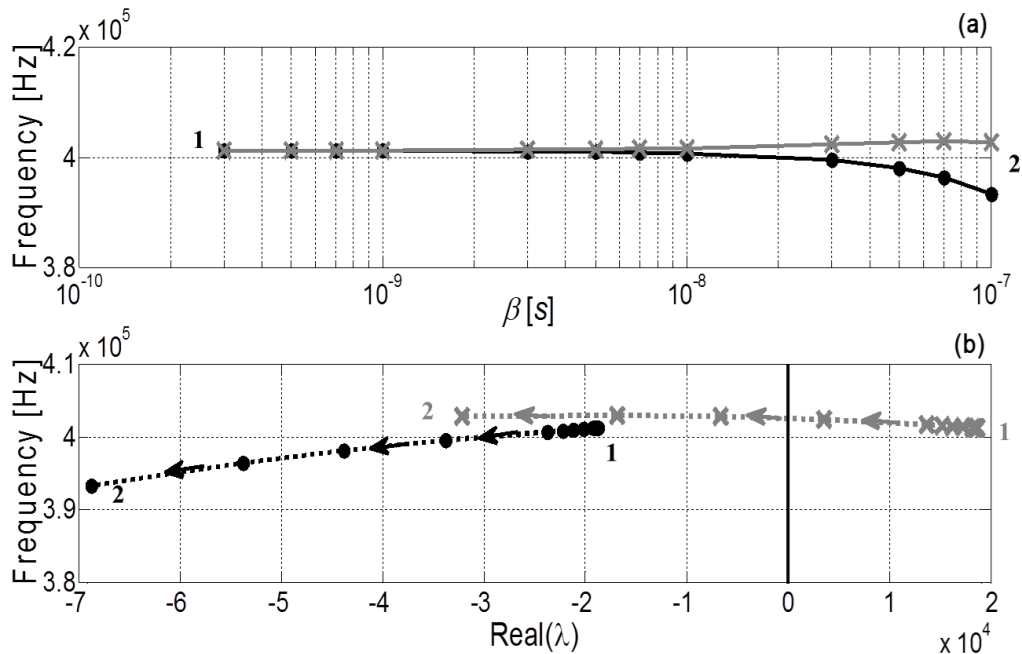


Figure 4-13: (a) Locus plot of the eigenvalues frequency around 402 kHz as a function of β . (b) Locus plot of the real part of eigenvalues around 402 kHz.

Focusing the attention to the mode at the 402 kHz, the representation of the eigenvalue imaginary parts (natural frequencies), obtained from the CEA as a function of β varying from $3e-10$ s to $1e-7$ s, is presented in Figure 4-13(a). The two coalescing modes, which are at almost the same frequency (lock-in unstable condition), split to two different frequencies (lock-out stable condition) with the increasing of β .

The locus plot reported in Figure 4-13(b) shows how the increase of β causes a decrease of the positive eigenvalue real parts; for $\beta < 5e-8$ s one of the coupling modes has positive real part, i.e. it is unstable; for $\beta > 5e-8$ s the real

part of both eigenvalues assumes negative value and both the modes are stable. As predicted by the transient simulations, the mode at 402 kHz results to be unstable for lower values of β .

On the other hand the Figure 4-14 shows the locus plot of the CEA for the two coupling modes at 65 kHz as a function of β (varying from $1e-7$ s to $1e-6$ s). Like in the mode lock-in at higher frequency, the two coupled modes split to two different frequencies when increasing β (Figure 4-14(a)). In particular, looking at the Figure 4-14(b), for $\beta < 8e-7$ s both the real parts of the coupled modes assume a negative value; therefore, also the lower mode results to be stable, as recovered by the stable response (stable continuous sliding) of the nonlinear transient simulation. The non-linear and linear analyses explain why for high value of damping parameter ($\beta < 1e-6$ s), the global behaviour is characterized by a stable state with no relevant oscillations during continuous sliding.

These results are in agreement with the mode coupling (lock-in) theory proposed by North [8] and investigated by several authors [7, 71, 72, 75] for the brake squeal noise emission.

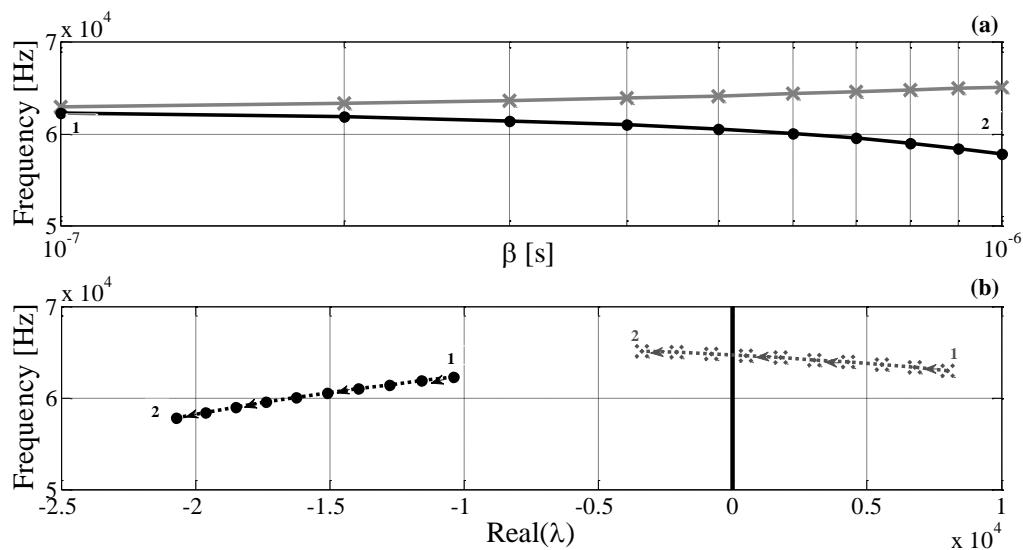


Figure 4-14: (a) Locus plot of the eigenvalues frequency around 65 kHz as a function of β . (b) Locus plot of the real part of eigenvalues around 65 kHz.

4.7 Coupling between local contact behaviour and system dynamic response

This section focuses the attention to the interaction between the local contact behaviour and the system response during the different contact scenarios

described in the previous sections. Because of the difficulties in measuring and correlating the local contact behaviour (rupture and wave propagation, contact status distribution and transition, ...) by experimental techniques, the numerical analysis is here used as a powerful tool to retrieve these information and link it to the macroscopic response of the system.

4.7.1 Macroscopic stick-slip instability

Figure 4-15 shows the system response and the local behaviour in the case of macroscopic stick-slip instability for $\beta=5e-10$ s (detailed in section 4.3) during the first macro-slip event. Figure 4-15(a) represents the nodal velocity field (along x direction) of the system and the contact status distribution at the time $t=7.47e-4$ s. The scale of the velocity magnitude is given on the left; the local contact status can be either stick (bleu), sliding (green) or detached (red). Figure 4-15(b) shows the global response (tangential and normal forces) of the system, for the considered time interval (rotated zoom of Figure 4-1). Figure 4-15(c) shows the contact node status along the time for the considered interval. The x-scale represent the contact line, while the y-scale is the time. Reading the graphic from the bottom to the top, it is possible to see the evolution of the contact status (along the whole interface) during the considered time interval.

In a first phase, while the global tangential force increases over the time, a part of the contact nodes changes its status switching from sticking to sliding state (Figure 4-15(c)). The sliding onset of the contact node in the left-side of the interface respect to the centre, is due to the deformation of the samples and the non-homogeneous initial stress distribution due to the imposed relative displacement at the boundaries. Different micro-slip front coalesce and grow giving origin to the so called “slow front” phase. Then, when the tangential force reaches larger values, rupture propagations occur at the contact interface leading to detectable drops of the tangential force (precursors). In this second phase the switching of the nodes in sliding or detachment state, is more rapid due to the rupture fronts (Figure 4-15(a)). When the rupture fronts have a sufficient energy to propagate along the whole interface, the waves coming from the contact interface reach the boundaries (Figure 4-15(a)) and arrive to cause the macroscopic slip event. The waves originated at the contact are reflected into the bodies, exciting the system dynamics and influencing again the contact behaviour recursively. An extensive analysis of the complex dynamics at the contact interface and the interaction between rupture propagation and system dynamics during the macroscopic stick-slip behaviour is presented in [17].

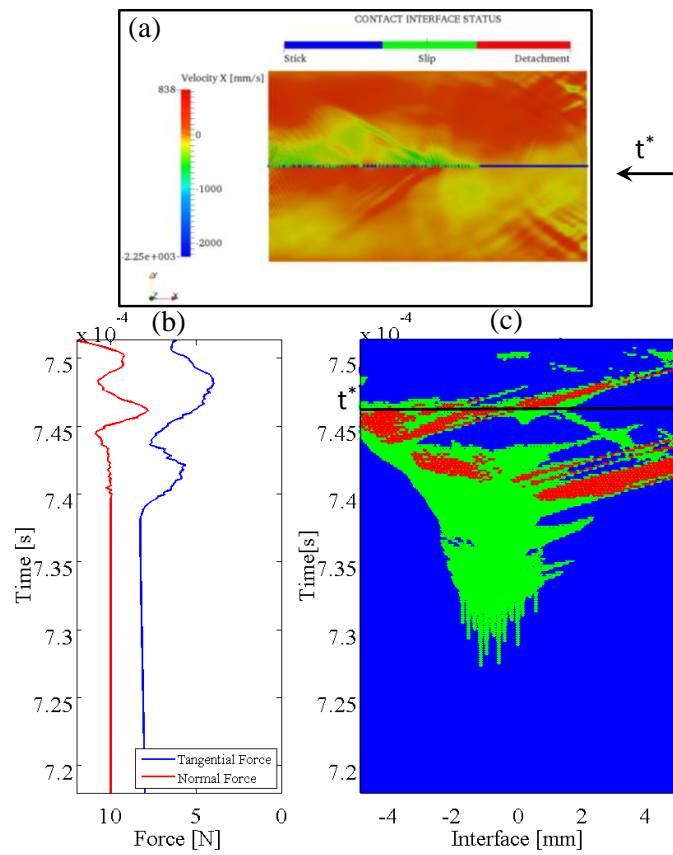


Figure 4-15: (a) X-Velocity distribution of the system and status of the contact nodes at time $t^* = 7.47e-4$ s for $\beta = 5e-10$ s. (b) Time evolution of the global (tangential and normal) contact forces for $t \in [7.10e-4 \div 7.51e-4]$ s. (c) Status of the interface contact nodes for the same time interval: green dots=slip, blue dots=stick, red dots=detachment.

4.7.2 Mode coupling instability

The interaction between local contact behaviour and the dynamic response of the system in the case of mode coupling instability ($\beta = 1e-8$ s) is highlighted in Figure 4-16. The status distribution of the contact interface along the time is reported in Figure 4-16(b) where a periodic switch of the contact area in sticking and sliding is reported once the system unstable vibrations grow up; the period correspond to the fundamental harmonic of the vibration at 406 kHz, corresponding to the unstable mode of the system. Figure 4-16(a) shows the nodal velocity field calculated along the x direction at the time t^* . Looking at the Figure 4-16(a) and Figure 4-16(c), it can be seen how the actual deformation of the system is directly related to the local sliding and sticking distribution:

different amplitude or direction of the local tangential velocities of the two bodies, at the contact interface, brings the contact nodes in a sliding state; on the other hand, where the local tangential velocities of the two bodies are the same, due to the system deformation, the contact nodes stay in sticking state. For this reason the interface state, during “continuous apparent macroscopic sliding”, shows a periodic evolution of the local contact status distribution (Figure 4-16(c)) along the time, at the fundamental frequency (406 kHz) of the unstable mode. The switch in sticking or detachment state of part of the contact surface is the only nonlinearity accounted for in the transient model, allowing the limit cycle of the self-excited vibrations. The magnifications reported on the right of Figure 4-16(c) show the detail of the contact status distribution over the time during the exponential grow of the vibration (zoom 1) that brings to a progressive increase of the areas that switch in stick state (at the period of the unstable mode), and during the nonlinear phase (zoom 2) when the limit cycle is reached and the amount of sticking zones reach its maximum value.

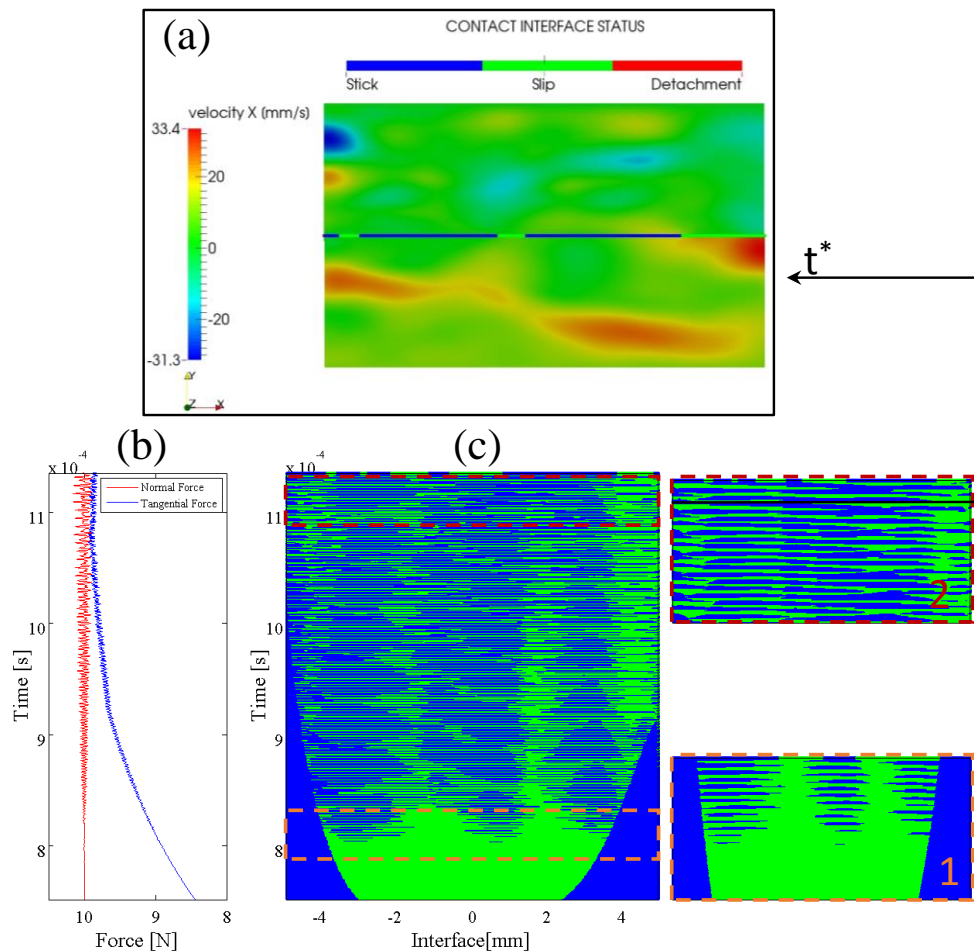


Figure 4-16: (a) *X*-Velocity distribution of the system and status of the contact nodes at time $t^*=1.15e-3$ s for $\beta = 1e-8$ s. (b) Time evolution of the global (tangential and normal) contact forces for $t \in [7.5e-4 \div 1.355e-3]$. (c) Status of the interface contact nodes for the same time interval: green dots=slip, blue dots=stick, red dots=detachment.

Figure 4-17 shows the same global system behaviour explained in the previous section but this time referred to the mode coupling instability at 63 kHz ($\beta=1e-7$ s). As in Figure 4-16 the switching of the contact nodes in sticking and slipping conditions (Figure 4-17(c)) is due to the deformation of the system (Figure 4-17(a)) due to the unstable vibration, which guides the local behaviour at the contact. Comparison between Figure 4-16 (higher frequency instability) and Figure 4-17 (lower frequency instability) highlights as the system unstable response influences differently the local contact behaviour during macroscopic continuous sliding in function of the unstable mode excited by the frictional contact forces. On the other hand the contact non-linearities (switching of the contact nodes in stick-slip-detachment status) modifies the system response during the limit cycle leading to sub/super-harmonics of the main frequency peak in the system response.

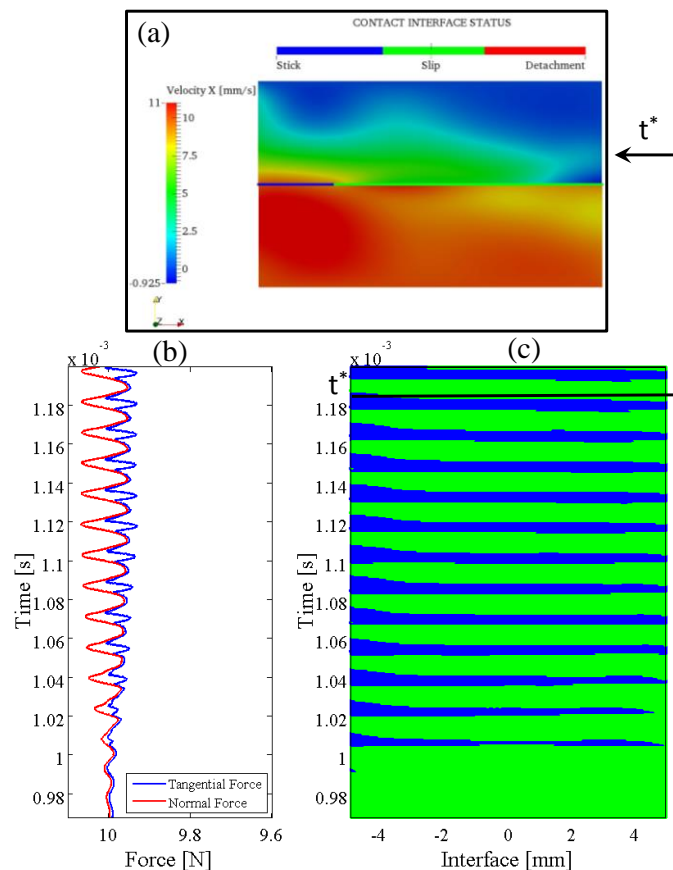


Figure 4-17: (a) X-Velocity distribution of the system and status of contact nodes at time $t^*=1.185e-3$ s for $\beta = 1e-7$ s. (b) Time evolution of the global (tangential and normal) contact forces for $t \in [0.97e-3 \div 1.20e-3]$. (c) Status of the interface contact nodes for the same time interval: green dots=slip, blue dots=stick, red dots=detachment.

4.7.3 Stable continuous sliding

When the system is characterized by stable response during continuous sliding (Figure 4-18(a)), as in the case explained in the section 4.5, the local contact behaviour is represented by the Figure 4-18(b). While the tangential force increases reaching the limit imposed by the frictional contact law, the interface part in sliding increases until the whole contact surface stays in sliding condition and no relevant oscillations are present in the system response (Figure 4-18(a)). It should be highlighted that these simulations are developed in absence of surface roughness; its introduction at the contact interface would cause a further local excitation and local dynamics which induce low amplitude vibrations due to the response of the system dynamics [83, 84, 91].

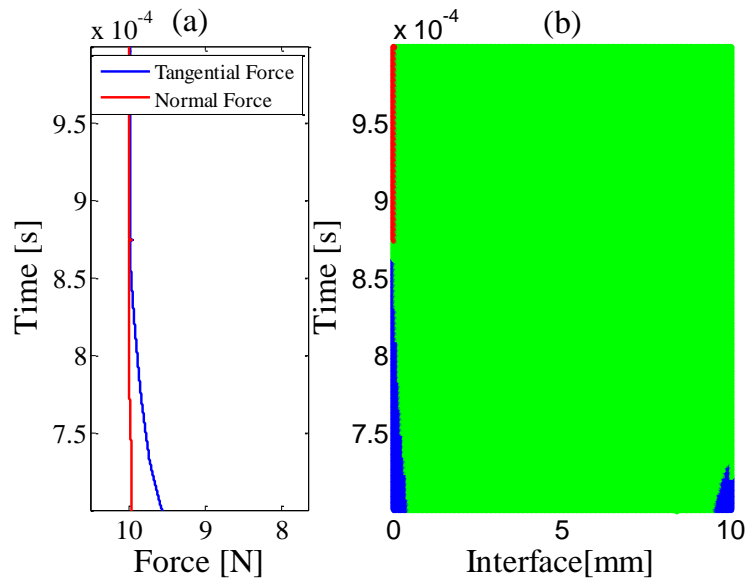


Figure 4-18: (a) Time evolution of the global (tangential and normal) contact forces for $t \in [0.7e-3 \div 1.355e-3]$ and $\beta = 1e-6$ s. (b) Status of the interface contact nodes for the same interval time: green dots=slip, blue dots=stick, red dots=detachment.

4.8 Discussion of results: contact scenario map

The instability scenarios of a mechanical system under frictional contact have been numerically investigated. The presented results show how, by varying a system parameter, the macroscopic frictional dynamics can be characterized by macro stick-slip phenomena, or harmonic vibrations due to the mode coupling instability, or stable state in continuous sliding.

The selection mechanism between these scenarios is a combination of the local contact dynamics, detailed in [17], and its coupling with the macroscopic dynamic response of the mechanical system.

The non-linear transient simulations and the complex eigenvalue analysis highlight that the damping parameters α and β affect the system frictional response in a different manner, resumed in Figure 4.13.

The mass matrix damping coefficient α :

- i) plays a key role on the damping of the system response (excited system vibrations) when the behaviour of the system is dominated by stick-slip phenomena (Figure 4-19);
- ii) affects the stability of low frequency modes and the limit cycle amplitude during continuous sliding with mode coupling instability (Figure 4-9).

The stiffness matrix damping coefficient β :

- i) affects, by damping the local dynamics (wave and rupture propagation) at the contact, the macroscopic frictional behaviour of the system that shifts from stick-slip to continuous sliding.
- ii) affects the damping and mode coupling instability of higher frequency modes.

The performed non-linear numerical analysis shows the existence of two zones defined by a critical value β^* (equal to $1e-8$ s for the presented model).

- For $\beta < \beta^*$ the behaviour of the whole system is mainly dominated by macro stick-slip instability;
- for value of $\beta > \beta^*$ the system reaches the status of “continuous sliding” with or without mode coupling instability.

When $\beta \geq \beta^*$ both the transient simulations and the CEA showed that increasing β the oscillations due to unstable modes shift in frequency, passing from a higher frequency mode to a lower one. This is due to the linear

contribution (with respect to the frequency) of β to the modal damping, which has a larger stabilizing effect for the modes at higher frequencies.

For values of $\beta > 5 \times 10^{-8}$ s the time system response exhibits a fundamental frequency peak at about 65 kHz, which corresponds to the unstable frequency calculated by the CEA; for smaller values of β the transient simulation exhibits a fundamental harmonic vibration corresponding to a higher frequency mode (405 kHz), predicted to be unstable by the CEA too.

Finally, increasing both α and β each eigenvalue calculated by CEA with the linear model is stable and no oscillations during the continuous sliding are observed in the transient non-linear response of the system (Figure 4-19).

The instability map presented in Figure 4-19 wants to resume the possible instability scenarios between two elastic media in sliding contact as a function of the material damping parameters. From both transient nonlinear simulations and linear CEA, three main regions can be identified:

- stick-slip instability zone, characterized by macroscopic stick-slip frictional behaviour;
- mode coupling instability zone, characterized by continuous sliding with harmonic self-excited friction induced vibrations, due to an unstable mode;
- stability zone, characterized by continuous sliding with no relevant oscillations in the transient response of the system.

The switch from the macroscopic stick-slip behaviour to continuous sliding is dominated by the β damping parameter, because affecting the high frequency phenomena occurring locally (contact rupture and wave propagation) and their coupling with the system dynamics.

The switch to mode coupling instability is affected by both the α and β parameters as a function of the frequency of the unstable mode.

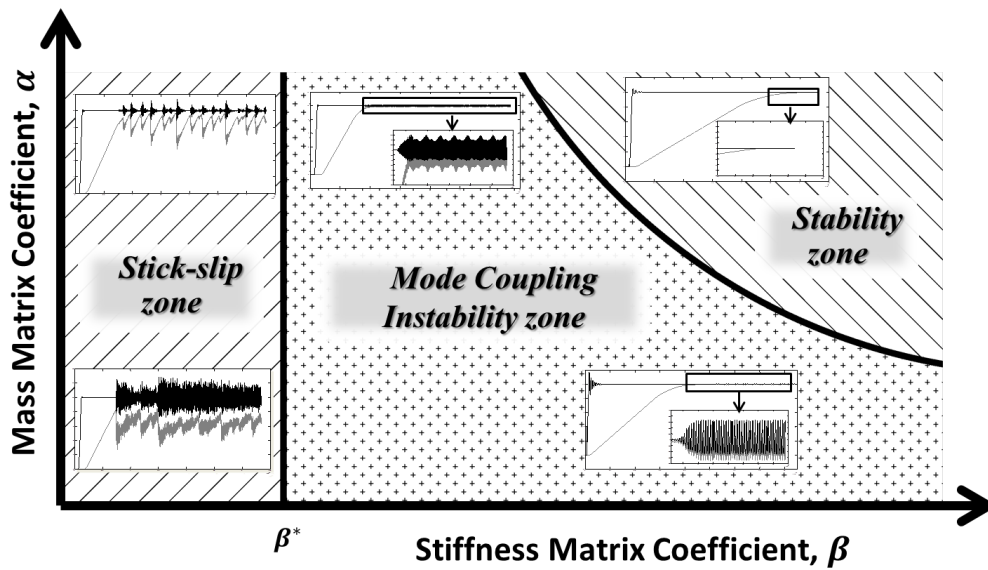


Figure 4-19: Instability scenario map as a function of damping parameters.

No scales are reported in the map axes, presented in Figure 4-19, because the material damping is just one of the parameters that affect the response of the frictional system: system geometry, surface roughness, applied boundary conditions, friction coefficient and contact law, other material properties [94] like Young modulus or Poisson ratio, etc.

The effects of all these parameters on the selection mechanism of the instability scenarios are deeply interrelated and the threshold of α and β that define the zones presented in Figure 4-19 changes in function of the other system parameters. By the two presented numerical approaches (transient non-linear simulations and parametrical CEA), qualitative maps of the instability scenarios can be drawn as a function of several parameters.

5 Preliminary experimental analysis and qualitative numerical comparison

5.1 Introduction

The chapter presents experimental observations of the frictional macroscopic behaviours reproduced in a laboratory set-up (see section 3.2).

The macroscopic response of two elastic media in relative motion has been investigated experimentally, highlighting how the contact frictional behaviour is affected by the imposed boundary conditions. Macroscopic stick-slip, mode coupling instability and the transition to stable continuous sliding have been observed.

The first part of the chapter shows the results obtained by the experimental analysis of two polycarbonate blocks in sliding motion. As a function of the boundary conditions (load and relative velocity) the same system exhibits different frictional behaviour switching from macroscopic stick-slip phenomena to mode coupling instability up to stable continuous sliding. A different structural response (vibrations amplitude, excited frequencies and accelerations) of the system has been observed as a function of the frictional response.

The second part of the chapter shows a preliminary (qualitative) comparison between numerical and experimental analysis as a function of same parameters. In the finite element model a contact law that considers the coefficient of friction as a function of the adherence time (see section 2.2.3) is accounted for, in order to simulate the frictional behaviour of the polycarbonate. The explicit finite element code PLASTD has been used to perform the numerical transient analysis.

The frequency and time analysis of the experimental tests exhibits a good qualitative agreement with the numerical results obtained through the transient contact simulations. Maps of the instability scenarios have been drawn as a function of boundary conditions both experimentally and numerically. With respect to the previous chapter, where the investigated driving parameter was the material damping, the numerical analysis is here developed as a function of parameters that can be varied experimentally (load and velocity).

5.2 Materials and method

The description of the experimental test bench used to provide the relative motion of two elastic blocks in contact with a defined contact pressure is presented in the section 3.2.

Two blocks of polycarbonate (see Figure 3-1) have been used to carry out the experimental tests. The material and geometrical properties of the polycarbonate blocks are reported in the following table:

Polycarbonate	
Length [mm]	30
Width [mm]	10
Thickness [mm]	5
Density [kg/m³]	1190
Young Modulus [GPa]	2.65
Poisson coefficient	0.4

Table 2: Geometrical and material properties of polycarbonate blocks used to perform the experimental analysis.

The dimensions of the specimens (Table 2) are set in order to obtain both an acceptable planarity of the two contact surfaces and a considerable average contact pressure. The contacting faces of the two blocks have been polished and each contact face has been cleaned before performing the tests.

In the first phase of each test, the lower and upper specimens are put in contact applying a compressive normal force F ; afterward a constant velocity V is imposed on the upper specimen to bring the blocks in frictional relative motion (Figure 3-1). The global signals (tangential force, normal force, tangential acceleration and imposed displacement) have been recorded with a sample frequency of 50 kHz by the OROS acquisition system. The translational velocity is imposed to the slider block with high resolution in order to avoid artificial stick-slip phenomena induced by the set-up control system.

An experimental parametrical analysis, as function of the driving velocity and the normal load, has been performed. Four different values of normal force have been tested, 150 N, 450 N, 750 N, 1000 N, corresponding to an average contact pressure of 1 MPa, 3 MPa, 5 MPa, 6.6 MPa respectively. For each value of the normal load, the driving velocity has been ranged between 10 mm/s and 2 μ m/s with a maximum total displacement of 5 mm.

5.3 Frictional observations: role of boundary conditions

This section presents the different macroscopic frictional behaviours observed experimentally between the two elastic bodies, when the relative translational velocity is varied. Experimental tests have been performed ranging the velocity of the upper slider block, while the normal load is fixed to 750 N in order to obtain an average contact pressure of 5 MPa. At the end of the section, the effect of normal load and imposed horizontal velocity on the contact scenarios is resumed in the contact scenario maps.

5.3.1 Macroscopic stick-slip instability

Figure 5-1 shows the system frictional response for an imposed driving velocity of 1 mm/s. The blue and green curves show respectively the tangential and normal global forces recorded by the force transducer. The black curve represents the imposed displacement in order to have constant translational velocity along the x direction. First, a normal force along the y direction is applied to the system in order to obtain an initial average normal pressure of 5 MPa. After this preload phase (not reported in Figure 5-1) a constant velocity is imposed to the lower boundary of the body 2.

After a first ramp due to the tangential loading phase, the curve of the tangential force (Figure 5-1) exhibits periodic drops and subsequent ramps along the recorded time. Each increase of the tangential force (increase of elastic energy stored in the system) is followed by a sudden drop due to the following macro-slip event (rupture and wave propagations) at the contact surface [17]. The slope of the initial tangential curve is function of the tangential stiffness of the whole system during the tangential loading phase. During each load phase, until the tangential force reaches the maximum value, the bodies are mainly in adherence status while some contact zones can switch in sliding state before the macro-slip due to the interface rupture propagation (precursors), as shown in [17, 19, 20].

Then, a sudden macroscopic slip occurs with the consequent drop of the tangential force. The sliding of the whole interface is due to the rupture and wave generation and propagation at the contact interface that produces the release of the elastic energy stored in the system during the loading (sticking) phase. The detail of the rupture propagation phases before the macro-slip event is reported in [17].

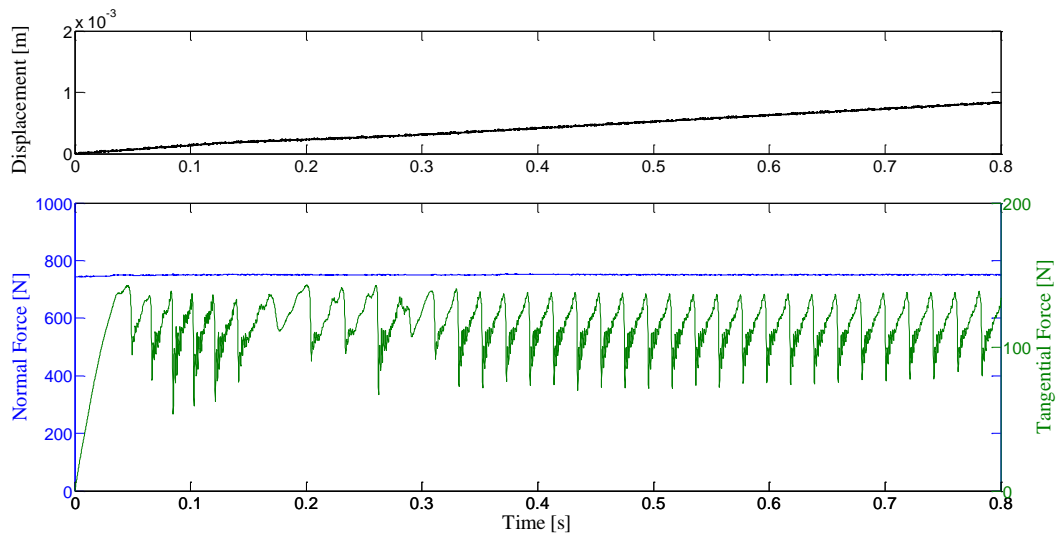


Figure 5-1: Imposed displacement (up); normal (y direction) force and tangential (x direction) force (down). Experimental data obtained with the following parameters: imposed driving velocity 1 mm/s and normal load 750 N.

The macroscopic slip of the contact interface represents an impulsive excitation for the system and the generated vibrations, measured by the piezoelectric accelerometer (see Figure 5-4), are related to the dynamic response of the whole set-up. The Figure 5-4(b) shows the spectrum of the acceleration signal for the time interval Δ_1 , i.e. a time period between two macro slip, characterized by the response to the impulsive (force drops) system excitation; the first natural frequencies (110 Hz, 600 Hz, 900 Hz, 1500 Hz, 2400 Hz) of the whole system are excited. On the other hand, the spectrum in the Figure 5-4(c) is referred to a larger time interval Δ_2 and shows a superposition of the superharmonics of the stick-slip frequency (50 Hz) together with the excited natural frequencies of the system. Thus, the macroscopic frictional behaviour, characterized by periodic drops of tangential force and referred in literature as stick-slip [26], is originated by the local contact rupture propagation that excites the whole system dynamics. The propagation of the contact waves and the interaction with the structural dynamics play a key role into defining the frictional behavior of two elastic media in relative motion. This kind of frictional instability can occur in any mechanical system with frictional interfaces and it is also referred as the main mechanism at the origin of earthquakes [29].

5.3.2 Mode coupling instability

Increasing the driving velocity and maintaining fixed the normal force (750 N), the macroscopic frictional behaviour changes its pattern (Figure 5-2). Figure

5-2 shows the system behaviour for an imposed driving velocity equals to 5 mm/s. After the preload phase, the translational velocity is imposed and the tangential force (green curve in Figure 5-2) reaches its maximum value, which is higher than the mean tangential force at steady sliding state. Then, after the first macroscopic slip, the system shows large oscillations of the global frictional force around its mean constant value, increasing up to a maximum amplitude of oscillation (green curve in Figure 5-2). Furthermore the recorded acceleration highlights the typical behaviour of mode coupling instability (see Figure 5-4(d)): a first phase (time interval Δ_1 in Figure 5-4(d)) with an initial exponential increase of the oscillations and an harmonic spectrum at the unstable natural frequency, followed by a second phase where the response is bounded to a limit cycle (time interval Δ_2 in Figure 5-4(d)). The spectrum of the first phase (Figure 5-4(e)) shows a main frequency peak, representing the fundamental harmonic at 110 Hz. The relatively low frequency of the vibrations is associated to an unstable mode of the whole experimental set-up. The spectrum in the second phase (Figure 5-4(f)) shows the main harmonic at 110 Hz and the respective super-harmonics of the signal, due to the contact non-linearities that bound the vibration. The harmonic vibrations in Figure 5-4(f), induced by frictional contact forces, are typical of mode coupling instability [24, 78]. In fact, when the two bodies are in relative motion the contact forces can excite an unstable mode of the system [24] and, after an initial exponential increase of the vibration, a limit cycle is reached; the acceleration signal in Figure 5-4(d) shows the exponential increasing until the material damping and contact non-linearities stabilize the system response. This kind of contact scenario, typically studied in disc brake or clutch systems, has been experimentally highlighted also here for general mechanical system under frictional contact. The same contact scenario has been analysed numerically in [24] where the interaction between local behaviour at the contact and system dynamics has been analysed as a function of the material damping.

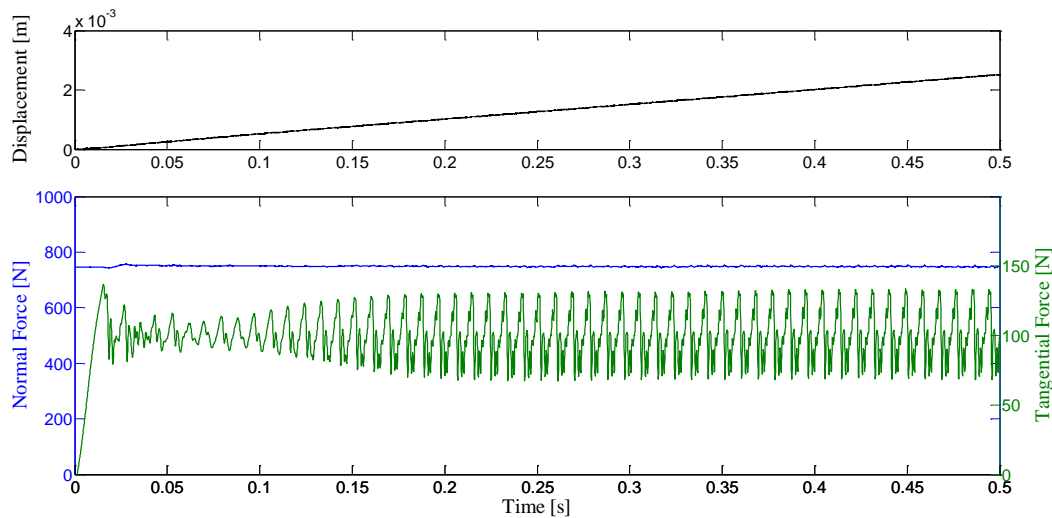


Figure 5-2: Imposed displacement (up); normal (y direction) force and tangential (x direction) force (down). Experimental data obtained with the following parameters: imposed driving velocity 5 mm/s and normal load 750 N.

5.3.3 Stable continuous sliding

Considering the same mechanical system, Figure 5-3 shows its macroscopic behaviour during relative motion obtained for a translational velocity of 10 mm/s, while the normal load is fixed to 750 N. First, the tangential force reaches its maximum value, higher than the tangential force at the steady state; afterwards the entire system remains in sliding status and the frictional force stabilizes (decaying oscillations) reaching the steady value. On the other hand, the acceleration signal in the Figure 5-4(g) shows typical decaying oscillations excited by the initial drop of the tangential force (Figure 5-3); the spectrum of the signal in this first phase (Figure 5-4(h)) shows how the decaying oscillations are related to the excited first natural frequencies of the set-up. Afterwards the system response is stable and no relevant oscillations can be observed from the recorded signal and its related spectrum (Figure 5-4(i)).

In this case the relative motion between the two bodies of polycarbonate can be considered stable and the structural dynamics of the system is not excited (not relevant oscillations), as it can be observed from the measured tangential force and acceleration. The extremely low vibrations and relative low spectrum that can be seen in Figure 5-4(i) are due to “stable” friction induced vibrations due to the surface roughness and the parasitic noise coming from the set-up.

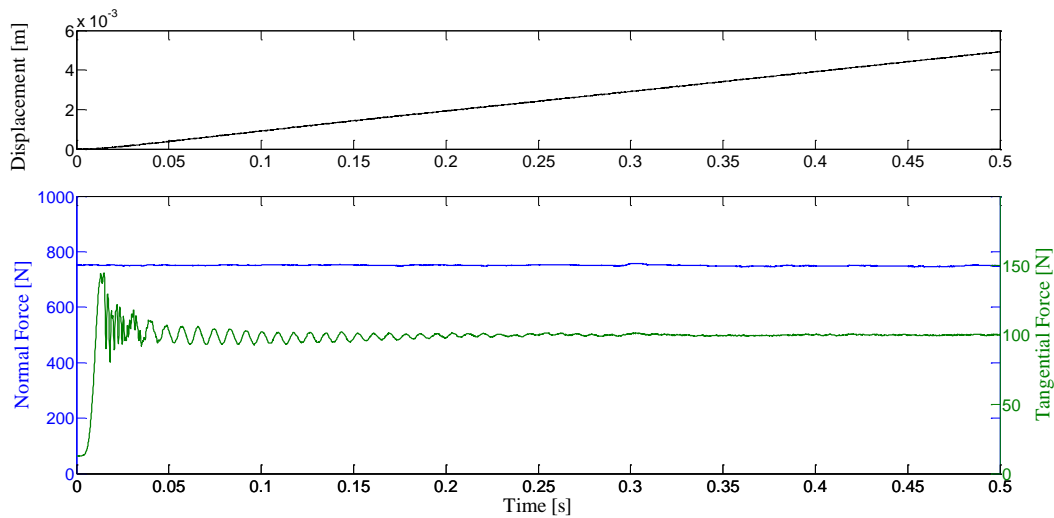


Figure 5-3: Imposed displacement (up); normal (y direction) force and tangential (x direction) force (down). Experimental data obtained with the following parameters: imposed driving velocity 10 mm/s and normal load 750 N.

5.3.4 Discussion on experimental frictional scenario map

The experimental results presented above showed how a simple frictional system can exhibit different macroscopic contact scenarios (macro stick-slip, mode coupling instability, stable continuous sliding) as a function of the only boundary conditions. Figure 5-4 shows as the frictional contact forces can excite the system dynamics differently, when increasing the imposed driving velocity. The macroscopic behaviour of the system can be characterized by intermittent interface motion and impulsive excitation of the system (macro stick-slip instability in Figure 5-4(a)), continuous sliding at the interface with harmonic vibration of the system (mode coupling instability in Figure 5-4(d)) or continuous stable sliding state (Figure 5-4(g)). The spectrum of the tangential acceleration during the macro stick-slip scenario (Figure 5-4(c)) highlights how the system vibration amplitude is lower with respect to the amplitude of the acceleration in the limit cycle during mode coupling instability (Figure 5-4(f)). Furthermore, in the first case the system behaviour is characterized by intermittent interface motion, while in the second case the system can be considered in macroscopic continuous sliding state with large periodical oscillations of the local contact forces, up to reach local changes in the contact status (local stick slip and detachment) [17, 24].

The same transition from stable continuous sliding state to macro stick-slip instability has been also observed experimentally as a function of normal load, ranging from 150 N (1 MPa) up to 1000 N (6.6 MPa), maintaining fixed the imposed horizontal velocity (Figure 5-5). The experimental parametrical analysis, carried out on the two blocks of polycarbonate as a function of the boundary conditions allowed for drawing a contact scenario map of the system. Figure 5-5 highlights the role of normal load and imposed velocity into the switching from macroscopic stick-slip instability and continuous sliding behaviour with or without mode coupling instability. For low normal load (low average contact pressure) the system is characterized by stable behavior for the whole imposed velocity range (between $2 \mu\text{m/s}$ to 10 mm/s). Increasing the normal load the system starts to exhibit unstable contact behavior for relative low imposed velocity, as shown in the Figure 5-5. It should be noticed that the mode coupling instability has been obtained only for an unstable mode at relative low frequency, 110 Hz, which is a mode of the whole experimental set-up. In fact, a numerical complex eigenvalue analysis performed on the used polycarbonate samples alone, didn't predict unstable modes related to the sample modes (at several kHz).

Similar maps of the frictional behavior can be drawn numerically for other system parameters, as shown in [24].

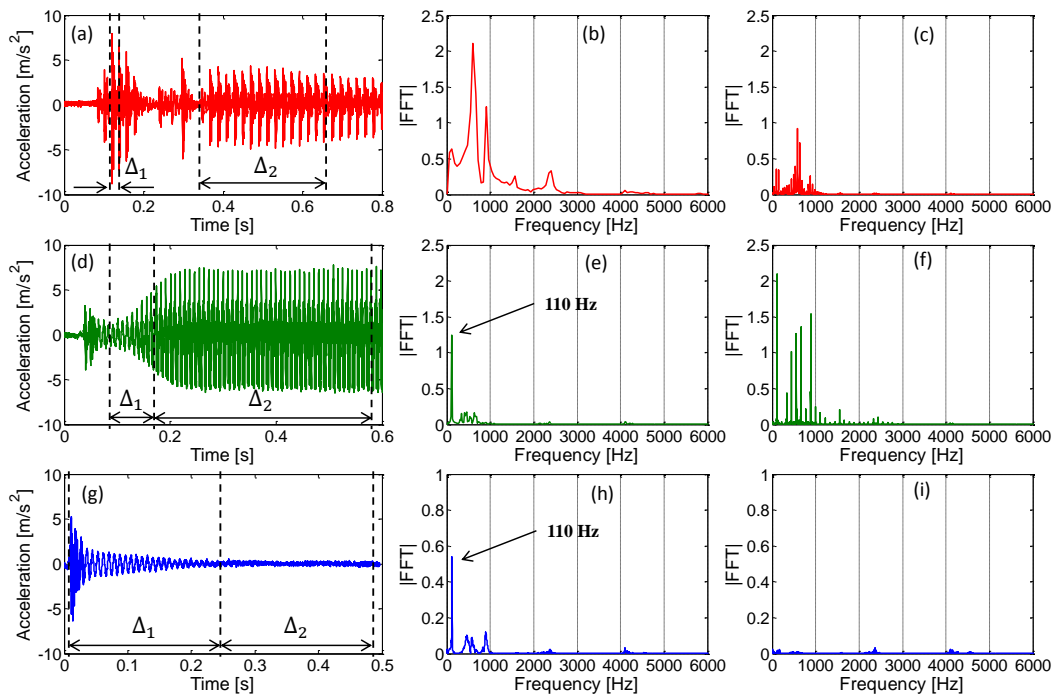


Figure 5-4: Experimental scenarios for normal load equal to 750 N. (a) (b) (c)- macro stick-slip instability for $V=1 \text{ mm/s}$; (d) (e) (f)- mode coupling instability for $V=5 \text{ mm/s}$; (g) (h) (i)- stable continuous sliding for $V=10 \text{ mm/s}$.

Alongside each contact scenario (acceleration signals) the spectrum related to different time period Δ_1 and Δ_2 is shown.

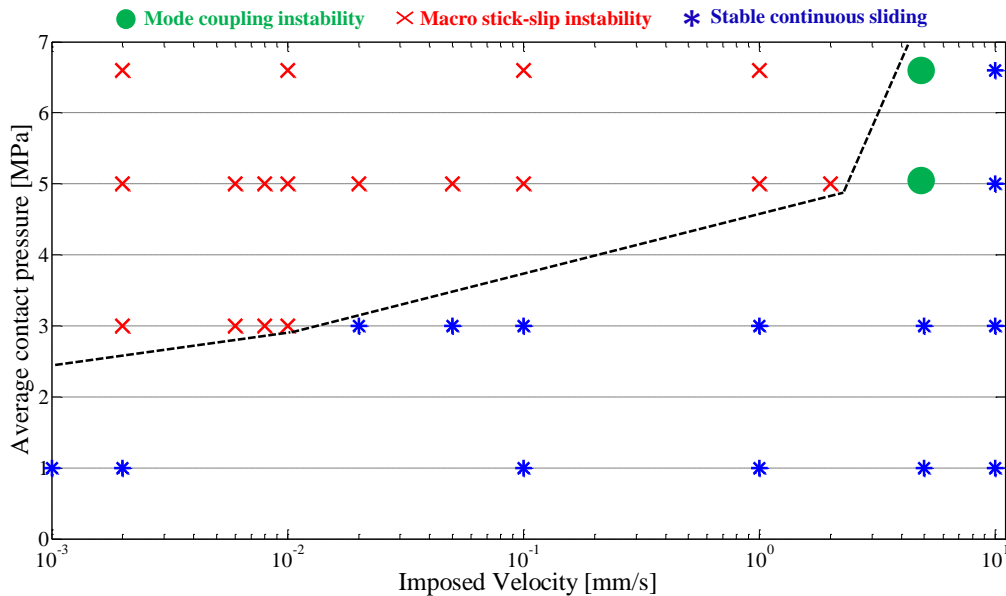


Figure 5-5: Experimental map of the frictional contact scenarios as a function of the imposed driving velocity and average contact pressure.

5.4 Qualitative comparison between experimental and numerical results

This section presents the comparison with numerical results obtained by transient contact non-linear simulations. While Chapter 4 showed the numerical investigation of the frictional contact scenarios as a function of the material damping parameters, in this Chapter the effect of the relative motion and applied load is investigated for comparison with the experimental results. A good agreement between numerical and experimental scenarios is presented, showing comparable behaviours as a function of the boundary conditions.

5.4.1 Numerical model

The 2D model (plane strain deformation) consists of two isotropic elastic finite media separated by a frictional interface; for the presented analysis, at each node of the contact interface, the friction law as a function of adherence

time (explained in section 2.2.3) is imposed. The material and geometrical properties of the numerical model are listed in Table 3. The reference values of the material damping parameter have been recovered by means of experimental tests on Polycarbonate detailed in [95]. A force distribution along the y axis, giving a global force F , is applied at the bottom of the body 2. After the preload phase, the global normal force F is maintained constant and a translational velocity V , along the x direction, is applied at the lower edge of the body 2 to bring the system in relative motion; the body 1 is maintained fixed at its upper side.

	<i>Body 1</i>	<i>Body2</i>
Length [mm]	30	30
Width [mm]	10	10
Element Number	30000	5590
Contact element size [mm]	0.1	0.23
Young Modulus [GPa]	2.65	2.65
Density [kg/m³]	1190	1190
Poisson ration	0.40	0.40
Material damping: Alpha [1/s]	40	
Material damping: Beta [s]	1e-7	
Integration time step [s]	9e-9	

Table 3: Geometry dimensions, material and mesh properties used to perform the non-linear simulations.

5.4.2 Definition of the friction law

In the present numerical analysis the coefficient of friction is not assumed to be a constant value (Amontons-Coulomb friction law).

In particular, the value of the friction coefficient between the two surfaces of polycarbonate has been observed experimentally to be a function of the sticking (adherence) time between the two surfaces; this behaviour can be probably attributed to the physicochemical reactivity of the polycarbonate blocks at the interface, which increases the static friction coefficient (adhesion) with the increase of the adherence time.

The definition of a reliable law of friction has been derived by the experimental tests carried out on the polycarbonate blocks.

Figure 5-6 shows the curve fitting of experimental points of the macroscopic friction coefficient, obtained considering the performed experimental tests for an average contact pressure of 5 MPa. The experimental data (red triangles in Figure 5-6) represent the static friction coefficient calculated as the maximum ratio between tangential force (peaks of the tangential force ramps) and normal force recorded during the macro stick-slip instability behaviour for a fixed imposed driving velocity. At each experimental point in Figure 5-6 has been associated the adherence time calculated by the period of the stick phase (force ramps of the stick-slip events) for each considered imposed driving velocity. This assumption has been considered under the hypothesis that between two following macro slip, observed experimentally, the contact interface stays in adherence (stick phase).

The point marked by a black dashed circle is the dynamic friction coefficient experimentally estimated as the ration between the tangential force and normal load in the case of stable continuous sliding (Figure 5-3), equivalent to a nil adherence time.

The curve fitting of the experimental results led to obtain an analytical curve of the friction contact law (equation 8) able to be implemented in the numerical contact model.

The experimental analysis of the friction coefficient highlighted some important variations of static coefficient for short adherence times and a stabilization of friction curve for long time of adherence, as shown in Figure 5-6. This kind of friction law wants, in a simple way, to account for the complex mechanisms at the contact interface such as adhesion, physical and chemical actions, and viscoelastic deformations of asperities that occur at the interface. These mechanisms play a key role into define the local frictional contact behaviour, but at the same time they are difficult to be implemented in a numerical model [43, 96]. Nevertheless, the experimental macroscopic measurements of the contact forces allow for defining reliable parameters of the friction law to be representative, as much as possible, of the local physics at the interface.

The same behaviour of the macroscopic friction coefficient, shown in Figure 5-6, has been also observed for the average normal pressure of 3 MPa and 6.6

MPa; then, a similar friction law has been estimated for each values of the contact pressure, modifying the parameters A, B, C as a function of the experimental points (Table 3). The difference on the friction, observed experimentally, as a function of the average pressure could be due to the effects of the real contact pressure on the surface phenomena listed above.

It has been also observed numerically that determining the static friction coefficient from the time evolution of tangential force (peak of the force ramps) underestimates the real value of the local static friction coefficient [19, 24, 51]; in fact the difference between apparent (macroscopic) and real (local) static friction coefficient is due to the local contact dynamics at the frictional interface, which lead to have macro-sliding events (force drops) for a tangential force lower than the upper limit imposed by the local friction coefficient at the contact, as explained in the recent literature [17, 58]. After these considerations, in order to perform the comparison between experimental and numerical results obtained by the nonlinear transient analysis, the values of static friction coefficient has been increased of 15 % as showed by the friction law reported in Figure 5-6 (green curve). In such a way, the imposed local friction coefficient at the contact nodes is representative to obtain the macroscopic friction coefficient obtained by the experimental curves.

Average contact pressure [MPa]	A	B	C	Max Static friction coefficient (A+B)	Dynamic friction coefficient (B)
3	0.14	0.20	30	0.34	0.20
5	0.16	0.135	30	0.295	0.135
6.6	0.14	0.125	35	0.265	0.125

Table 4: Parameters of the local friction law implemented in the numerical model.

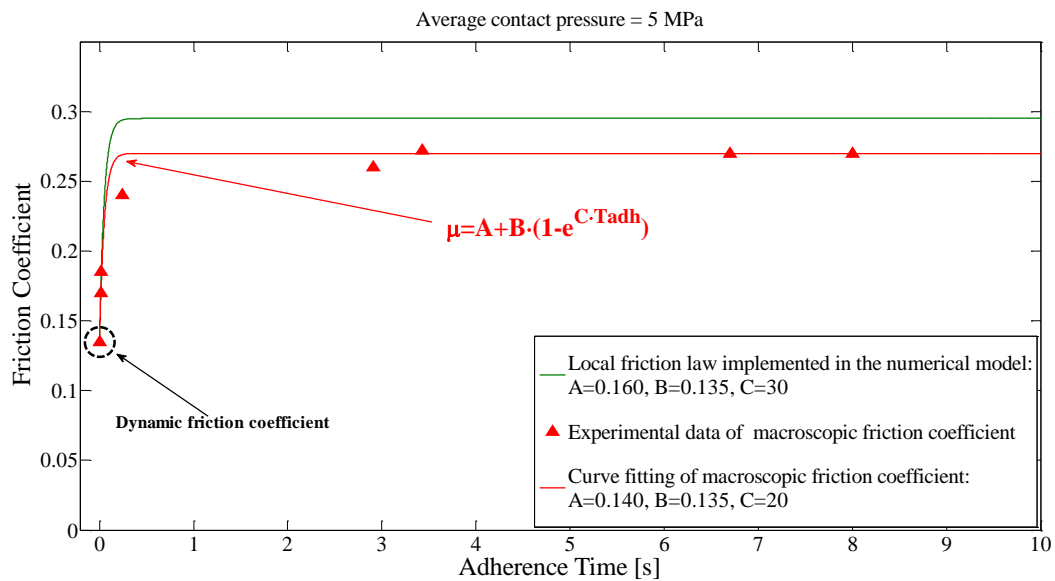


Figure 5-6: Curve fitting of friction contact law implemented in the finite element model for an average contact pressure of 5 MPa.

5.4.3 Effect of the imposed boundary conditions

This section presents a comparison between the experimental tests and the numerical results carried out by means of the transient non-linear simulations. The effect of the boundary conditions, imposed driving velocity and normal force (average contact pressure), has been numerically investigated considering the 2D plane strain model, for which the contact behaviour is the only non-linearity accounted for (see section 5.4.2). The black curve in Figure 5-7 shows the displacement imposed at the lower edge of the model in order to obtain a relative velocity of 1 mm/s; the blue and the green curve in the figure represents respectively the recovered normal contact force and the tangential contact force; like in the experimental tests, before applying the constant translational velocity, a preload phase has been realized to bring the two blocks in contact with average normal pressure of 7.6 MPa. The simulation results highlight how the system behaviour is characterized by stick-slip phenomena (Figure 5-7). After a first linear growth, the tangential contact force exhibits repetitive fluctuations (ramps and sudden drops). The release of elastic energy during the drops produces strong vibrations into the system. The same contact scenario characterized by macro stick-slip has been revealed experimentally for an imposed velocity of 1 mm/s and average pressure of 6.6 MPa (Figure 5-1).

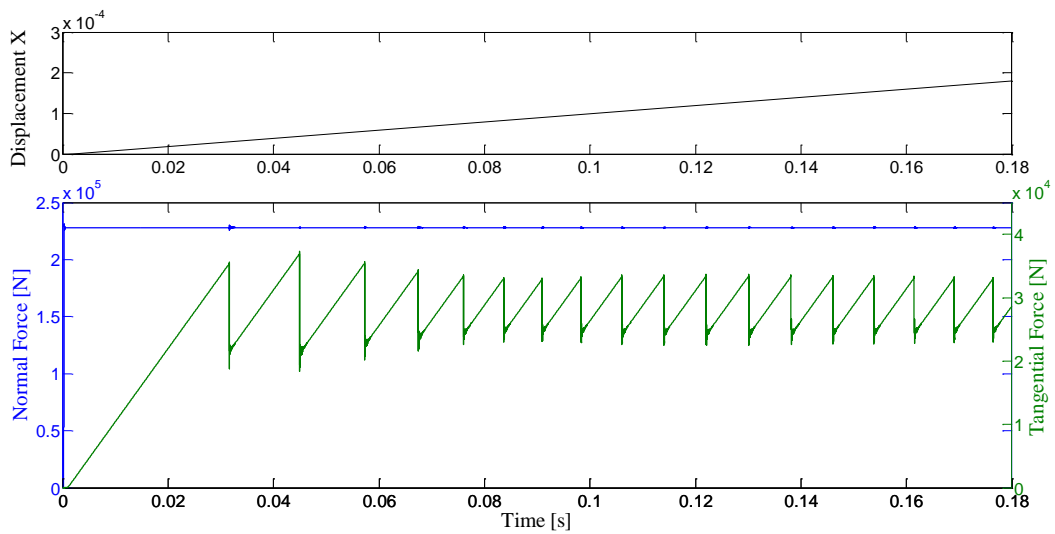


Figure 5-7: Imposed displacement at lower edge of body 2 (up); normal force (along y direction) and tangential force (x direction) measured numerically at the upper edge of the body 1. Imposed boundary condition: horizontal velocity $V=1$ mm/s and average contact pressure 7.6 MPa.

Figure 5-8 shows the effect of the imposed driving velocity, both experimentally and numerically, on the macroscopic frictional behaviour. The macroscopic friction coefficient along the time has been calculated as the ratio between the total tangential force and normal force measured at the boundaries for both the numerical and experimental tests. Ranging the imposed velocity from 10 mm/s to 1 mm/s and maintaining fixed the normal force (average pressure of 7.6 MPa) the behaviour of the numerical system changes its pattern (Figure 5-8, right) as shown also in the experimental measurements (Figure 5-8, left). For a driving velocity of 10 mm/s and an average contact pressure of 7.6 MPa the numerical model exhibits a typical stable continuous sliding behaviour (Figure 5-8(d)) as observed experimentally for the same value of the sliding velocity and an average pressure of 6.6 MPa (Figure 5-8(a)). The friction coefficient shows a linear increase until it reaches the maximum value and, after a sudden drop due to the released of elastic energy, its value stays constant. The initial drop in the friction coefficient (related to tangential force drop) produces an excitation that leads to decaying oscillations of the system (Figure 5-8(d)). After this first phase of transition from adherence to sliding state of the whole surface, the friction coefficient stabilises itself reaching a steady value of 0.125, like in the experimental test (Figure 5-8(a)).

Decreasing the imposed driving velocity, both experimentally and numerically, the macroscopic behaviour changes completely its pattern (Figure 5-8(b) and Figure 5-8(e)). The drops of the tangential force along the time

produce periodic fluctuations in the macroscopic friction curve, as shown in the Figure 5-8 for an imposed velocity of 1 mm/s. Continuing to decrease the imposed velocity for values lower than 1 mm/s and maintaining fixed the average normal pressure, the response of the system doesn't change its pattern: the macroscopic contact scenarios is always characterized by macro stick-slip phenomena (Figure 5-8(c) and Figure 5-8(f)). However the Figure 5-8(c) and Figure 5-8(f) show that, both numerically and experimentally, the amplitude of the drops of the macroscopic friction and the time period of stick-slip events increase when the imposed velocity is reduced.

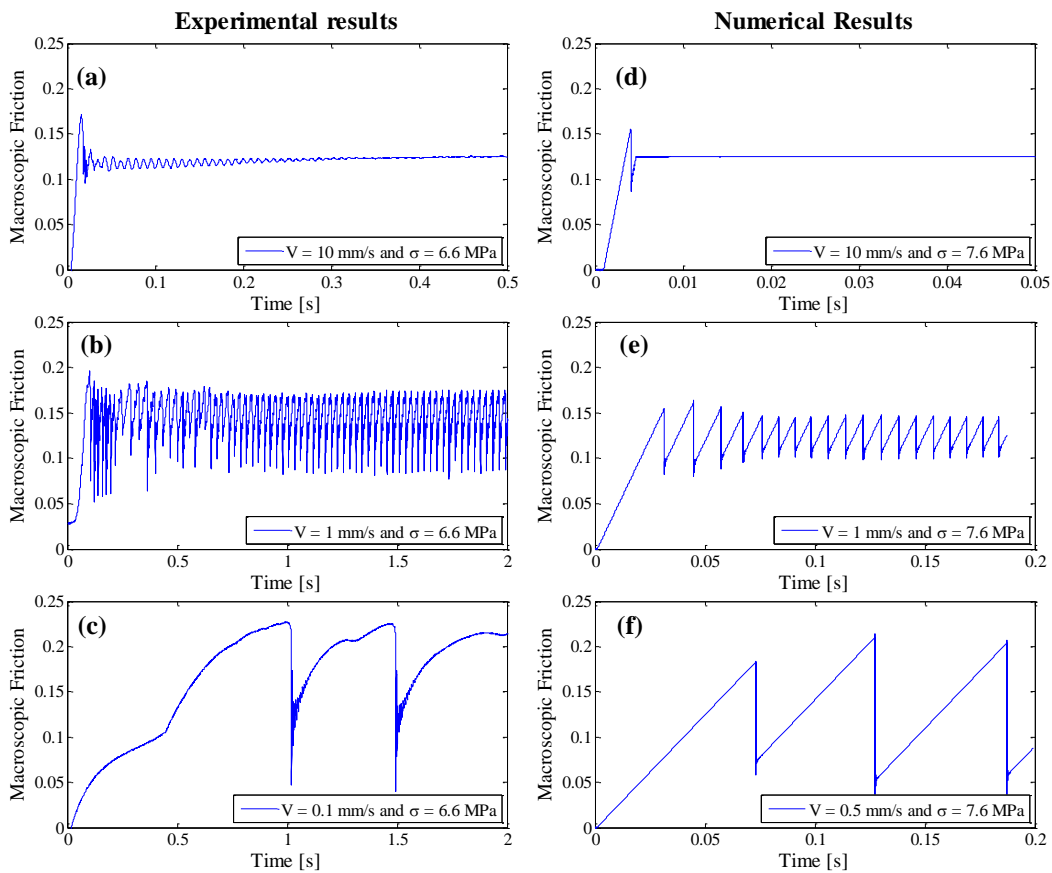


Figure 5-8: Comparison between experimental and numerical results on transition from stable continuous sliding to macroscopic stick-slip instability as a function of imposed driving velocity V . (a)-(b)-(c) Experimental results ranging the imposed velocity between 10 mm/s to 0.1 mm/s and average contact pressure of 6.6 MPa. (d)-(e)-(f) Numerical results ranging the imposed velocity between 10 mm/s to 0.5 mm/s and average contact pressure of 7.6 MPa.

Figure 5-9 shows the main effect into defining the macroscopic response of the frictional system when the normal force (average contact pressure) is varied between 3 MPa to 6.6 MPa for the experimental tests and between 3.5 MPa to

7.6 MPa for the numerical simulations, while the driving velocity is maintained fixed. For low contact pressure the system is characterized by a stable continuous sliding; the friction coefficient increases reaching the constant value of 0.20 with not relevant oscillations of the system (Figure 5-9(a) and Figure 5-9(d)). On the other hand, increasing the contact pressure, the system (numerically and experimentally) switches from stable sliding to macro-stick slip instability, showing subsequent drops in the macroscopic friction coefficient along the time.

For both experimental and numerical results, when increasing further the contact pressure, the amplitude of the drops in the friction coefficient increases reaching a lower limit of macroscopic friction coefficient around 0.05, due to the important released of elastic energy stored during the tangential (stick) ramp.

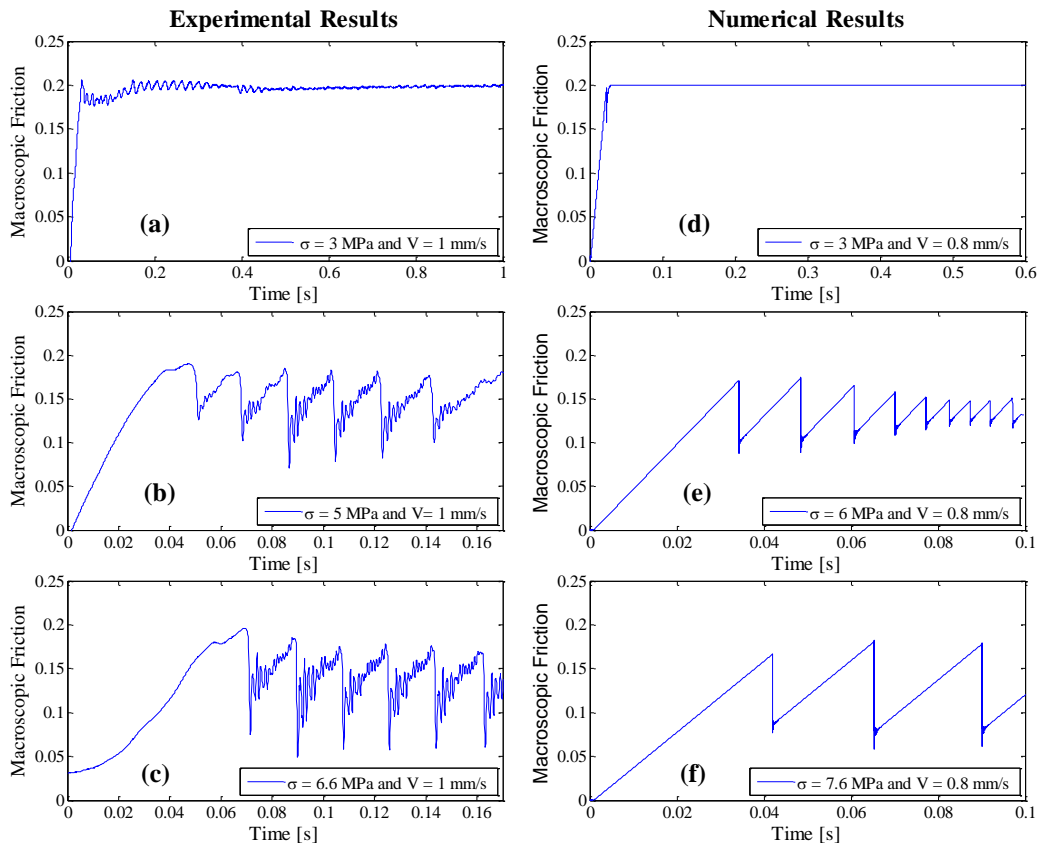


Figure 5-9: Comparison between experimental and numerical results on transition from stable continuous sliding to macroscopic stick-slip instability as a function of average contact pressure. (a)-(b)-(c) Experimental results ranging the average contact pressure between 3 MPa and 6.6 MPa and impose velocity of 1 mm/s. (d)-(e)-(f) Experimental results ranging the average contact pressure between 3.5 MPa and 7.6 MPa and imposed velocity of 0.8 mm/s

It should be noticed that the decaying vibrations excited experimentally after each force drop present low frequency components (mainly at about 110 Hz) due to the dynamic response of the modes of the whole experimental set-up, as observed in the section 5.3; in the numerical curves only decaying oscillations at higher frequencies can be observed and are related to the dynamic response of the modes of vibration of the two blocks of polycarbonate.

Similarly, the differences in term of amplitude and period of stick-slip events between experimental and numerical tests are due to the fact that the numerical model simulates the dynamics of two polycarbonate blocks without accounting for the tangential stiffness and dynamics of the whole experimental set-up. The experimental setup is composed by auxiliary parts that can't allow for defining a quantitative comparison between experimental and numerical results.

The main differences, due to the lack in modelling of the whole set-up, is the different tangential stiffness of the numerical and experimental systems, which brings to a different slope of the tangential force and consequently to different values of the time period between successive stick-slip events.

Another not negligible difference is the presence of the set-up modes at lower frequencies that brings to the low frequency oscillations recorded in the experimental test and not observable in the numerical curves.

Nevertheless, the effect of the imposed boundary conditions recovered by means of the numerical simulations, exhibits a good qualitative agreement with the experimental results. The experimental transition from stable continuous sliding to macroscopic stick-slip for the polycarbonate blocks has been obtained for the same trend of the boundary conditions.

The performed simulations allowed to draw a numerical map of possible contact scenarios (Figure 5-10), showing the good qualitative agreement with the experimental map in Figure 5-5. The missing of the mode coupling instabilities in the numerical map is due to the missing of the unstable mode of the whole set-up at 110 Hz. In fact, the complex eigenvalue analysis [24] of the numerical model of the polycarbonate blocks alone doesn't predict unstable system modes. The unstable mode recovered experimentally (see section 3.2) is a low frequency mode of the set-up, which is not modelled in the numerical analysis.

The numerical maps of the instability scenarios can give just the trend of the frictional scenarios as a function of the system parameters; as showed in the previous Chapter, accounting for the material damping, the effect of all the system parameters are deeply interdependent and the boundary of these maps, calculated for a given system configuration, can vary as a function of the other system parameters.

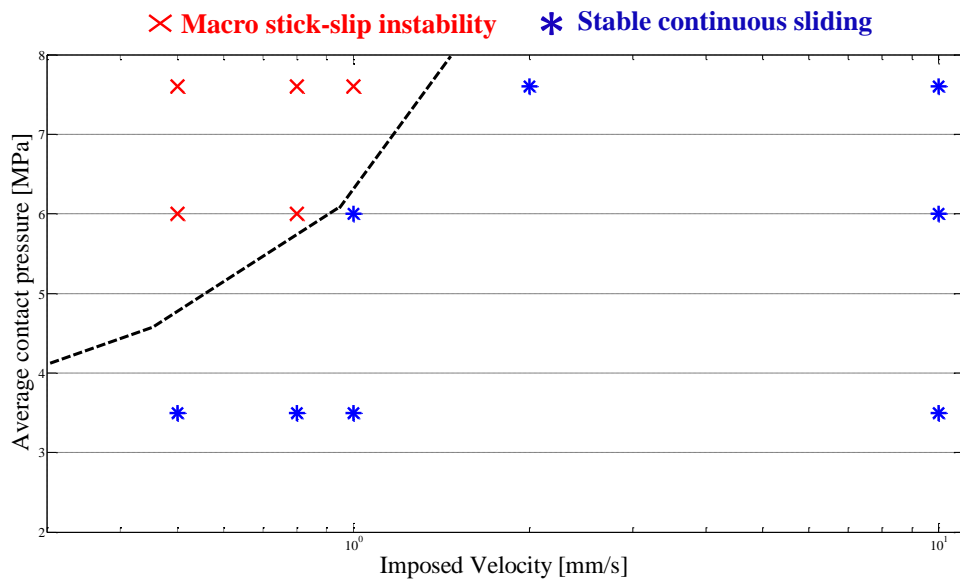


Figure 5-10: Numerical map of the frictional contact scenarios as a function of the imposed driving velocity and average contact pressure.

5.5 Discussion of results

Frictional scenarios of two elastic media in relative displacement have been investigated both by experimental tests and numerical simulations. The same system with respect to different boundary conditions, such as imposed velocity or average contact pressure, switches its macroscopic frictional behaviour from macroscopic stick-slip instability to mode coupling instability with harmonic vibrations, up to stable continuous sliding. A frictional scenario map, found numerically as a function of the material damping in [24], has been here drawn experimentally and numerically as a function of the applied boundary conditions.

The mode coupling contact instability, investigated mostly in brake squeal, has been reproduced here for two general elastic bodies in frictional relative motion.

From the experimental data obtained by frictional tests on polycarbonate, an appropriate friction law with adherence time dependence has been defined. Non-linear transient simulations highlighted the same experimental transition range from stable sliding to macroscopic stick-slip as a function of the key parameters.

Even if the qualitative comparison is obtained, the set-up stiffness and dynamics, not included into the numerical model, doesn't allow for a quantitative comparison. In the next Chapter the experimental tests have been

reproduced on the newer dedicated set-up, TRIBOWAVE, and the set-up tangential stiffness has been included into the model, in order to allow for a quantitative comparison.

6 Analysis of macroscopic frictional scenarios on a dedicated setup

6.1 Introduction

While the preliminary experimental campaign allowed for recovering qualitatively the different frictional scenarios highlighted numerically, a finer experimental analysis is needed to investigate the coupling between the system and contact dynamics and provide a quantitative comparison with the numerical simulations.

At this aim the newer set-up TRIBOWAVE, described in Chapter 2, has been developed. This set-up allowed for reproducing and analysing the different macroscopic frictional behaviours and their occurrence as a function of a larger and more controlled range of boundary conditions. The stiffness and the dynamics of the set-up has been measured as well and included into the numerical model. In fact, because the shift between different macroscopic frictional scenarios is a function of the coupling between the contact and system dynamics, the experimental test bench have to provide access to both the local (contact) and system behaviour.

The development of the TRIBOWAVE set-up and the updating of the numerical model, including the set-up stiffness and dynamics, allowed to develop a quantitative comparison between the experimental and numerical results, as detailed in this chapter.

The numerical results can be then used to associate each macroscopic frictional response of the system to the local behaviour at the contact (rupture and contact wave propagation, stick-slip-detachment distribution and evolution at the interface), which is still not possible to be investigated experimentally.

Moreover, the accessibility to the contact by optical and acoustic instrumentations will allows for future analyses of the rupture and wave propagation at the contact to validate the results of the numerical simulations at the contact region.

6.2 Experimental observations

6.2.1 Materials and method

Blocks of polycarbonate (PC) and blocks of polymethyl-methacrylate (PMMA) have been used to carry out the experiments on the setup TRIBOWAVE. The material and geometrical properties of the specimens, used in the experimental analysis, are reported in the following table:

	Polycarbonate	PMMA
Length [mm]	30	30
Width [mm]	10	10
Thickness [mm]	10	10
Density [kg/m³]	1200	1190
Young Modulus [GPa]	2.5	3.3
Poisson coefficient	0.4	0.37

Table 5: Material and geometrical properties of the samples in contact.

The dimensions of the specimens (Table 5) are relatively small in order to optimize the planarity of the two contact surfaces and to reach large ranges of the contact pressure.

To obtain reproducibility of the results, the contact surface of the samples has been polished and then cleaned before performing each test. The following procedure has been adopted:

- First, each contact surface has been polished with a SiC paper (size #1000) for wet grinding of materials, obtaining a random roughness of contact surface and avoiding preferential direction of the roughness.
- Then the ultrasonic cleaning process is applied to the specimens. The intention is to remove all traces of contamination tightly adhering or embedded onto solid surfaces using ultrasounds and an appropriate cleaning solvent. Distilled water has been used as solvent, avoiding further contamination of the contact surface of the samples.
- Finally the samples are put in a vacuum dryer machine with appropriate salt in order to remove the water absorbed superficially.

The explained procedure led to have a contact surface of the sample with controlled mean roughness properties as shown in Figure 6-1 in the case of a block of polycarbonate.

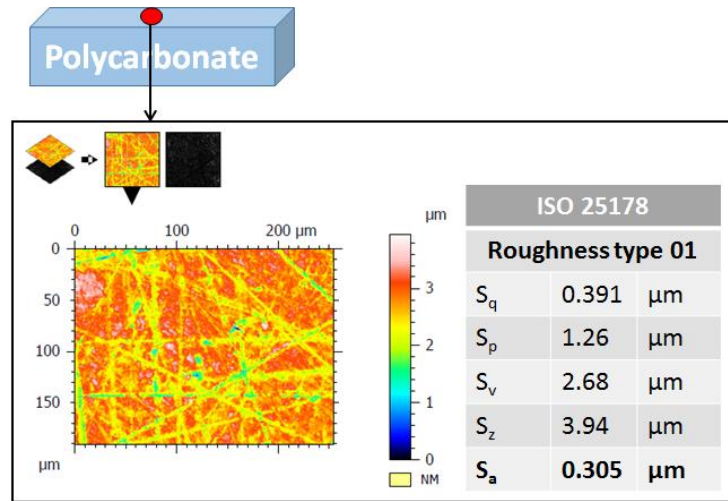


Figure 6-1: Reference properties of the roughness of the contact sample surface used in the experimental analysis for polycarbonate blocks.

The lower specimen is fixed to the mobile part of the set-up and the translation displacement is imposed by means of the electromagnetic motors, controlled in position as explained in the section 3.3. The upper specimen is bonded to the fixed support of the experimental setup. In order to characterize the contact frictional behaviour of the two elastic bodies in relative motion, the tangential force (force along x direction), the normal force (force along y direction), the imposed displacement, the acceleration of the mobile and fixed part and the acceleration of the whole assembly have been recorded during each experiment. The friction and contact forces have been recorded both in the preload phase and during the relative motion. The imposed displacement has been measured by the linear encoder, while piezoelectric accelerometers record the acceleration of the system within a bandwidth of 15 kHz. In order to also investigate the dynamic response on the samples in contact, the velocity of one point of the fixed sample has been recorded, as close as possible to the contact surface, with a sample frequency of 100 kHz. The velocity signal allows for capturing the local dynamics that come from the contact interface. Figure 6-2 shows the position of the point close to the contact interface, where the velocity is measured.

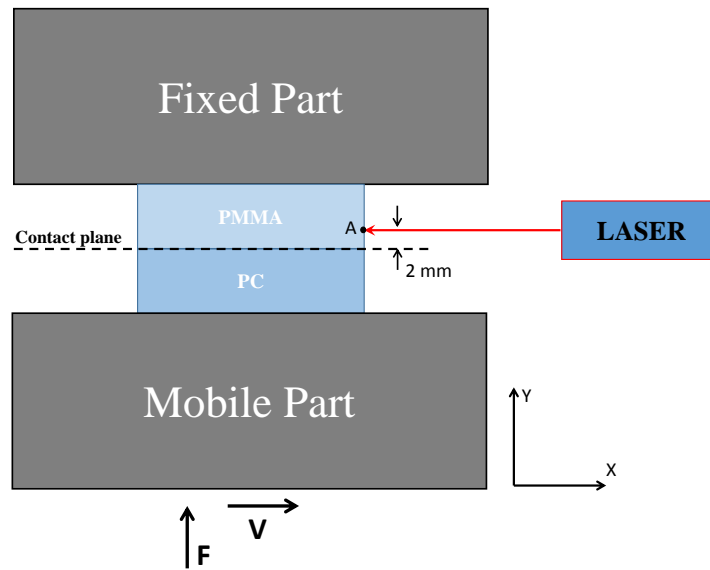


Figure 6-2: Basic scheme of the measure of the velocity of the one point (A) of the fixed sample with the vibrometer laser.

Each experimental test has been performed applying in the first phase the compressive normal force F in order to obtain a desired initial average contact pressure; then, in the second phase, a constant velocity (linear displacement) is imposed in the x direction on the lower sample to bring the specimens in frictional relative motion.

The monitored signals have been recorded with a sampling frequency of 50 kHz by an OROS acquisition system, except for the local velocity signal (vibrometer laser) that has been recorded with a sample frequency of 100 kHz; this in order to investigate the dynamics of the samples, which is characterized by high natural frequencies due to the small dimensions of the considered specimens.

6.2.2 Frictional scenario maps

The experimental analysis on the dedicated setup (TRIBOWAVE) has been performed considering contact samples constituted by both similar materials (PMMA-PMMA) and dissimilar ones (PMMA-PC). For each pair of contact material a parametrical analysis has been carried out as a function of normal load and imposed driving velocity. The initial normal load has been varied between three different values: 900 N, 1500 N and 2000 N; the considered values of the normal load led to have an initial average pressure at the contact interface of 3 MPa, 5 MPa and 6.6 MPa respectively. On the other hand the horizontal driving velocity has been varied from 10 $\mu\text{m/s}$ up to 10 mm/s, with a maximum horizontal displacement of 5 mm.

The performed tests allowed for drawing for each pair of materials in contact a frictional scenario map as a function of the boundary conditions. Figure 6-3 shows the frictional scenario map related to PMMA-PC contact samples. In Figure 6-3 and Figure 6-4 the red crosses represent a frictional system which is dominated by macroscopic stick-slip instability, the green points a frictional system characterized by continuous sliding with mode coupling instability and the blue stars a frictional system in stable continuous sliding. The same mechanical system exhibits different macroscopic frictional behaviours varying only the imposed boundary conditions. As a consequence the macroscopic friction coefficient depends from the imposed boundary conditions too. The Figure 6-3 and Figure 6-4 highlight that, for the investigated system and materials, the imposed driving velocity influences mostly the frictional response of the system.

In the case of PMMA-PC contact materials (Figure 6-3), for low driving velocity ($V < 2$ mm/s) the system dynamic is dominated by macroscopic stick-slip instability; otherwise for higher driving velocity ($V > 2$ mm/s) the system is characterized by continuous sliding with or without mode coupling instability. The variation of the average contact pressure doesn't influence the switching from a stable to unstable frictional scenario; in fact increasing the average contact pressure from 3 MPa up to 6.6 MPa and for low driving velocity ($V < 2$ mm/s) the system is always characterized by macroscopic stick-slip. The apparition of the mode coupling instability during continuous sliding is affected by the applied load; one of the possible explanations is the varying of the system dynamics with the applied load.

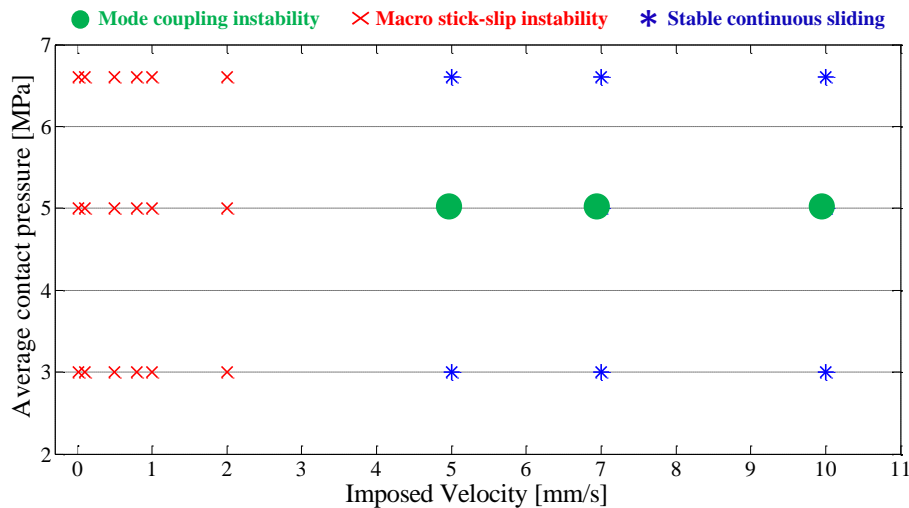


Figure 6-3: Experimental map of the frictional contact scenarios as a function of the imposed driving velocity and average contact pressure for PMMA-PC contact samples.

The Figure 6-4 related to PMMA-PMMA contact samples shows a similar pattern as the map in Figure 6-3. For low driving velocities macroscopic stick-slip characterises the system response; otherwise for high driving velocity a continuous sliding with unstable vibrations due to the mode coupling instability governs the system response. The comparison of the two maps in Figure 6-3 and Figure 6-4 highlights a greater propensity to the mode coupling instability for the PMMA-PMMA respect to PMMA-PC contact materials.

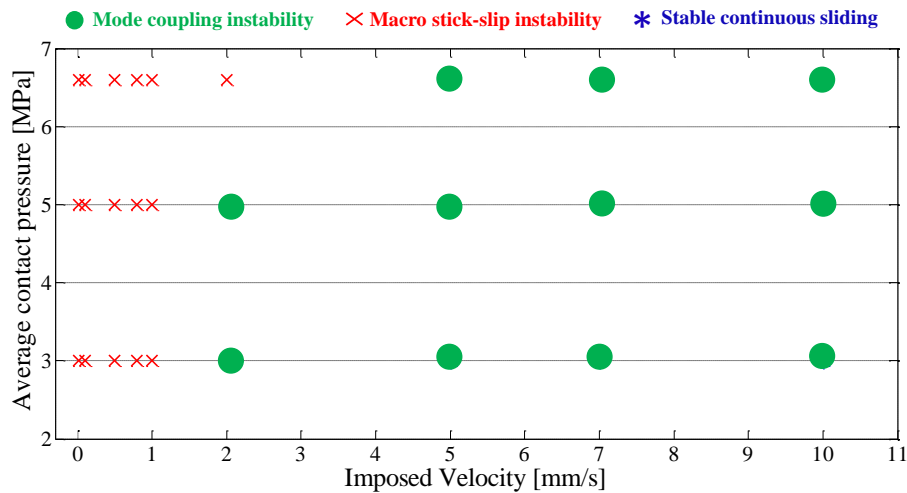


Figure 6-4: Experimental map of the frictional contact scenarios as a function of the imposed driving velocity and average contact pressure for PMMA-PMMA contact samples.

In order to better understand the difference propensity to mode coupling instability the macroscopic friction coefficient (Figure 6-5) has been recovered for the two different contact material pairs with the same imposed boundary conditions. Figure 6-5 shows that the mean value of the macroscopic friction coefficient in the case of PMMA-PMMA contact samples is higher than PMMA-PC contact samples. In general, numerical and experimental works [30, 42, 78] highlighted as a higher friction coefficient certainly plays a key role into the propensity on the mode coupling instability. However different key factors are involved simultaneously on the occurring of the mode coupling instability, so that an exact separation of each effects is often difficult.

A more detailed analysis of frictional instabilities both related to macroscopic stick-slip and mode coupling instability is presented in the next sections, focusing the attention to the contact sample dynamics.

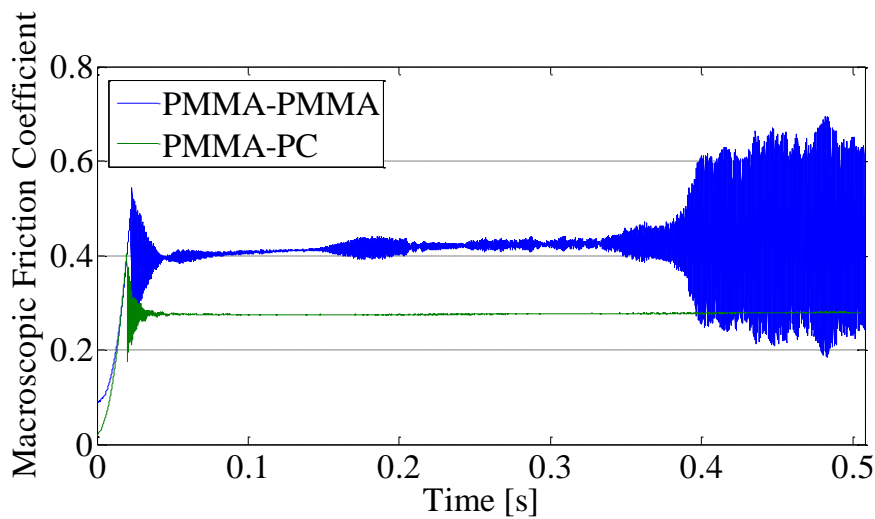


Figure 6-5: Macroscopic friction coefficient (ratio between global tangential force and global normal force) for different contact material pairs, obtained with the following boundary conditions: imposed driving velocity 10 mm/s and initial normal load 900 N (3 MPa).

6.2.3 Frictional instabilities: discussion on the system dynamic response

This section presents the experimental results carried out with PMMA-PC contact samples. The more relevant cases of the frictional instabilities are presented: macroscopic stick-slip and mode coupling instability. The frequency and time analysis is presented focusing the attention to the response of the sample and the setup dynamics during the frictional instabilities.

Macroscopic stick-slip

A typical macroscopic scenario with stick-slip instability has been reproduced with PMMA-PC materials in contact. Figure 6-6 shows the system frictional response for an imposed driving velocity of 10 $\mu\text{m/s}$ and normal contact force of 1500 N (5 MPa). The black curve represents the imposed displacement in order to obtain a constant translational velocity along the x direction. The blue and green curves show respectively the tangential and normal global forces recorded by the force transducer. The red curve shows the velocity of a point of the upper sample, as close as possible to the contact interface, measured by the laser vibrometer along the direction of the relative motion.

First, a normal force along the y direction is applied to the system in order to obtain an initial average normal pressure of 5 MPa. After this preload phase (not

reported in Figure 6-6) the constant velocity is imposed to the lower boundary of the body 2.

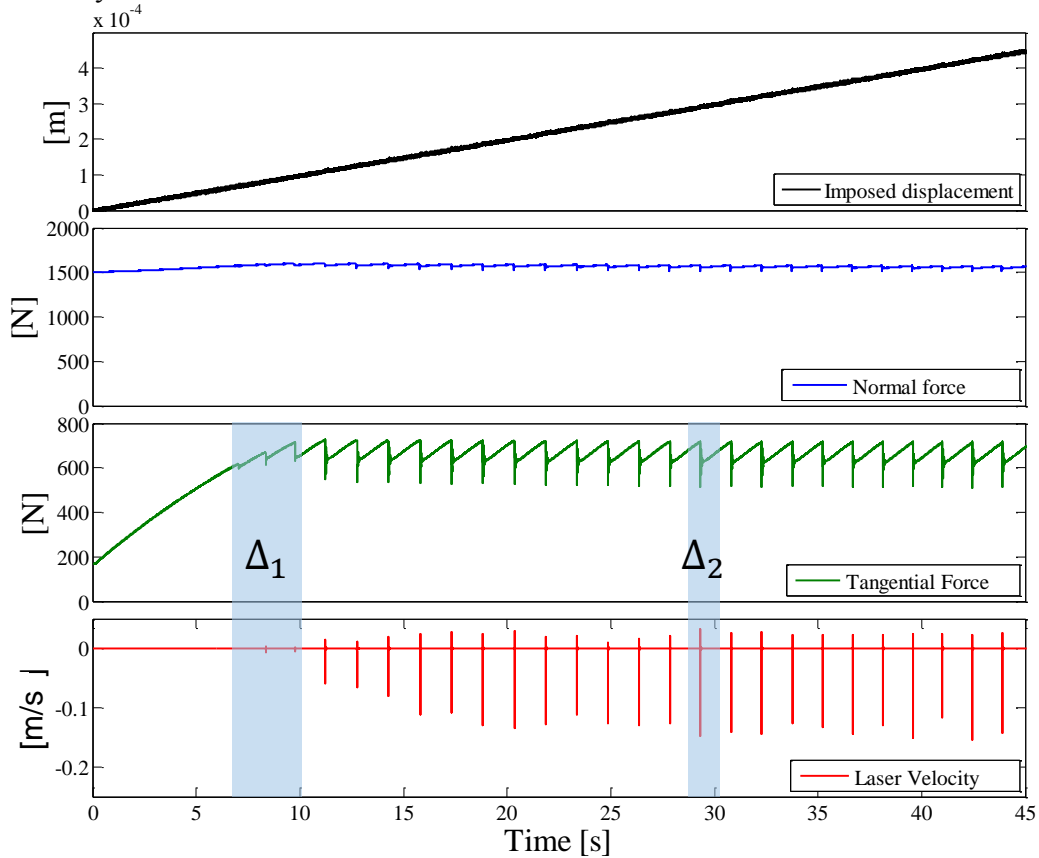


Figure 6-6: Macroscopic stick-slip instability for PMMA-PC contact samples. From top to bottom: Imposed displacement; normal (y direction) force and tangential (x direction) force; laser velocity. Experimental data obtained with the following parameters: imposed driving velocity $10 \mu\text{m/s}$ and average normal load 1500 N (5 MPa).

The tangential force exhibits periodic drops along the time. The period of the force drops represents the period of the macroscopic stick-slip of the system. Each force drop excites the system dynamics with oscillations that are then damped during the ramp (stick) phase. It is interesting to note that the pattern of the tangential force during the first tangential ramp ($5\text{s} < t < 10\text{s}$) is characterized by repetitive force drops of small amplitude (Figure 6-7) until the tangential force reaches the maximum value (around 700 N). Figure 6-7 shows the tangential force and the laser velocity for the time interval Δ_1 , allowing for distinguish the contributions of the whole set-up dynamics and sample dynamics respectively.

In the time interval Δ_1 the tangential force exhibits three force drops with consequent released of the accumulated elastic energy. The normalized spectrum

(FFT) of each signal in the time interval Δ_3 is reported in the Figure 6-7. Each force drop represents an impulsive excitation of the whole sample dynamics as shown from the spectrum of the velocity signal in Figure 6-7. The tangential force drops before the first macro-slip event represents a sort of “precursors”, investigated numerically and experimentally in recent works [19, 20, 62]. The precursors are associated with a rupture propagation at the interface characterized by an energy content not sufficient to bring the whole surface in sliding condition. Nevertheless, a small part of the stored elastic energy is released during each force drop causing an excitation of the global dynamics of the setup and the sample dynamics. In fact the FFT (Fast Fourier Transform) calculated in the time interval Δ_3 (Figure 6-7) of the tangential force and the velocity signal shows a main frequency peak at around 1200 Hz related to the tangential mode of the whole setup. Moreover the FFT of the velocity signal shows also as the first natural frequencies (21, 32, 34, 41, 43 kHz) of the samples in contact are excited after the rupture propagation (precursors).

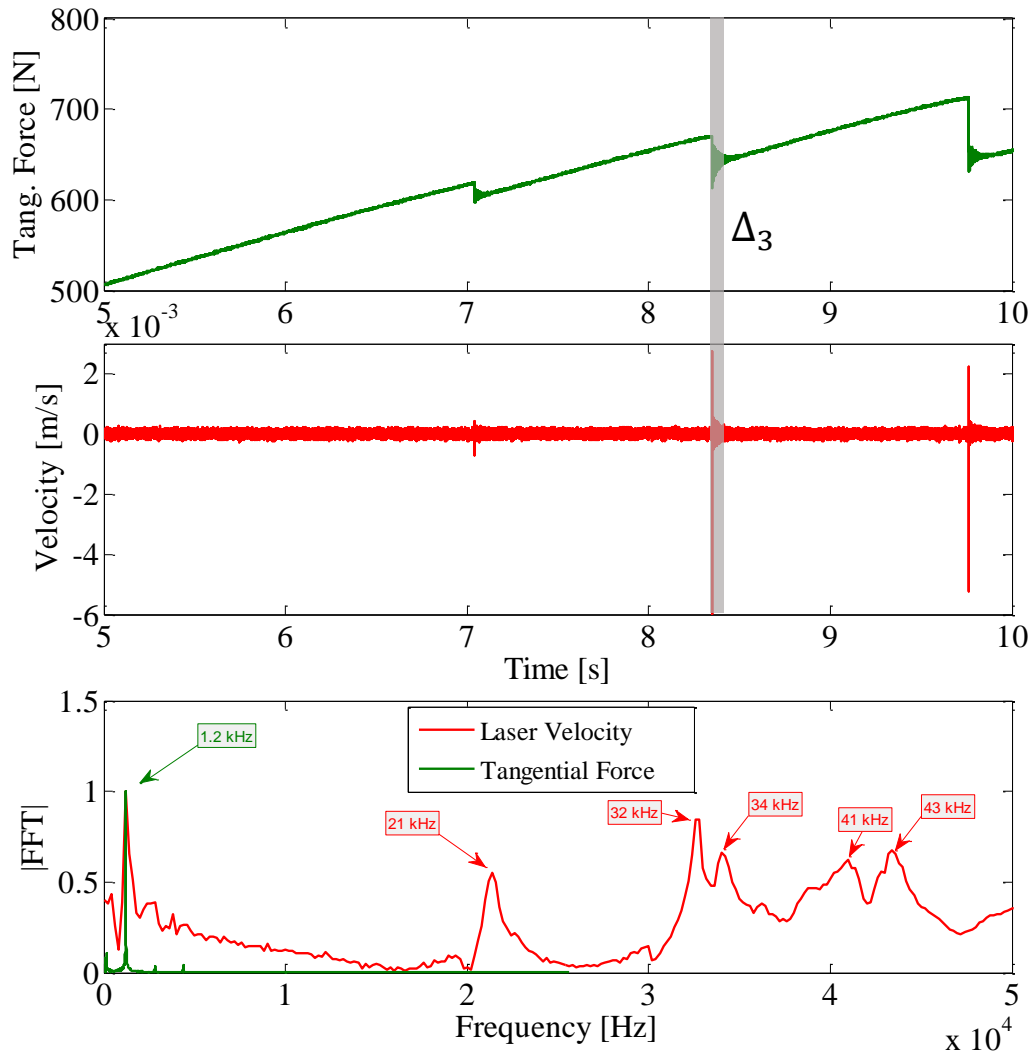


Figure 6-7: Plot (interval Δ_1 of the Figure 6-6) of the tangential force (a) and laser velocity (b) for the following parameters: imposed driving velocity $10 \mu\text{m/s}$ and average normal load 1500 N (5 MPa). Normalized FFT of the tangential and laser velocity (c) computed in the interval Δ_3 . The normalization of the FFT respect to the maximum value for each signal allows for a direct comparison between the two recorded signals.

After this first ramp due to the tangential loading phase, the curve of the tangential force (Figure 5-1) exhibits periodic drops and subsequent ramps along the recorded time. Each increase of the tangential force (increase of elastic energy stored in the system) is followed by a sudden drop due to the following macro-slip event (rupture and wave propagations) at the contact surface [17]. Figure 6-8 shows the signal of tangential force and the signal of laser velocity in the time interval Δ_2 . The locus plot (Figure 6-8) shows an impulsive excitation (velocity signal) with the consequent tangential force drop ($t=29.3327\text{s}$) when

the macro-slip event is reached. The rupture propagation at the interface, highlighted by the impulse on the signal of the velocity recorded at the border of the contact, leads to the consequent macroscopic slip of the frictional system [17, 88].

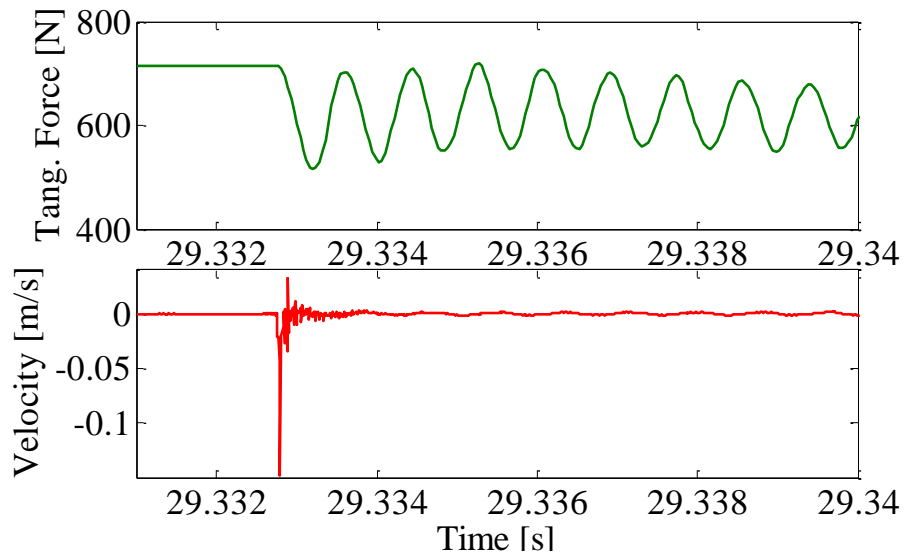


Figure 6-8: Locus plot (interval Δ_2 of the Figure 6-6) of the tangential force and laser velocity for the following parameters: imposed driving velocity 10 $\mu\text{m/s}$ and average normal load 1500 N (5 MPa).

After the occurrence of the macro-slip event, the natural frequency of the contact samples are excited, as shown by the time-varying spectrum of the laser velocity in Figure 6-9(a); after that, the oscillations related to the sample dynamics are quickly damped and the oscillations at low frequency (1200 Hz) characterises the system response, as shown in the time-varying normalized spectrum in Figure 6-9(b).

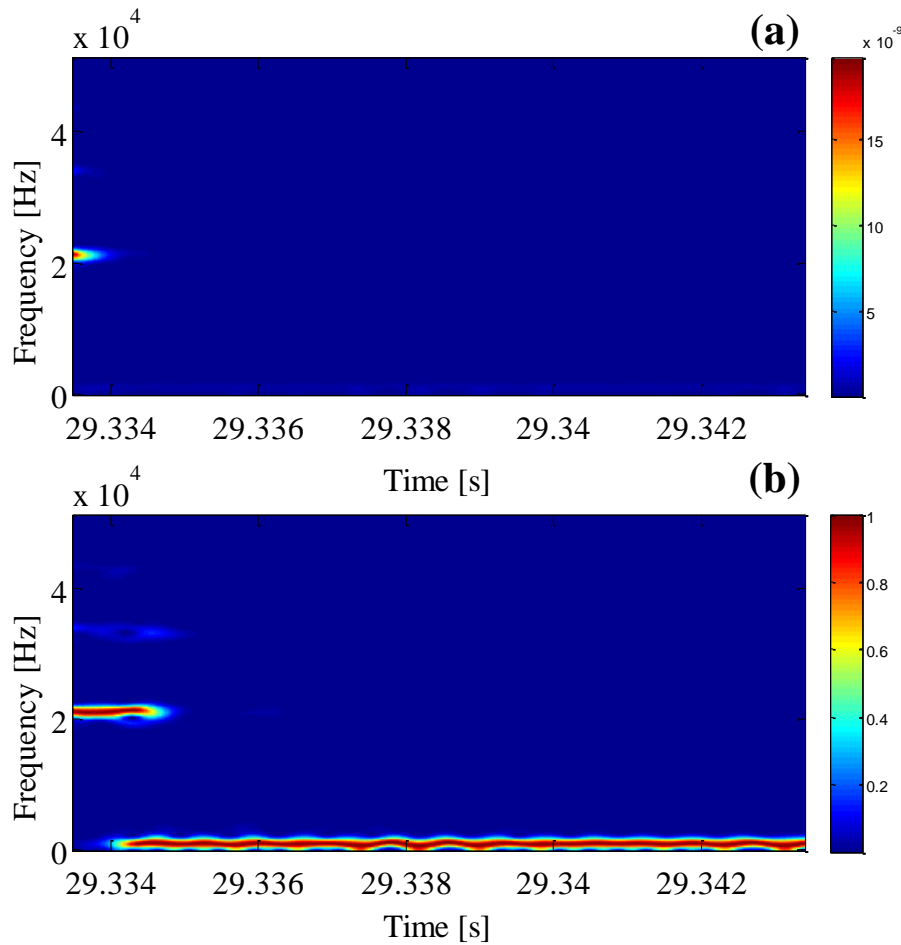


Figure 6-9: Time-varying spectrum (up) of the laser velocity signal for t . Normalized time-varying spectrum (down) respect to the maximum value at each time period in order to highlight the main frequencies involved after the macro-slip event.

Mode coupling instability

Increasing the driving velocity and maintaining fixed the normal force (1500 N), the macroscopic frictional behaviour changes its pattern. Figure 6-10 shows the system behaviour for an imposed translational velocity of 10 mm/s. After the preload phase, the translational velocity is imposed and the tangential force (green curve in Figure 6-10) reaches its maximum value, higher than the mean tangential force at steady state. Then, after the first macroscopic slip, the system shows oscillations of the global frictional force around its mean constant value (green curve in Figure 6-10). Furthermore the recorded tangential force highlights the typical behaviour of mode coupling instability: a first phase with an initial exponential increasing of oscillations followed by a second phase where the response is bounded to a limit cycle. Two different exponential

increases of the oscillations can be observed successively at 0.05s and 0.3s, resulting in two limit cycles with a different amplitude.

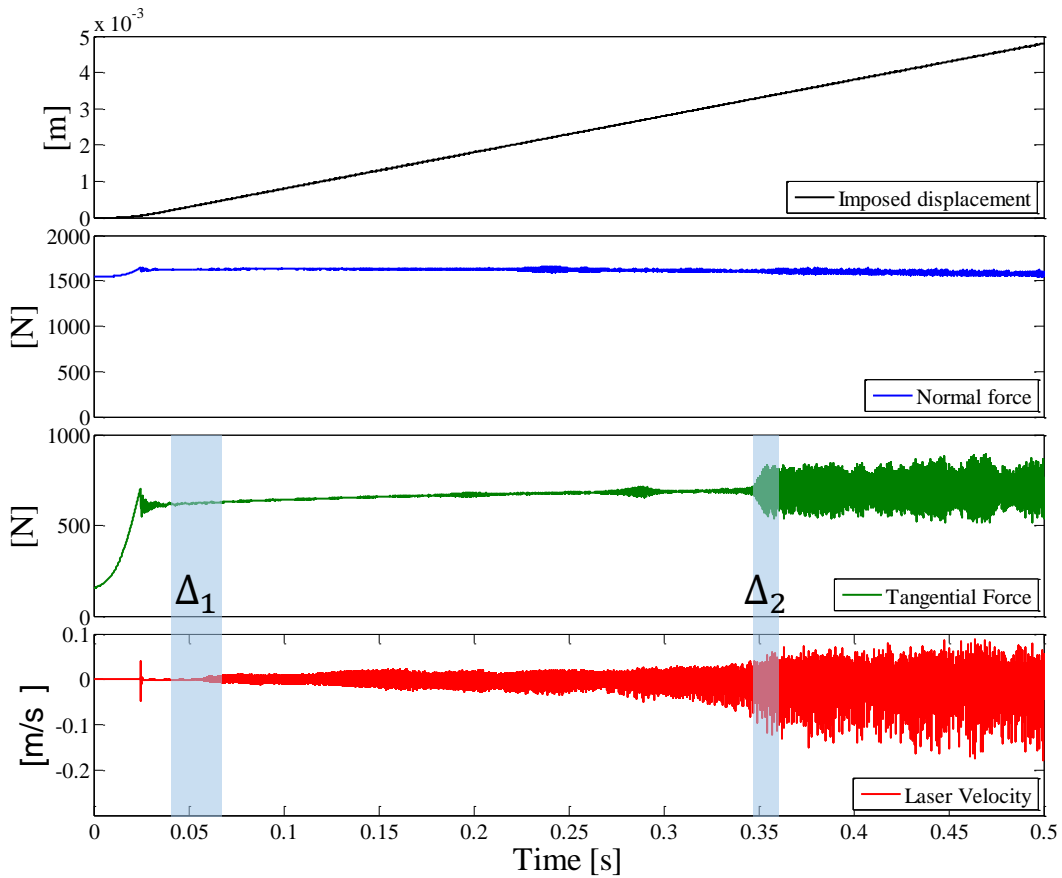


Figure 6-10: Mode coupling instability for PMMA-PC contact samples. From top to bottom: Imposed displacement; normal (y direction) force and tangential (x direction) force; laser velocity. Experimental data obtained with the following parameters: imposed driving velocity 10 mm/s and average normal load 1500 N (5 MPa).

Looking at the recorded signals in the time interval Δ_1 of the Figure 6-11, a pattern of the signals characteristic of mode coupling instability is observed. While the tangential force show low amplitude oscillations in time (Figure 6-10), the laser velocity increases the amplitude of oscillations during the time as shown in Figure 6-11.

The time-varying spectrum and the FFT of the signal velocity in the time interval Δ_1 show as the frequency content of the velocity signal is characterized by a main harmonic at 22 kHz and the respective super/sub-harmonics, due to the contact non-linearities. A spectrum characterized by harmonic vibrations as in Figure 6-11 is characteristic of mode coupling instability induced by the

frictional contact forces. In this case the high frequency oscillations (22 kHz) are mainly related to an unstable mode of the contact samples. For this reason the oscillation of the contact forces, measured away from the contact and averaging the response due to the deformation of the samples, shows relative low amplitude of the oscillation.

This kind of frictional instabilities, related to the unstable mode of the contact samples, has been explained in details in the chapter 4.

The experimental results highlighted as the frictional forces can excite different unstable modes of the system. Each excited unstable mode (low and high frequency) characterises differently the local contact behaviour and the coupling with the vibrational system response.

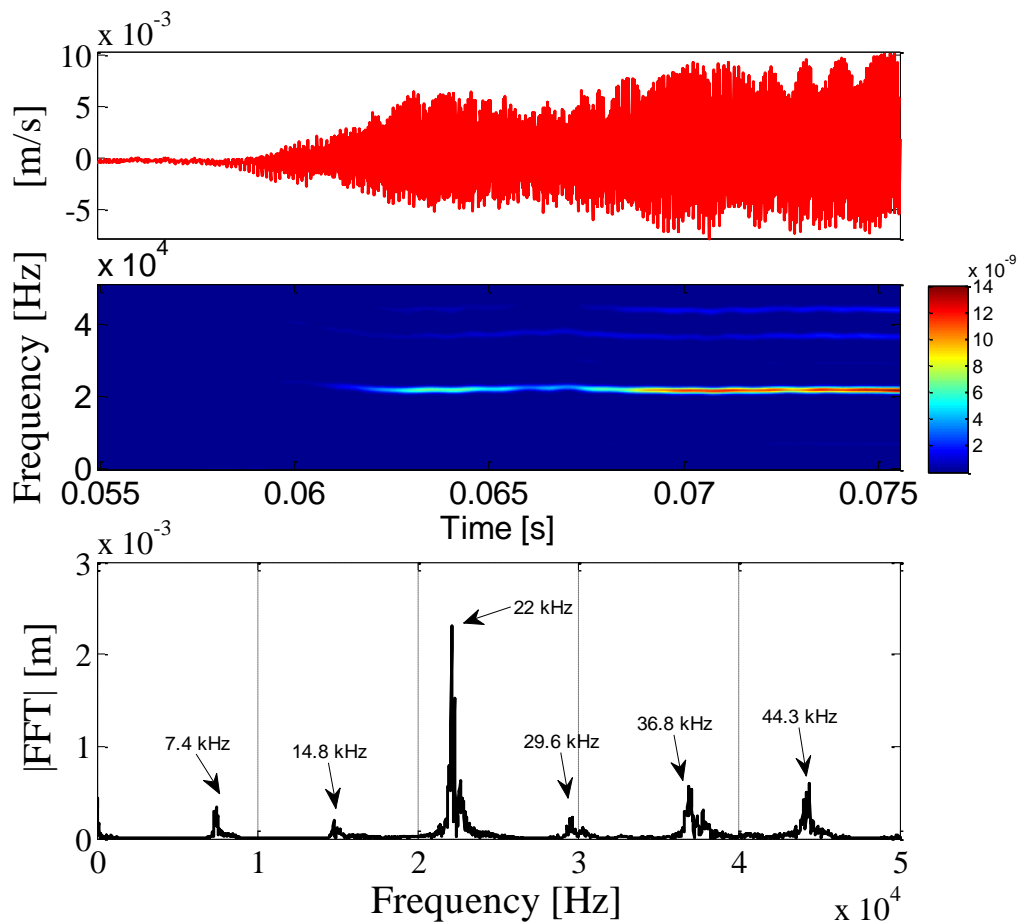


Figure 6-11: (Up) Plot (interval Δ_1 of the Figure 6-10) of the laser velocity and time-varying spectrum of the velocity; (Down) FFT of the velocity signal calculated in the same time interval.

The plot of the tangential force and the laser velocity during the limit cycle (time interval Δ_2) is shown in Figure 6-12. The recorded tangential force during

the limit cycle exhibits harmonic oscillation at 1200 Hz (see Figure 6-12); the relatively low frequency of the oscillation is associated to the tangential mode of the whole experimental setup. In this case the tangential mode can be considered unstable causing strong vibrations in the system response. The comparison between the recorded velocity signal and the tangential force during the time interval Δ_2 highlights the interaction between the contact behaviour and the dynamics of the setup (Figure 6-12). In fact during the limit cycle the low frequency instability guides the relative oscillation between the contact surfaces of the samples, influencing thus the contact behaviour. Figure 6-12 shows as the period of the oscillation of the tangential force (due to the unstable setup dynamics) is equal to the period of the impulses recorded in the velocity signal (sample dynamics). Thus, at each period of vibration, at the unstable mode frequency, a macroscopic slip event occurs between the contact surfaces of the sample. The time-varying spectrum of the laser velocity in Figure 6-12 shows as for each period of tangential force vibration, the response to an impulsive excitation of the contact samples is achieved. A periodic excitation of the sample dynamics (natural frequencies at several kHz), corresponding to the period of the unstable set-up frequency, is shown in the time-varying spectrum in Figure 6-12; in this case the global dynamics of the whole setup guides the rupture generation and propagation at the contact interface (macroscopic slip events).

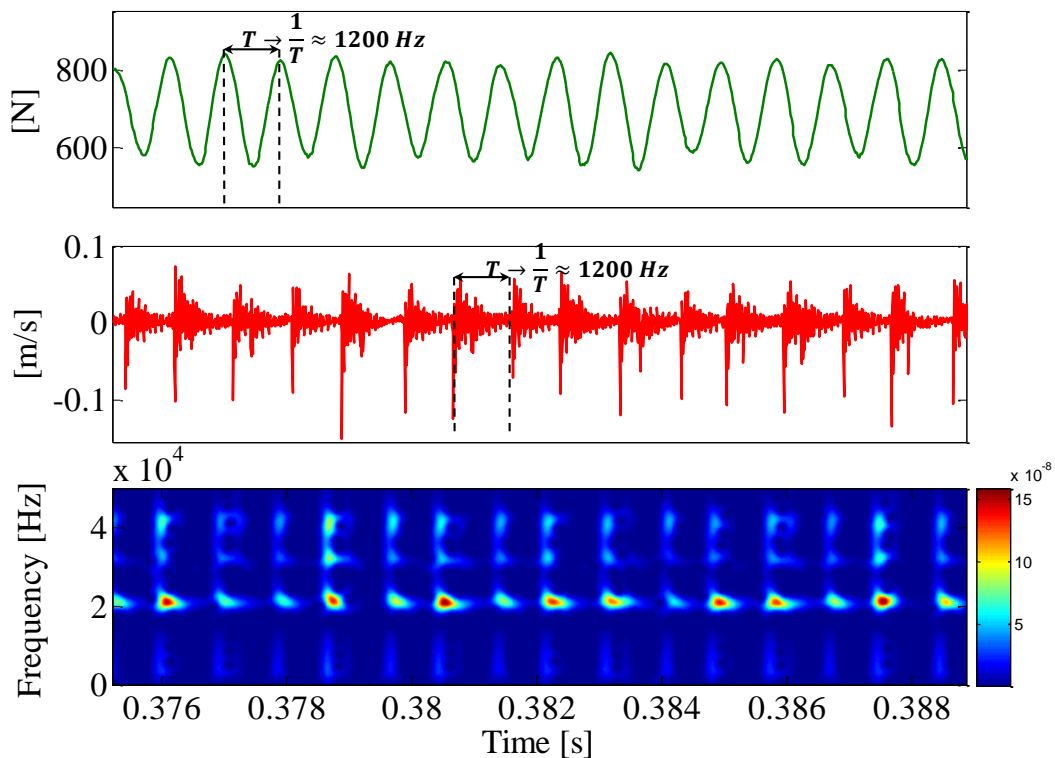


Figure 6-12: Locus plot (interval Δ_2 of the Figure 6-10) of the tangential force, laser velocity and time-varying spectrum for the following parameters: imposed driving velocity $10 \mu\text{m/s}$ and average normal load 1500 N (5 MPa).

6.2.4 Effect of roughness on the friction coefficient

In this section a preliminary analysis of the effect of roughness on the frictional response of the system is presented. An experimental analysis has been performed considering two different roughness of the contact surfaces. One experimental campaign has been carried out considering samples of PMMA-PC with the surface roughness parameters detailed in the section 6.2.1, defined as the reference. On the other hand a second experimental campaign (same materials (PMMA-PC)) with a finer surface roughness has been performed. The properties of the roughness of the contact surfaces used in the experiments are listed in Figure 6-13.

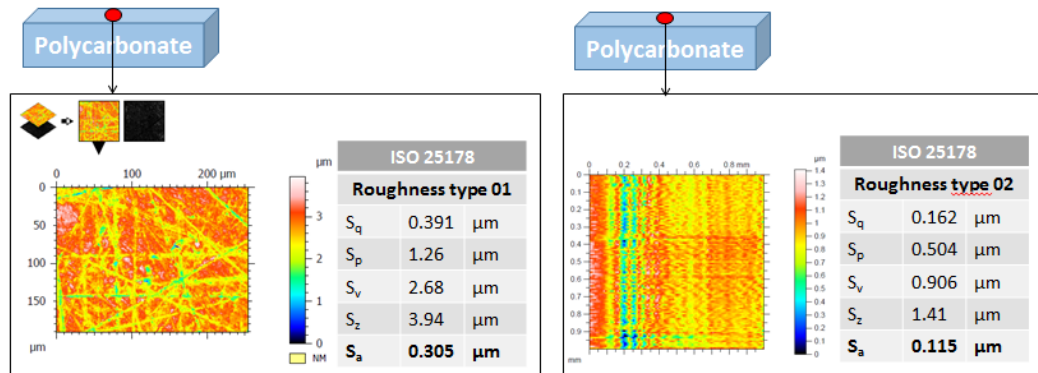


Figure 6-13: Properties of the contact surface roughness used to perform the experimental analysis for polycarbonate blocks.

As in the previous experimental analysis the tests have been performed applying first the compressive normal load and then the driving velocity along the x direction, in order to bring the two samples in relative motion. The imposed velocity has been ranged from $10 \mu\text{m/s}$ up to 15 mm/s , maintaining the normal force at the value of 1500 N (5 MPa at the contact interface). The global response of the system has been recorded for the contact samples with a roughness of type-01 and type-02 (see Figure 6-13) by means of the transducer force. For each value of the imposed driving velocity, a macroscopic friction coefficient as a function of time has been calculated, being the ratio between the recorded global tangential and normal forces. Figure 6-14 shows the macroscopic friction coefficient for different values of the imposed driving velocity. Firstly, the system exhibits a typical behaviour characterized by continuous sliding for $V=15 \text{ mm/s}$ for each roughness type (see Figure

6-14(a)(e)). In particular looking at the Figure 6-14(a)(e) an higher macroscopic dynamic friction coefficient in the case of roughness type-01, respect to roughness type-02, is highlighted for the same driving velocity (15 mm/s). Decreasing the driving velocity the system switches from continuous sliding to macroscopic stick-instability for both the roughness type-01 and type-02. The switch to stick-slip behaviour is obtained at higher velocities for the roughness type-01.

Moreover, Figure 6-14(c)-(h) show how the period of the macroscopic stick-slip is different in the two cases: $T_{01}=1.5$ s and $T_{02}=8.1$ s for driving velocity equal to 0.01 mm/s. In the case of roughness type-02, when the system is characterized by macroscopic stick-slip behaviour, the system reaches an higher value of static friction than in the case of roughness type-01; The same observation can be done for the initial value of the friction coefficient when continuous sliding occurs Figure 6-14(a)-(e). Consequently, during stick-slip, each ramp of the friction coefficient is followed by a larger drop of the friction, which produces a stronger system excitation. In fact the elastic energy stored in the system during each ramp is higher, leading to a larger drop of the friction coefficient as observed in the Figure 6-14(d)(h).

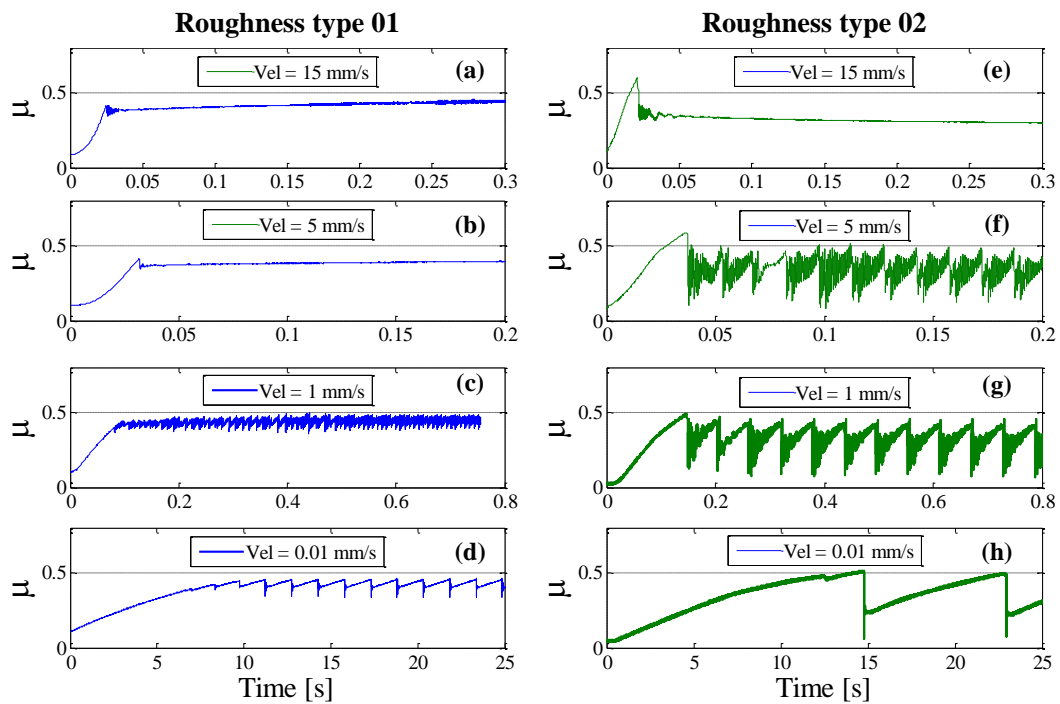


Figure 6-14: Macroscopic friction coefficient as a function of imposed driving velocity for a fixed value of contact force of 1500 N. (left) Experimental results carried out with contact samples of roughness type-01. (right) Experimental results carried out with contact samples of roughness type-02.

The different behaviour of the two roughness samples can be attributed to a higher static friction coefficient and a lower dynamic friction coefficient in the case of roughness type-02 respect to the case of roughness type-01. In fact the estimated curves of macroscopic friction coefficient for each type of roughness (Figure 6-15) shows several differences in term of maximum static friction coefficient and dynamic friction coefficient. For roughness type-01 the maximum static friction coefficient is about 0.51 and the dynamic friction coefficient is about 0.32 (green curve in Figure 6-15); for roughness type-02 the maximum static friction coefficient is about 0.45 and the dynamic friction coefficient is about 0.4 (blue curve in Figure 6-15).

Considering some of the more commonly used friction empirical theories, the friction at the contact interface is often attributed to two mechanisms: adhesion force and deformation force [97, 98]. The first mechanism is mainly due to the different chemical-physical effects at the contact interface; in general the adhesion mechanism is related to the surface energy of the contact materials and in particular a larger real area of contact increases the adhesion contribution to the friction force. The real contact area is smaller than the apparent contact area.

The second mechanism related to the local deformation is a function of the contact asperities of the surfaces. When two roughness surfaces are in contact, the asperities weld each other and thus the macroscopic tangential force is a function of the intersecting asperities. As a consequence of these observations a finer roughness at the contact can increase the static macroscopic friction coefficient, by increasing the real contact area, justifying the larger static friction coefficient for the roughness type-02; on the contrary, the increase of the macroscopic dynamic friction coefficient for the roughness type-01 can be attributed to a larger contribution of component due to the roughness deformation.

It's known that in contact pairs between the polymers the adhesion mechanism is often dominant. The increase of the contact (adherence) time can increase the material adhesion due to both the increasing of the time for physico-chemical activity and the increasing of real contact area under loading conditions.

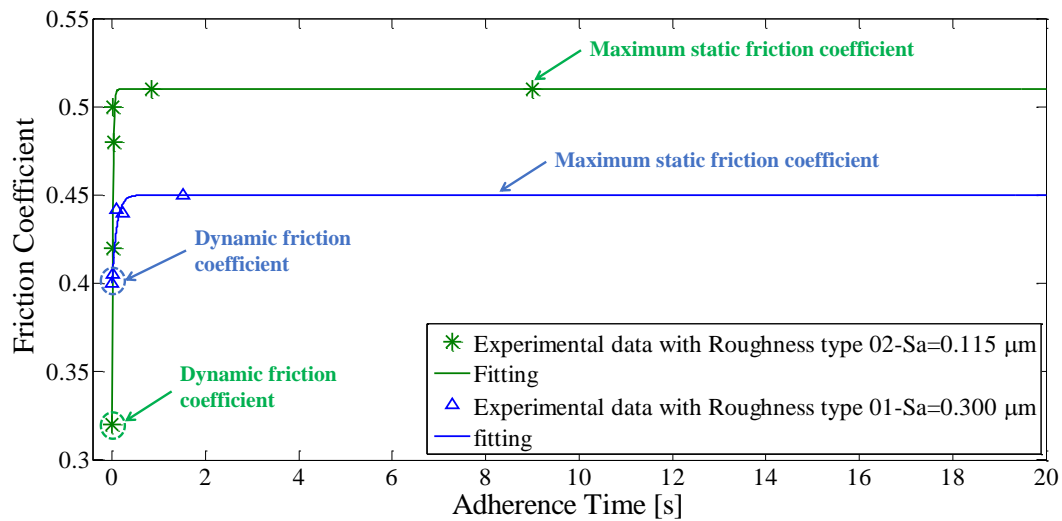


Figure 6-15: Curve fitting of experimental data of macroscopic friction coefficient for normal contact force of 1500 N (5 MPa).

Then, an interpretation of the difference on the measured macroscopic friction coefficient, for the two analysed roughness, can be made considering the nature of friction as explained above. In the case of larger roughness of the contact surfaces the deformation contribution to the friction is dominant; the frictional behaviour is characterized by a higher dynamic friction coefficient and a lower maximum static friction coefficient, which doesn't increase too much as a function of adherence time (blue curve in Figure 6-15).

On the other hand in the case of smaller roughness the adhesion component is dominant; a larger real contact area, combined with a greater propensity of adhesion mechanism for PMMA-PC contact samples, lead to have a larger difference between static and dynamic friction coefficient (green curve in Figure 6-15). The lower amount of asperities in contact and the higher chemical-physical activity of the contact surfaces characterises the contact behaviour leading to a more likely evidence of macroscopic stick-slip instability (Figure 6-14). In addition to this, it has been shown in [50, 68, 78, 99] how the roughness and heterogeneities at the interface can influence the rupture propagation, which is at the origin of macroscopic stick-slip (rupture propagation within the whole interface).

This preliminary investigation of the effect of roughness shows how the contact topography is of great importance into defining the frictional and dynamic response of the system in relative motion.

6.3 Numerical analysis

6.3.1 Description of the numerical model

The numerical model presented in section 2.2 has been updated in order to include the set-up stiffness and dynamics, allowing for a quantitative comparison with the experimental tests. The updated 2D model (plane strain) consists of the two samples separated by the frictional interface governed by the friction contact law presented in section 2.2.3 (friction coefficient as a function of adherence time). Moreover the tangential stiffness and the dynamics of the setup have been implemented in the numerical model. A series of springs (Figure 6-16) have been added to the model in the x direction, giving a global tangential stiffness corresponding to the one estimated in section 3.3. Furthermore an equivalent distributed mass and viscous damping ($C=\alpha_3*M$) has been added in the model, at the boundary of the sample connected with the spring, in order to account for the tangential mode of vibration of the set-up (see section 3.3), which is the mainly involved mode in the dynamic response of the set-up. The numerical model allows for investigating the interaction between the dynamic response of the system and the local contact dynamics during the sliding motion between the same materials considered in the experimental tests.

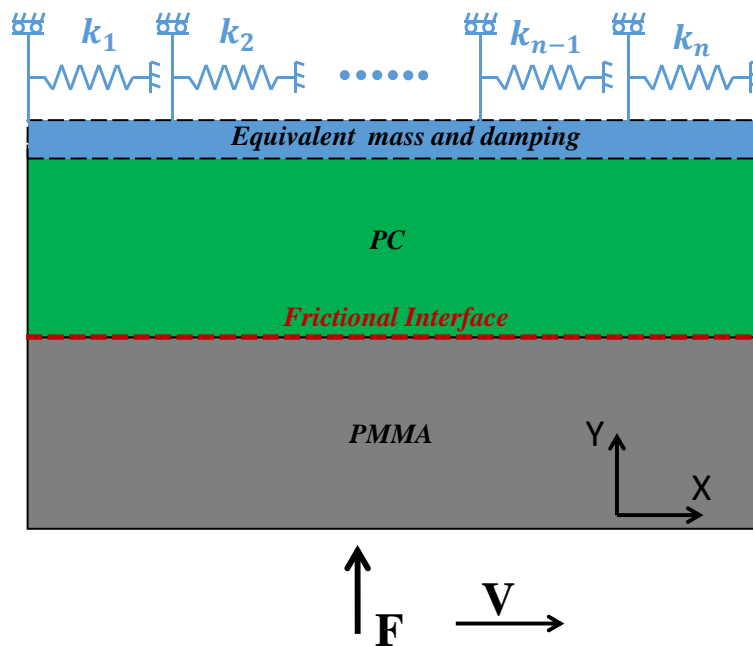


Figure 6-16: Updated numerical model and boundary conditions. The equivalent mass, damping and tangential stiffness are representative of the setup dynamics.

The material and geometrical properties of the model are listed in the Table 6.

The parameters of the friction law in the different conditions are reported in the Table 7. In the first phase the two bodies are put in contact until the compressive normal force F is reached; afterwards the constant horizontal velocity V is applied at the lower body to bring the system in relative motion, while the upper body is maintained fixed along the y direction as in the experimental performed tests. In the updated model the distributed stiffness (springs), mass and damping, representing the set-up dynamics, are interposed between the frame and the upper sample.

	Polycarbonate	PMMA
Length [mm]	30	30
Width [mm]	10	10
Element number	30000	5590
Contact element size [mm]	0.1	0.23
Density [kg/m³]	1200	1190
Young Modulus [GPa]	2.35	3.3
Poisson coefficient	0.4	0.37
Material damping α [1/s]	40	300
Material damping β [s]	1e-7	1e-7
Simulation time step [s]	9e-9	
	Equivalent properties	
Density equivalent mass [kg/m³]	5.83 · 10 ⁶	
Setup Tangential stiffness [N/m]	1.7 · 10 ⁷	
Equivalent damping α_3 [1/s]	100/250	

Table 6: Geometry dimensions, material and mesh properties used to perform the non-linear transient simulations.

	A	B	C	μ_0
Roughness type-01 and $\sigma=3$ MPa	0.32	0.29	100	0.76
Roughness type-02 and $\sigma=5$ MPa	0.275	0.135	140	0.53

Table 7: Parameters of the friction contact law implemented in the numerical model.

6.3.2 Validation of the numerical model: the macroscopic frictional and dynamic response

This section presents a comparison between the experimental tests and the numerical results carried out by means of the transient non-linear simulations. The effect of the boundary conditions on the macroscopic frictional behaviour have been numerically investigated considering the 2D plane strain model in Figure 6-16. The comparison with experiments has been performed considering the two contact surface roughness, detailed in the section 6.1. For each roughness and related average contact pressure, the curve of the friction coefficient has been recovered from experimental tests, allowing for defining appropriate parameters of the friction law detailed in Table 7.

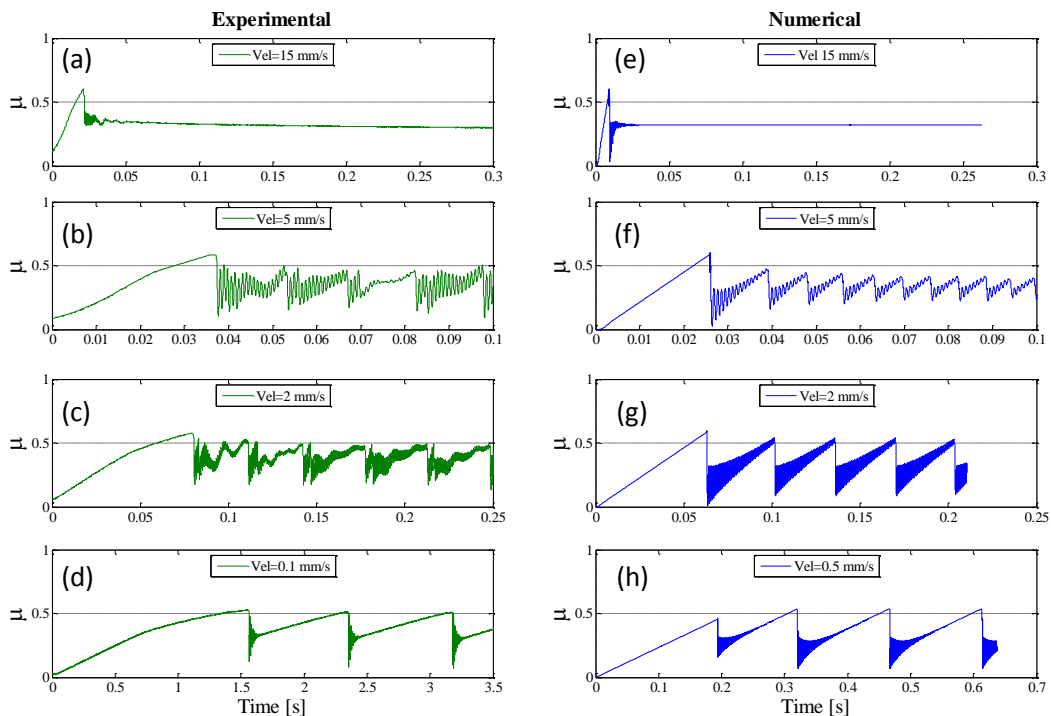


Figure 6-17: Experimental (left) and numerical (right) macroscopic friction coefficient, as a function of relative velocity, for average contact pressure of 5 MPa and sample surface roughness of type-02 ($S_a=0.115$). The parameters of the friction contact law used in the simulations are reported in the table 7. Equivalent damping $\alpha_3=250 [s^{-1}]$.

Figure 6-17 shows the effect of the imposed relative velocity, both experimentally and numerically, on the macroscopic frictional behaviour in the case of roughness type-02 and average contact pressure of 5 MPa. The macroscopic friction coefficient along the time has been calculated as the ratio between the global tangential force and normal force measured at the boundaries

for both the numerical and experimental (force transducer) analyses. Ranging the imposed velocity from 0.1 mm/s to 15 mm/s, maintaining fixed the normal force, the behaviour of the numerical system changes its pattern (Figure 6-17, right) accordingly with the experimental measurements (Figure 6-17, left). For a translational velocity of 15 mm/s the numerical model exhibits a typical stable continuous sliding behaviour (Figure 6-17(e)) as observed experimentally for the same value of the sliding velocity and for the same average contact pressure (Figure 6-17(a)). The friction coefficient shows a linear increasing until it reaches the maximum value and, after a sudden drop due to the release of the elastic energy, its value becomes constant at a lower value corresponding to the dynamic friction coefficient. The initial drop in the friction coefficient (related to the tangential force drop) produces an excitation that leads to decaying oscillations of the system. After this first phase of transition from adherence to sliding state of the whole surface, the friction coefficient stabilizes itself reaching the steady value of 0.32, like in the experimental test (Figure 6-17(a)). Decreasing the horizontal imposed velocity, both experimentally and numerically, the macroscopic frictional behaviour changes completely its pattern (Figure 6-17(b) and Figure 6-17(f)), in a macroscopic stick-slip behaviour. The drops of the tangential force along the time produce periodic fluctuations in the macroscopic friction curve, as shown in the Figure 6-17 for an imposed velocity of 5, 2 and 0.1 mm/s. Continuing to decrease the imposed velocity for values lower than 2 mm/s and maintaining fixed the average normal load, the macroscopic contact scenarios is always characterized by macroscopic stick-slip phenomena (Figure 6-17(d) and Figure 6-17(h)). Moreover Figure 6-17 shows that, both numerically and experimentally, the amplitude of the drops of the macroscopic friction and the time period of stick-slip events increase as the imposed velocity is reduced.

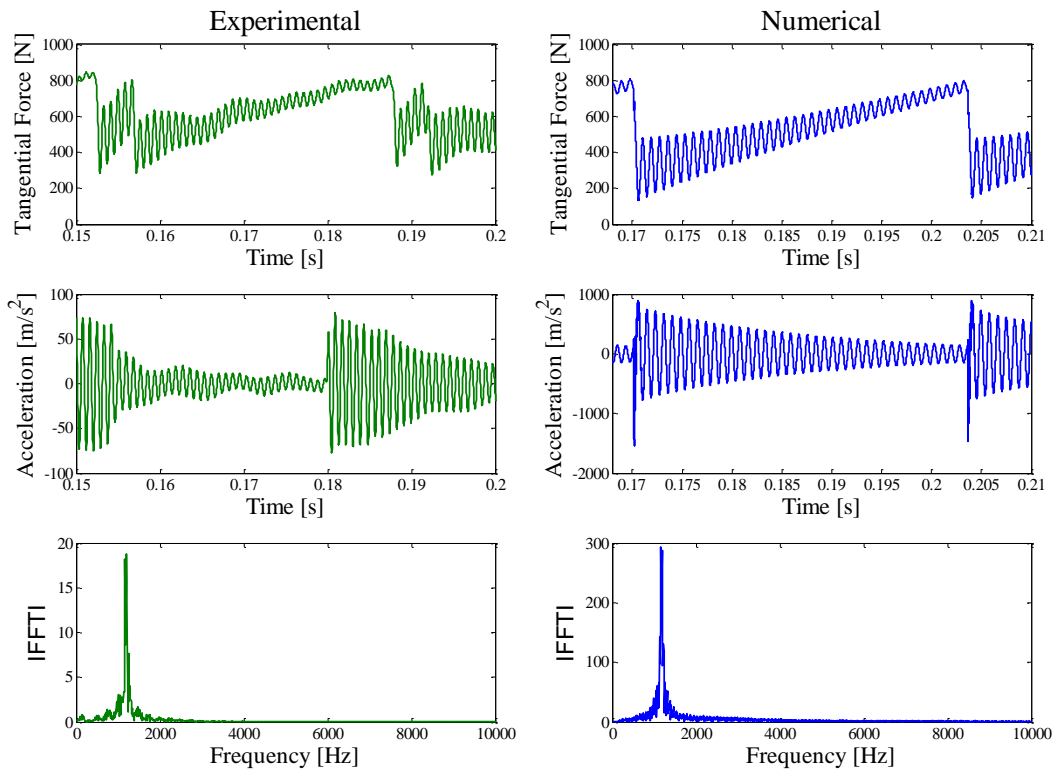


Figure 6-18: Tangential force, tangential acceleration and spectrum of the acceleration signal in the case of driving velocity of 2 mm/s and average contact pressure of 5 MPa both experimentally and numerically, obtained between two macro-slip events.

Figure 6-18 shows the decaying oscillations between two slip events for driving velocity of 2 mm/s and average contact pressure of 5 MPa, both numerically and experimentally. Figure 6-18 shows how the system vibrations excited experimentally and numerically after each force drop, present a frequency content mainly around 1200 Hz, due to the dynamic response of the tangential mode of the experimental set-up (Figure 6-18); the differences in term of the amplitude of the acceleration signals shown in the Figure 6-18 are due to the fact that the experimental signal is related to the acceleration of the support of the sample (just under the sample), while the numerical acceleration signal is related to one point of the upper boundary of the PC block (Figure 6-16). In fact, it would have been impossible to add an accelerometer on the side of the samples, because of their small dimensions. Nevertheless, the time and frequency analysis show a good agreement between numerical and experimental vibrational response of the system.

The low frequency fluctuations that can be observed in Figure 6-17 and Figure 6-18, for the experimental signals, are due to a mode of vibration of the

whole structure supporting the set-up at about 110 Hz. Anyway, this disturbance is just superposing the system response and is not affecting significantly the different contact scenarios obtained both experimentally and numerically.

Further experiments have been performed with the support of a laser vibrometer allowing for a quantitative validation not only the global signals (force, acceleration of the sample support) but also the vibration response along the tangential direction (laser velocity) of a point of the samples close to the contact interface.

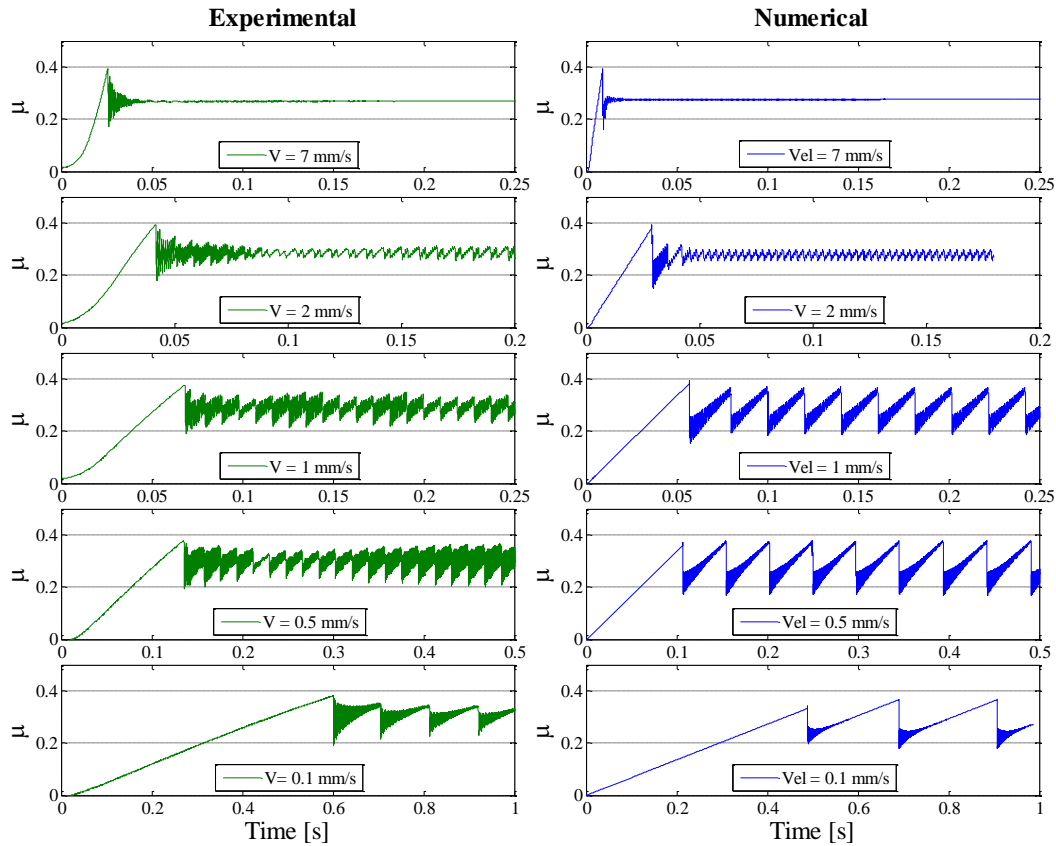


Figure 6-19: Experimental (left) and numerical (right) macroscopic friction coefficient, as a function of relative velocity, for average contact pressure of 3 MPa and sample surface roughness of type-01 ($S_a=0.305$). The parameters of the friction contact law used in the simulations are reported in the table 7. Equivalent damping $\alpha_3=100 [s^{-1}]$.

Figure 6-19 shows the effect of the imposed horizontal velocity, both experimentally and numerically, on the macroscopic frictional behaviour in the case of roughness type-01 and average contact pressure of 3 MPa. The frictional system switches from continuous sliding to macroscopic stick-slip, when decreasing the imposed driving velocity, as observed in the previous case (see Figure 6-17). For the imposed driving velocity of 2 mm/s, the frictional system

exhibits the transition of the behaviour (Figure 6-19(b) and Figure 6-19(g)) between continuous sliding to macroscopic stick-slip instability both experimentally and numerically. Decreasing the driving velocity, the frictional response of the system shows an increasing trend of the force drop amplitude and the period between two subsequent drops. Figure 6-20 shows a zoom of the frictional response (Figure 6-19(d) and Figure 6-19(i)) during the first tangential drop (macro-slip event). The frequency and time analyses in Figure 6-20 show a good quantitative agreement between experimental and numerical results. The time-varying spectrum of the signal velocity (Figure 6-20) shows as the main frequency excited after the macro-slip event is around 20 kHz both experimentally and numerically. After the macro-slip event the system oscillations due to the contact sample dynamics (several kHz) decrease due to the material damping both in the numerical model and in the experiments. Afterwards, only the macroscopic oscillation of the set-up at its tangential mode frequency (1200 Hz) is appreciable in the time signals. The velocity measured by the laser vibrometer, close to the sample contact interface, allows for recovering the full dynamic response; the tangential force, averaged and measured at the position of the force transducer miss the information about the dynamic response of the samples in contact. The different amplitude of the force oscillations into the comparison between experimental and numerical results could be attributed to a dependence of damping (associated to the tangential mode of the setup) by various parameters such as contact pressure, amplitude of oscillations, that are not accounted for in the numerical damping model where the proportional mass damping is introduced ($C=\alpha_3*M$).

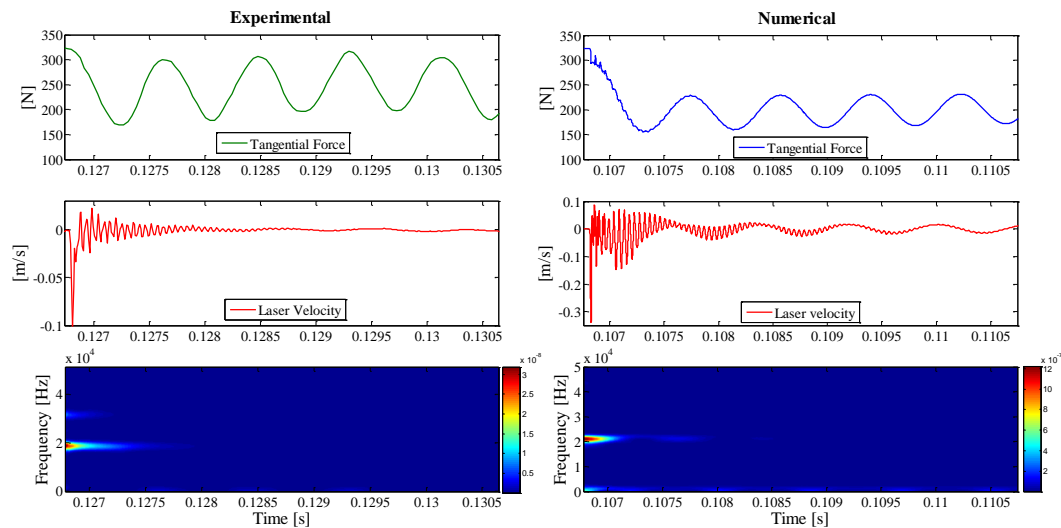


Figure 6-20: Experimental (left) and numerical (right) comparison during macro-slip event for the following boundary condition: imposed driving velocity

of 0.5 mm/s and average contact pressure of 3 MPa. Sample surface roughness of type-01 ($S_a=0.305$).

6.4 Concluding remarks

Contact frictional scenarios of similar contact materials (PMMA-PMMA) and dissimilar ones (PMMA-PC), have been investigated both experimentally and numerically. The dedicated experimental set-up, TRIBOWAVE, allowed for reproducing the relative motion under well controlled values of the driving parameters. The tests performed on the experimental set-up highlight the complex phenomena arising when two media are in frictional sliding. The same system with respect to different boundary conditions, such as imposed horizontal velocity, switches its macroscopic frictional behaviour from macro stick-slip instability up to stable continuous sliding with or without mode coupling instability. Maps of the frictional contact scenario have been drawn.

The updated numerical model, including the set-up tangential stiffness and dynamics, allowed for reproducing a qualitative comparison and obtaining the same transition ranges from stable sliding to macroscopic stick-slip as a function of the key parameters. The numerical results show a quantitative agreement both in frequency and in time domain with the macroscopic frictional behaviours obtained by the experiments. The comparison, performed on the macroscopic response of the system (measured forces, acceleration and velocity), allows for validating the numerical simulations, which are useful for the investigation of the local contact dynamics (see section 4.7 and [17]) and its coupling with the system response.

7 General conclusions

7.1 Original contributions

The present thesis is addressed to the investigation of the mechanisms at the origin of the different frictional contact scenarios between two elastic media in relative motion.

The development of the experimental and numerical tools and the dialog between experiments and simulations of frictional contact dynamics allowed for investigating the coupling between the local contact behaviour (status of interfaces, relative interface velocity, wave and rupture propagation) and the system response (vibrations, unstable modes) as a function of system parameters (material damping, imposed driving velocity, average contact pressure, surface roughness, friction coefficient). The main contributions of this work are considered in the following points:

- i) Transient non-linear simulations and complex eigenvalue analysis performed with a simple frictional elastic model show, as a function of system parameters, how the same system can be characterized by either macroscopic stick-slip phenomena, harmonic vibrations due to the mode coupling instability, or stable state in continuous sliding.
- ii) Frictional scenario maps have been drawn as a function of pairs of the system parameters. One of the main parameters retained for the analysis is the material damping, because of its key role in both the dissipation of the energy released locally at the contact (rupture and wave propagation) and the stabilization effect on the whole system dynamics.
- iii) A newer experimental setup, named TRIBOWAVE, has been developed to investigate frictional instabilities arising between samples in contact. A stiffness and dynamic characterization of the setup has been carried out in order to implement the dynamic characteristics of the whole system in the numerical model. Preliminary experimental analyses highlighted and confirmed the macroscopic frictional scenarios obtained numerically, while non-linear transient simulations highlighted the same experimental transition range from stable sliding to macroscopic stick-slip as a function of the same key parameters.
- iv) Frictional scenario maps as a function of imposed boundary conditions have been drawn experimentally and numerically considering different contact material pairs and surface roughness.

- v) The experimental and numerical results on the mode coupling instability scenario allowed for generalizing the theory of mode lock-in presented in the literature for specific contact issues (brake squeal, hip endoprosthesis squeaking, clutch instability). In each elastic system under frictional contact, with appropriate system parameters and boundary conditions, the mode coupling instability can occur giving origin to harmonic vibrations. This result can explain several everyday noise emissions coming from frictional contacts and not attributable to stick-slip phenomena because of their harmonic feature.
- vi) Experimental tests on different contact material pairs allowed for defining appropriate friction laws as a function of the adherence time. A quantitative validation of the updated numerical model has been realized, with experiments, on the macroscopic frictional response of the system.
- vii) On the other hand, the numerical model allowed for investigating the local behaviour at the contact interface, which is, for the moment, difficult to achieve with experimental techniques. In fact nowadays, the measurement of the local dynamics at the contact is one of the main challenges.
- viii) The numerical results highlighted the coupling between local contact response and system dynamic response, which is at the origin of the different macroscopic contact scenarios. While the macroscopic stick-slip is driven by the local contact phenomena (rupture and wave propagation), the dynamic system instabilities (mode coupling) can drive the local contact distribution, and vice-versa.

In a more general manner the results of this thesis highlighted the complexity of the local (contact) and global (system) phenomena involved during sliding motion between elastic media. Moreover the present work underlines how a combined experimental and numerical analysis is needed for understanding the mechanisms at the origin of the different scenarios of frictional contact instability.

7.2 Future works

As stated above, the results from the thesis highlighted the complexity of the phenomena and, consequently, allowed to point out some of the main perspectives regarding the experimental and numerical investigations. Some of the major points are reported in the following:

- i) With the updated numerical model, validated experimentally in this thesis, time and frequency analyses of the local contact dynamics are needed to characterize the contact behavior during macroscopic frictional instabilities.
- ii) Newer techniques are needed to observe experimentally the fast phenomena occurring at the contact interface (wave propagations, local contact distribution). The developed experimental set-up has been designed to provide full access to the samples and the contact interface.
- iii) Then a comparison of the local contact dynamics with the measurements of the local dynamics during frictional instabilities is needed to realize a quantitative validation of the numerical model at the contact scale.
- iv) Several key parameters, like the surface roughness, should be implemented into the numerical model in order to investigate its effect on the frictional instabilities and the local behavior.
- v) Parametrical analyses on roughness, contact materials and different geometries are needed, numerically and experimentally, in order to better understand and control the friction between bodies by exploiting the “dynamic response” of the surface and the system.
- vi) A specific investigation will be performed to analyze the effect of external wave fields in the frictional behavior in order to control/avoid frictional instabilities.
- vii) It has been shown that a key role, in all the contact scenarios, is played by the material damping. Further numerical developments are needed in the defining of the new appropriated damping models, in order to consider a more realistic trend of the material damping factor within a larger frequency range; this need is due to the different time (frequency) scales involved in the phenomena: from some Hz of the structural scale (system modes) to hundreds of kHz of contact scale (rupture and wave propagation).

Finally, the understanding and controlling of the coupling between local contact dynamics and system dynamics could bring to innovative tools and technics able to avoid/control frictional contact instabilities and related wear and noise issues.

8 References

- [1] G. Amontons, "De la résistance causée dans les machines, tant par le frottement des parties qui les composent que par la roideur des corps qu'on y employe, et la manière de calculer l'un et l'autre," *Compte rendu de l'Académie des Sciences*, pp. 206-227, 1699.
- [2] C. A. Coulomb, *Theorie des machines simples*. Paris: Memoire de Mathematique et de Physique de l'Academie Royale, 1785.
- [3] M. Godet, "The third-body approach: A mechanical view of wear," *Wear*, vol. 100, pp. 437-452, 12// 1984.
- [4] Y. Berthier, *Background on friction and wear: Handbook of materials behaviour models*, Lemaître Academic Press, 2001
- [5] J. F. Brunel, P. Dufrénoy, M. Naït, J. L. Muñoz, and F. Demilly, "Transient models for curve squeal noise," *Journal of Sound and Vibration*, vol. 293, pp. 758-765, 6/13/ 2006.
- [6] H. Kasem, J.-F. Witz, P. Dufrénoy, and Y. Desplanques, "Monitoring of Transient Phenomena in Sliding Contact Application to Friction Brakes," *Tribology Letters*, vol. 51, pp. 235-242, 2013/08/01 2013.
- [7] N. M. Kinkaid, O. M. O'Reilly, and P. Papadopoulos, "Automotive disc brake squeal," *Journal of Sound and Vibration*, vol. 267, pp. 105-166, 10/9/ 2003.
- [8] H. Ouyang, W. Nack, Y. Yuan, and F. Chen, "Numerical analysis of automotive disc brake squeal: a review," *International Journal of Vehicle Noise and Vibration*, vol. 1, pp. 207-231, 01/01/ 2005.
- [9] J. J. Sinou, "Transient non-linear dynamic analysis of automotive disc brake squeal – On the need to consider both stability and non-linear analysis," *Mechanics Research Communications*, vol. 37, pp. 96-105, 1// 2010.
- [10] B. Hervé, J. J. Sinou, H. Mahé, and L. Jézéquel, "Analysis of squeal noise and mode coupling instabilities including damping and gyroscopic effects," *European Journal of Mechanics - A/Solids*, vol. 27, pp. 141-160, 3// 2008.
- [11] F. Massi, J. Rocchi, A. Culla, and Y. Berthier, "Coupling system dynamics and contact behaviour: Modelling bearings subjected to environmental induced vibrations and 'false brinelling' degradation," *Mechanical Systems and Signal Processing*, vol. 24, pp. 1068-1080, 5// 2010.
- [12] Y. Ben-Zion, "Dynamic ruptures in recent models of earthquake faults," *Journal of the Mechanics and Physics of Solids*, vol. 49, pp. 2209-2244, 9// 2001.
- [13] R. Fagiani, F. Massi, E. Chatelet, Y. Berthier, and A. Sestieri, "Experimental analysis of friction-induced vibrations at the finger contact surface," *Proceedings of the Institution of Mechanical Engineers, Part J: Journal of Engineering Tribology*, vol. 224, pp. 1027-1035, 2010.
- [14] N. Fan and G. X. Chen, "Numerical study of squeaking suppresses for ceramic-on-ceramic hip endoprosthesis," *Tribology International*, vol. 48, pp. 172-181, 4// 2012.

- [15] C. Weiss, A. Hothan, M. Morlock, and N. Hoffmann, "Friction-Induced Vibration of Artificial Hip Joints," *GAMM-Mitteilungen*, vol. 32, pp. 193-204, 2009.
- [16] A. Cochard and J. R. Rice, "Fault rupture between dissimilar materials: Ill-posedness, regularization, and slip-pulse response," *Journal of Geophysical Research: Solid Earth*, vol. 105, pp. 25891-25907, 2000.
- [17] M. Di Bartolomeo, F. Massi, L. Baillet, A. Culla, A. Fregolent, and Y. Berthier, "Wave and rupture propagation at frictional bimaterial sliding interfaces: From local to global dynamics, from stick-slip to continuous sliding," *Tribology International*, vol. 52, pp. 117-131, 8// 2012.
- [18] Z. Shi and Y. Ben-Zion, "Dynamic rupture on a bimaterial interface governed by slip-weakening friction," *Geophysical Journal International*, vol. 165, pp. 469-484, 2006.
- [19] S. Maegawa, A. Suzuki, and K. Nakano, "Precursors of Global Slip in a Longitudinal Line Contact Under Non-Uniform Normal Loading," *Tribology Letters*, vol. 38, pp. 313-323, 2010/06/01 2010.
- [20] S. M. Rubinstein, G. Cohen, and J. Fineberg, "Dynamics of Precursors to Frictional Sliding," *Physical Review Letters*, vol. 98, p. 226103, 06/01/ 2007.
- [21] D. Majcherczak, P. Dufrenoy, and Y. Berthier, "Tribological, thermal and mechanical coupling aspects of the dry sliding contact," *Tribology International*, vol. 40, pp. 834-843, 5// 2007.
- [22] A. Akay, "Acoustics of friction," *The Journal of the Acoustical Society of America*, vol. 111, pp. 1525-1548, 2002.
- [23] G. S. Chen, *Handbook of Friction-Vibration Interactions*: Elsevier Science, 2014.
- [24] D. Tonazzi, F. Massi, A. Culla, L. Baillet, A. Fregolent, and Y. Berthier, "Instability scenarios between elastic media under frictional contact," *Mechanical Systems and Signal Processing*, vol. 40, pp. 754-766, 11// 2013.
- [25] D. Tonazzi, F. Massi, L. Baillet, A. Culla, M. Di Bartolomeo, and Y. Berthier, "Experimental and numerical analysis of frictional contact scenarios: from macro stick-slip to continuous sliding," *Meccanica*, pp. 1-16, 2014/07/08 2014.
- [26] C. Voisin, F. Renard, and J.-R. Grasso, "Long term friction: From stick-slip to stable sliding," *Geophysical Research Letters*, vol. 34, p. L13301, 2007.
- [27] T. Baumberger, C. Caroli, and O. Ronsin, "Self-Healing Slip Pulses along a Gel/Glass Interface," *Physical Review Letters*, vol. 88, p. 075509, 02/04/ 2002.
- [28] "Slip dynamics at a patterned rubber/glass interface during stick-slip motions," *The European Physical Journal E*, vol. 35, 2012.
- [29] S. Nielsen, J. Taddeucci, and S. Vinciguerra, "Experimental observation of stick-slip instability fronts," *Geophysical Journal International*, vol. 180, pp. 697-702, 2010.
- [30] J. Brunetti, F. Massi, W. D'Ambrogio, and Y. Berthier, "Dynamic and energy analysis of frictional contact instabilities on a lumped system," *Meccanica*, pp. 1-15, 2014/08/07 2014.
- [31] B. Hervé, J. J. Sinou, H. Mahé, and L. Jezequel, "Analysis of squeal noise and mode coupling instabilities including damping and gyroscopic effects," *European Journal of Mechanics-A/Solids*, vol. 27, pp. 141-160, 2008.

- [32] M. Dezi, P. Forte, and F. Frendo, "Motorcycle brake squeal: experimental and numerical investigation on a case study," *Meccanica*, vol. 49, pp. 1011-1021, 2014/04/01 2014.
- [33] L. Baillet, S. D'Errico, and B. Lualagnet, "Understanding the occurrence of squealing noise using the temporal finite element method," *Journal of Sound and Vibration*, vol. 292, pp. 443-460, 5/9/ 2006.
- [34] C. Weiss, P. Gdaniec, N. P. Hoffmann, A. Hothan, G. Huber, and M. M. Morlock, "Squeak in hip endoprosthesis systems: An experimental study and a numerical technique to analyze design variants," *Medical Engineering & Physics*, vol. 32, pp. 604-609, 7// 2010.
- [35] A. Saulot and L. Baillet, "Dynamic Finite Element Simulations for Understanding Wheel-Rail Contact Oscillatory States Occurring Under Sliding Conditions," *Journal of Tribology*, vol. 128, pp. 761-770, 2006.
- [36] M. A. Heckl and I. D. Abrahams, "CURVE SQUEAL OF TRAIN WHEELS, PART 1: MATHEMATICAL MODEL FOR ITS GENERATION," *Journal of Sound and Vibration*, vol. 229, pp. 669-693, 1/20/ 2000.
- [37] D. Thompson, *Railway Noise and Vibration: Mechanisms, Modelling and Means of Control*: Elsevier Science, 2008.
- [38] Y. Altintas, *Manufacturing Automation: Metal Cutting Mechanics, Machine Tool Vibrations, and CNC Design*: Cambridge University Press, 2012.
- [39] R. Goodman and P. N. Sundaram, "Fault and system stiffnesses and stick-slip phenomena," *pure and applied geophysics*, vol. 116, pp. 873-887, 1978/07/01 1978.
- [40] W. Tang, S.-r. Ge, H. Zhu, X.-c. Cao, and N. Li, "The Influence of Normal Load and Sliding Speed on Frictional Properties of Skin," *Journal of Bionic Engineering*, vol. 5, pp. 33-38, 3// 2008.
- [41] U. Andreaus and P. Casini, "DYNAMICS OF FRICTION OSCILLATORS EXCITED BY A MOVING BASE AND/OR DRIVING FORCE," *Journal of Sound and Vibration*, vol. 245, pp. 685-699, 8/23/ 2001.
- [42] N. Hoffmann, M. Fischer, R. Allgaier, and L. Gaul, "A minimal model for studying properties of the mode-coupling type instability in friction induced oscillations," *Mechanics Research Communications*, vol. 29, pp. 197-205, 2002.
- [43] M. Renouf, H. P. Cao, and V. H. Nhu, "Multiphysical modeling of third-body rheology," *Tribology International*, vol. 44, pp. 417-425, 4// 2011.
- [44] U. Andreaus and P. Casini, "Friction oscillator excited by moving base and colliding with a rigid or deformable obstacle," *International Journal of Non-Linear Mechanics*, vol. 37, pp. 117-133, 1// 2002.
- [45] F. D'Annibale and A. Luongo, "A damage constitutive model for sliding friction coupled to wear," *Continuum Mechanics and Thermodynamics*, vol. 25, pp. 503-522, 2013/03/01 2013.
- [46] E. Sacco and F. Lebon, "A damage–friction interface model derived from micromechanical approach," *International Journal of Solids and Structures*, vol. 49, pp. 3666-3680, 12/15/ 2012.
- [47] M. T. Bengisu and A. Akay, "Stability of Friction-Induced Vibrations in Multi-Degree-of-Freedom Systems," *Journal of Sound and Vibration*, vol. 171, pp. 557-570, 4/7/ 1994.
- [48] N. Hoffmann and L. Gaul, "Effects of damping on mode-coupling instability in friction induced oscillations," *ZAMM - Journal of Applied Mathematics*

- and Mechanics / Zeitschrift für Angewandte Mathematik und Mechanik*, vol. 83, pp. 524-534, 2003.
- [49] J.-J. Sinou and L. Jézéquel, "Mode coupling instability in friction-induced vibrations and its dependency on system parameters including damping," *European Journal of Mechanics - A/Solids*, vol. 26, pp. 106-122, 1// 2007.
- [50] V. Magnier, J. F. Brunel, and P. Dufrénoy, "Impact of contact stiffness heterogeneities on friction-induced vibration," *International Journal of Solids and Structures*, vol. 51, pp. 1662-1669, 5/1/ 2014.
- [51] O. Ben-David and J. Fineberg, "Static Friction Coefficient Is Not a Material Constant," *Physical Review Letters*, vol. 106, p. 254301, 06/20/ 2011.
- [52] C. Fusco and A. Fasolino, "Velocity dependence of atomic-scale friction: A comparative study of the one- and two-dimensional Tomlinson model," *Physical Review B*, vol. 71, p. 045413, 01/12/ 2005.
- [53] A. Socoliuc, R. Bennewitz, E. Gnecco, and E. Meyer, "Transition from Stick-Slip to Continuous Sliding in Atomic Friction: Entering a New Regime of Ultralow Friction," *Physical Review Letters*, vol. 92, p. 134301, 04/01/ 2004.
- [54] G. G. Adams, "Self-Excited Oscillations of Two Elastic Half-Spaces Sliding With a Constant Coefficient of Friction," *Journal of Applied Mechanics*, vol. 62, pp. 867-872, 1995.
- [55] G. G. Adams, "Steady Sliding of Two Elastic Half-Spaces With Friction Reduction due to Interface Stick-Slip," *Journal of Applied Mechanics*, vol. 65, pp. 470-475, 1998.
- [56] G. G. Adams and M. Nosonovsky, "Elastic waves induced by the frictional sliding of two elastic half-spaces," in *Tribology Series*. vol. Volume 39, A. A. L. D. D. a. M. P. G. Dalmaz, Ed., ed: Elsevier, 2001, pp. 47-54.
- [57] L. Baillet, B. Laulagnet, Y. Berthier, V. Linck, and S. D'Errico, "Finite Element Simulation of Dynamic Instabilities in Frictional Sliding Contact," *Journal of Tribology*, vol. 127, pp. 652-657, 2005.
- [58] L. Baillet, V. Link, S. D'errico, and Y. Berthier, "Influence of sliding contact local dynamics on macroscopic friction coefficient variation," vol. 14/2-3, R. E. d. Element, Ed., ed, 2005, pp. 305-321.
- [59] F. Massi, Y. Berthier, and L. Baillet, "Contact surface topography and system dynamics of brake squeal," *Wear*, vol. 265, pp. 1784-1792, 11/26/ 2008.
- [60] G. Antoni, T. Désoyer, and F. Lebon, "A thermo-mechanical modelling of the Tribological Transformations of Surface," *Comptes Rendus Mécanique*, vol. 337, pp. 653-658, 9// 2009.
- [61] M. Champagne, M. Renouf, and Y. Berthier, "Modeling Wear for Heterogeneous Bi-Phasic Materials Using Discrete Elements Approach," *Journal of Tribology*, vol. 136, pp. 021603-021603, 2014.
- [62] "1D Model of Precursors to Frictional Stick-Slip Motion Allowing for Robust Comparison with Experiments," *Tribology Letters*, 2011.
- [63] J. Trømborg, J. Scheibert, D. S. Amundsen, K. Thøgersen, and A. Malthesørensen, "Transition from Static to Kinetic Friction: Insights from a 2D Model," *Physical Review Letters*, vol. 107, p. 074301, 08/12/ 2011.
- [64] S. M. Rubinstein, G. Cohen, and J. Fineberg, "Detachment fronts and the onset of dynamic friction," *Nature*, vol. 430, pp. 1005-1009, // 2004.

- [65] S. M. R. a. G. C. a. J. Fineberg, "Visualizing stick–slip: experimental observations of processes governing the nucleation of frictional sliding," *Journal of Physics D: Applied Physics*, vol. 42, p. 214016, 2009.
- [66] D. Zigone, C. Voisin, E. Larose, F. Renard, and M. Campillo, "Slip acceleration generates seismic tremor like signals in friction experiments," *Geophysical Research Letters*, vol. 38, p. L01315, 2011.
- [67] D. W. Lee, X. Banquy, and J. N. Israelachvili, "Stick-slip friction and wear of articular joints," *Proceedings of the National Academy of Sciences*, 2013.
- [68] M. Radiguet, D. S. Kammer, and J.-F. Molinari, "The role of viscoelasticity on heterogeneous stress fields at frictional interfaces," *Mechanics of Materials*, vol. 80, pp. 276-287, 2015.
- [69] D. S. Kammer, V. A. Yastrebov, G. Ancaux, and J. F. Molinari, "The existence of a critical length scale in regularised friction," *Journal of the Mechanics and Physics of Solids*, vol. 63, pp. 40-50, 2// 2014.
- [70] Z. Shi, A. Needleman, and Y. Ben-Zion, "Slip modes and partitioning of energy during dynamic frictional sliding between identical elastic–viscoplastic solids," *International Journal of Fracture*, vol. 162, pp. 51-67, 2010/03/01 2010.
- [71] H. R. Mills, *Brake Squeak* vol. Report No. 9162 B: Institution of Automobile Engineers, 1938.
- [72] R. T. SPURR, *A Theory of Brake Squeal*, 1961.
- [73] N. M. Ghazaly, Mohamed, El-Sharkawy, Ibrahim, Ahmed, "A Review of Automotive Brake Squeal Mechanisms," *Journal of Mechanical Design and Vibration*, vol. 1, pp. 5-9, 2013.
- [74] M. R. North, "Disc brake squeal," in *Conference on Braking of Road Vehicles, Automobile Division, Institution of Mechanical Engineers, Mechanical Engineering Publications Limited*, 1976, pp. 169-176.
- [75] X. Lorang, F. Foy-Margiocchi, Q. S. Nguyen, and P. E. Gautier, "TGV disc brake squeal," *Journal of Sound and Vibration*, vol. 293, pp. 735-746, 6/13/ 2006.
- [76] G. X. Chen, Z. R. Zhou, P. Kapsa, and L. Vincent, "Experimental investigation into squeal under reciprocating sliding," *Tribology International*, vol. 36, pp. 961-971, 12// 2003.
- [77] J. Kang, C. M. Krousgrill, and F. Sadeghi, "Analytical formulation of mode-coupling instability in disc–pad coupled system," *International Journal of Mechanical Sciences*, vol. 51, pp. 52-63, 1// 2009.
- [78] F. Massi, L. Baillet, O. Giannini, and A. Sestieri, "Brake squeal: Linear and nonlinear numerical approaches," *Mechanical Systems and Signal Processing*, vol. 21, pp. 2374-2393, 8// 2007.
- [79] F. Massi, L. Baillet, and A. Culla, "Structural modifications for squeal noise reduction: numerical and experimental validation," *International Journal of Vehicle Design*, vol. 51, pp. 168-189, 01/01/ 2009.
- [80] F. Cantone and F. Massi, "A numerical investigation into the squeal instability: Effect of damping," *Mechanical Systems and Signal Processing*, vol. 25, pp. 1727-1737, 7// 2011.
- [81] F. Massi and O. Giannini, "Effect of damping on the propensity of squeal instability: An experimental investigation," *The Journal of the Acoustical Society of America*, vol. 123, pp. 2017-2023, 2008.

- [82] P. Menezes, Kishore, S. Kailas, and M. Lovell, "Role of Surface Texture, Roughness, and Hardness on Friction During Unidirectional Sliding," *Tribology Letters*, vol. 41, pp. 1-15, 2011/01/01 2011.
- [83] M. O. Othman, A. H. Elkholly, and A. A. Seireg, "Experimental investigation of frictional noise and surface-roughness characteristics," *Experimental Mechanics*, vol. 30, pp. 328-331, 1990/12/01 1990.
- [84] B. L. Stoimenov, S. Maruyama, K. Adachi, and K. Kato, "The roughness effect on the frequency of frictional sound," *Tribology International*, vol. 40, pp. 659-664, 4// 2007.
- [85] L. Baillet and T. Sassi, "Finite element method with Lagrange multipliers for contact problems with friction," *Comptes Rendus Mathématique*, vol. 334, pp. 917-922, 2002.
- [86] N. J. Carpenter, R. L. Taylor, and M. G. Katona, "Lagrange constraints for transient finite element surface contact," *International Journal for Numerical Methods in Engineering*, vol. 32, pp. 103-128, 1991.
- [87] F. Massi, S. Aurelien, M. Renouf, and M. G., "Simulation of dynamic instabilities induced by sliding contacts," in *DINAME- Proceedings of the XV international symposium on dynamic problems of mechanics*, 2013.
- [88] M. Di Bartolomeo, A. Meziane, F. Massi, L. Baillet, and A. Fregolent, "Dynamic rupture at a frictional interface between dissimilar materials with asperities," *Tribology International*, vol. 43, pp. 1620-1630, 9// 2010.
- [89] V. Linck, "Modélisation numérique temporelle d'un contact frottant: Mise en évidence d'instabilités locales de contact-Conséquences tribologiques- ", LaMCoS, INSA-LYON, 2005.
- [90] M. A. Nayfeh, A. M. A. Hamdan, and A. H. Nayfeh, "Chaos and instability in a power system: Subharmonic-resonant case," *Nonlinear Dynamics*, vol. 2, pp. 53-72, 1991/01/01 1991.
- [91] A. Le Bot, E. Bou-Chakra, and G. Michon, "Dissipation of Vibration in Rough Contact," *Tribology Letters*, vol. 41, pp. 47-53, 2011/01/01 2011.
- [92] J. F. Tarter, "Prediction of Unstable Friction-Induced Vibrations using an Energy Criterion," Carnegie Mellon University, 2004.
- [93] D. Guan and J. Huang, "The method of feed-in energy on disc brake squeal," *Journal of Sound and Vibration*, vol. 261, pp. 297-307, 3/20/ 2003.
- [94] D. Vola, M. Raous, and J. A. C. Martins, "Friction and instability of steady sliding: squeal of a rubber/glass contact," *International Journal for Numerical Methods in Engineering*, vol. 46, pp. 1699-1720, 1999.
- [95] A. Culla, D. Tonazzi, and F. Massi, "Estimation of damping for highly damped structure with high modal densities," in *AIMETA*, 2013.
- [96] M. Renouf, F. Massi, N. Fillot, and A. Saulot, "Numerical tribology of a dry contact," *Tribology International*, vol. 44, pp. 834-844, 7// 2011.
- [97] F. P. Bowden and D. Tabor, *The Friction and Lubrication of Solids*: Clarendon Press, 1954.
- [98] E. Santner and H. Czichos, "Tribology of polymers," *Tribology International*, vol. 22, pp. 103-109, 4// 1989.
- [99] M. Radiguet, D. S. Kammer, P. Gillet, and J.-F. Molinari, "Survival of Heterogeneous Stress Distributions Created by Precursory Slip at Frictional Interfaces," *Physical Review Letters*, vol. 111, p. 164302, 10/18/ 2013.

FOLIO ADMINISTRATIF
THESE SOUTENUE DEVANT L'INSTITUT NATIONAL DES SCIENCES
APPLIQUEES DE LYON

NOM: TONAZZI	DATE de SOUTENANCE: 04/12/2014
Prénoms: Davide	
TITRE: Macroscopic frictional contact scenarios and local contact dynamics: at the origins of “macroscopic stick-slip”, mode coupling instabilities and stable continuous sliding.	
NATURE: Doctorat	Numéro d'ordre :
Ecole doctorale: MEGA	
Spécialité: Mécanique	
Code B.I.U. – Lyon : T 50/210/19 / et bis CLASSE :	
<p>RESUME: Le comportement local au contact et son interaction avec la dynamique globale du système sont à l'origine d'innombrables problèmes de contact concernant plusieurs disciplines telles que la tribologie, la géophysique, la mécanique de vibration ou la mécanique de la rupture. Lorsque deux corps élastiques sont en mouvement relatif avec une interface de frottement, des vibrations induites se produisent dans le système. Dans un point de vue macroscopique, le scénario macroscopique de stick-slip survenant pendant le mouvement relatif est caractérisé par la chute soudaine de la force de frottement (état de glissement), séparées par des périodes d'accumulation d'énergie élastique (état d'adhérence). Autrement, une instabilité dynamique se produit quand un mode de vibration du système mécanique devient instable en raison des forces de frottement. Ces types d'instabilités, générées par des forces de frottement, ont été principalement objet de publications traitant de problèmes spécifiques dans différents domaines tels que le crissement des freins, le crissement des prothèses de hanche, les vibrations roue-rail, les tremblements de terre, etc. Dans ce contexte, des analyses expérimentales et numériques ont été ici mises en place pour comprendre comme le comportement de l'interface locale affecte la réponse macroscopique du système et vice-versa, au cours de scénarios d'instabilité. Les scénarios macroscopiques (instabilité de « stick-slip macroscopique », instabilité modale, glissement continu stable), survenant entre deux milieux élastiques simples en mouvement relatif, ont été étudiés numériquement et expérimentalement. Un dispositif expérimental dédié (TRIBOWAVE) a été développé et a permis de reproduire et examiner les différents scénarios de frottement dans des conditions aux limites bien contrôlées. Les mêmes scénarios de frottement ont été reproduits par des simulations numériques transitoires. Une loi de frottement en fonction du temps d'adhérence (stick) a été définie à partir des essais expérimentaux. La loi de frottement obtenue a été mise en œuvre dans le modèle numérique, conduisant à une validation quantitative des scénarios de frottement par les expériences. Les simulations transitoires non linéaires, l'analyse aux valeurs propres complexes et les tests expérimentaux ont permis de dessiner des cartes de scénarios d'instabilité en fonction des paramètres clés du système. Validé par la comparaison avec les mesures des signaux expérimentaux globaux (forces, accélérations / vitesse), le modèle numérique a permis d'étudier le couplage entre le comportement du contact local (distribution de l'état du contact, propagation des ondes et des ruptures, précurseurs) et la réponse dynamique du système au cours du « stick-slip macroscopique », de l'instabilité due au couplage modale et du glissement continu stable. La compréhension du couplage entre le contact et la dynamique des systèmes apportera de nouvelles améliorations sur le contrôle des instabilités de contact et les problèmes d'usure connexes.</p>	
MOTS CLES : frottement sec, instabilités dues au frottement, stick-slip, couplage modale, dynamique de contact, analyse experimental, simulation numerique du contact.	
Laboratoire(s) de recherches : Dipartimento Ingegneria Meccanica e Aerospaziale (DIMA) et Laboratoire de Mécanique des Contacts et des Structures (LaMCoS).	
Directeurs de thèse : Yves BERTHIER Directeur de recherche (CNRS, INSA-Lyon) Annalisa FREGOLENT Professeur (La Sapienza, Université de Rome)	

Composition du jury :

Examiner/reviewer:	F. LEBON	(LMA, Aix-Marseille University)
Examiner/reviewer:	P. DUFRENOY	(LML, Lille1 University)
Examiner:	L. BAILLET	(ISTerre, UJF University of Grenoble)
Examiner/tutor:	Y. BERTHIER	(LaMCoS, INSA-LYON)
Examiner/tutor:	F. MASSI	(LaMCoS, INSA-LYON)
Examiner/tutor:	A. FREGOLENT	(DIMA, "Sapienza" University of Rome)
Examiner/tutor:	A. CULLA	(DIMA, "Sapienza" University of Rome)